Explanatory Supplement to the

Planck Early Release Compact Source Catalogue

planck

Version: 6 February 2012

Explanatory Supplement to the *Planck*[1,2] Early Release Compact Source Catalogue

Planck Collaboration: J. Aatrokoski, P. A. R. Ade, N. Aghanim, M. Arnaud, M. Ashdown, J. Aumont, C. Baccigalupi, A. Balbi, A. J. Banday, R. B. Barreiro, J. G. Bartlett, E. Battaner, K. Benabed, A. Benoît, J.-P. Bernard, M. Bersanelli, R. Bhatia, A. Bonaldi, L. Bonavera, J. R. Bond, J. Borrill, F. R. Bouchet, M. Bucher, C. Burigana, R. C. Butler, P. Cabella, C. M. Cantalupo, B. Cappellini, J.-F. Cardoso, P. Carvalho, A. Catalano, L. Cayón, A. Challinor, A. Chamballu, R.-R. Chary, X. Chen, L.-Y Chiang, C. Chiang, P. R. Christensen, D. L. Clements, S. Colombi, T. Conrow, F. Couchot, A. Coulais, B. P. Crill, F. Cuttaia, L. Danese, R. J. Davis, P. de Bernardis, A. de Rosa, G. de Zotti, J. Delabrouille, J.-M. Delouis, F.-X. Désert, J. Dick, C. Dickinson, J. M. Diego, K. Dolag, H. Dole, S. Donzelli, O. Doré, U. Dörl, M. Douspis, X. Dupac, G. Efstathiou, T. A. Enßlin, H. K. Eriksen, T. Evans, F. Finelli, O. Forni, P. Fosalba, M. Frailis, E. Franceschi, S. Galeotta, K. Ganga, M. Giard, Y. Giraud-Héraud, J. González-Nuevo, K. M. Górski, S. Gratton, A. Gregorio, A. Gruppuso, J. Haissinski, T. Handley, F. K. Hansen, D. Harrison, G. Helou, S. Henrot-Versillé, C. Hernández-Monteagudo, D. Herranz, S. R. Hildebrandt, E. Hivon, M. Hobson, W. A. Holmes, A. Hornstrup, W. Hovest, R. J. Hoyland, K. M. Huffenberger, M. Huynh, A. H. Jaffe, W. C. Jones, M. Juvela, E. Keihänen, R. Keskitalo, T. S. Kisner, R. Kneissl, L. Knox, H. Kurki-Suonio, G. Lagache, A. Lähteenmäki, J.-M. Lamarre, A. Lasenby, R. J. Laureijs, C. R. Lawrence, S. Leach, J. P. Leahy, W.-P. Lee, R. Leonardi, J. León-Tavares, C. Leroy, P. B. Lilje, M. Linden-Vørnle, M. López-Caniego, P. M. Lubin, J. F. Macías-Pérez, C. J. MacTavish, B. Maffei, G. Maggio, D. Maino, N. Mandolesi, R. Mann, M. Maris, F. Marleau, D. J. Marshall, E. Martínez-González, S. Masi, M. Massardi, S. Matarrese, F. Matthai, P. Mazzotta, P. McGehee, P. R. Meinhold, A. Melchiorri, J.-B. Melin, L. Mendes, A. Mennella, S. Mitra, M.-A. Miville-Deschênes, A. Moneti, L. Montier, G. Morgante, D. Mortlock, D. Munshi, A. Murphy, P. Naselsky, P. Natoli, C. B. Netterfield, H. U. Nørgaard-Nielsen, F. Noviello, D. Novikov, I. Novikov, I. J. O'Dwyer, S. Osborne, F. Pajot, R. Paladini, B. Partridge, F. Pasian, G. Patanchon, T. J. Pearson,

[1]Planck (http://www.esa.int/Planck) is a project of the European Space Agency ESA with instruments provided by two scientific Consortia funded by ESA member states (in particular the lead countries: France and Italy) with contributions from NASA (USA), and telescope reflectors provided in a collaboration between ESA and a scientific Consortium led and funded by Denmark.

[2]E-mail: piahelp@sciops.esa.int

O. Perdereau, L. Perotto, F. Perrotta, F. Piacentini, M. Piat, R. Piffaretti, S. Plaszczynski, P. Platania, E. Pointecouteau, G. Polenta, N. Ponthieu, T. Poutanen, G. W. Pratt, G. Prézeau, S. Prunet, J.-L. Puget, J. P. Rachen, W. T. Reach, R. Rebolo, M. Reinecke, C. Renault, S. Ricciardi, T. Riller, I. Ristorcelli, G. Rocha, C. Rosset, L. Rottler, M. Rowan-Robinson, J. A. Rubiño-Martín, B. Rusholme, A. Sajina, M. Sandri, D. Santos, G. Savini, B. M. Schaefer, S. Schurr, D. Scott, M. D. Seiffert, P. Shellard, G. F. Smoot, J.-L. Starck, F. Stivoli, V. Stolyarov, R. Sudiwala, R. Sunyaev, J.-F. Sygnet, J. A. Tauber, D. Tavagnacco, L. Terenzi, L. Toffolatti, M. Tomasi, M. Tornikoski, J.-P. Torre, M. Tristram, J. Tuovinen, M. Türler, G. Umana, L. Valenziano, J. Valiviita, J. Varis, P. Vielva, F. Villa, N. Vittorio, L. A. Wade, B. D. Wandelt, S. D. M. White, A. Wilkinson, D. Yvon, A. Zacchei, A. Zonca

Update History

- 6 Feb 2012: Minor additions to the text of this document to enhance clarity.
- 4 Jan 2012: This version of the explanatory supplement released with updated v1.3 catalogs. The convention for GAU_THETA and BEAM_THETA was incorrect in the catalogs from 11 Jan 2011. For GAU_THETA, the reference angle corresponding to 0° was offset from North by 90°. For BEAM_THETA, the reference angle was correct (i.e. 0° was in the direction North), but the values were given a range of -90° to +90° instead of 0° to 180°. In addition, the DATESOBS and NUMOBS fields did not include the dates corresponding to the *Planck* First Light Survey. The DATESOBS field was also found to be incorrect by larger than a day in many cases since it was derived from planned pointing files instead of actual pointing files. These four catalog quantities have been updated in the revised v1.3 catalogs. The color corrections for the LFI flux densities were described in the earlier version of the explanatory supplement as multiplicative while they were in fact, divisive. The numbers appropriate for multiplicative corrections have replaced the previous ones in Table 14. To illustrate the magnitude of the effect, for a source with $S_\nu \propto \nu^{-1}$ spectrum, using the incorrect numbers would have resulted in a 30 GHz flux density which was a factor of 1.1 (0.953^{-2}) too high compared to the true flux density of the source. There is no change in the number of sources or the other columns compared to the v1.2 catalogs.
- 11 Jan 2011: First release with v1.2 of the catalogs.

Contents

1 Introduction **9**

2 Summary of ERCSC Data Products **11**

2.1 Individual Frequency Source Lists 11

2.2 Cold Cores and Galaxy Cluster Candidates 11

3 User's Guide to ERCSC **12**

3.1 Usage of the Source Lists 12

3.2 Cautionary Notes 16

4 *Planck* Data Sets **21**

4.1 LFI 21

4.2 HFI 22

4.3 Specification of Input Maps 23

5 ERCSC Data Processing **26**

5.1 Source Detection 26

5.2 Source Extraction 27

5.2.1 Aperture Photometry 27

5.2.2 Moment Analysis 27

5.2.3 Gaussian Fitting 28

5.2.4 PSF Fitting 29

5.3 Bandfilling 29

6 Detection Algorithms **33**

6.1 PowellSnakes 33

6.2 SExtractor 35

6.2.1 Flat Patches 35
6.2.2 The Method 35
6.2.3 Tuning of SExtractor for ERCSC 36

7 Quality Assessment Cuts **39**
7.1 The Monte-Carlo QA Approach 39
7.1.1 Technique 40
7.1.2 Background Thresholding 40
7.1.3 Flux Accuracy 42
7.1.4 Performance of Codes 43
7.1.5 Positional Accuracy and Flux Density Limit 44
7.2 Secondary Quality Assessment Cuts 54
7.3 CMB Subtraction 64

8 Characterization of ERCSC Between the *Planck* Bands **66**

9 Validation of ERCSC with Ancillary Catalogs **66**
9.1 Positional Accuracy 70
9.2 Comparison Between *Planck* and WMAP 70
9.3 Assessment of Flux Densities with a Predictive Flux Catalog 80

10 Contents of ERCSC **84**
10.1 ERCSC FITS Header 84
10.2 ERCSC Table Format 85
10.3 Postage Stamps and Skymaps 88
10.3.1 Postage Stamps 88
10.3.2 Skymaps 88
10.4 Notes on Individual Sources 89

10.5 Color Corrections 90

11 The *Planck* Early Cold Cores Catalog **92**

11.1 Introduction 92

11.2 Source Detection 92

11.3 ECC Monte Carlo Quality Assessment 93

11.4 Delivered ECC 98

11.4.1 Catalog Contents 98

11.4.2 Catalog Format 98

11.5 Postage Stamps and Skymaps 102

11.5.1 Postage Stamps 102

11.5.2 Skymaps 102

11.6 Notes on the Catalog 102

11.6.1 Sources with Negative 100 μm Flux Densities 102

11.6.2 Contents of the ECC Notes File 103

12 The *Planck* Early Sunyaev-Zel'dovich Detected Cluster Candidates **105**

12.1 Introduction 105

12.2 The Generation of the ESZ List 106

12.3 Usage of the ESZ List 109

12.4 Notes on Individual Clusters 110

A Glossary **120**

List of Figures

1 Range in sensitivity of *Planck* maps 18

2 HFI bandpasses 20

3 Comparison between bandfilled and individual frequency flux densities . . . 32

4 SExtractor flowchart 37

5 Example of background threshold maps 41

6 Comparison between performance of codes from the Monte-Carlo analysis . . 45

7 Flux density limit and positional accuracy of catalogs derived from Monte-Carlo analysis 55

8 Spectral indices of *Planck* sources 68

9 Same as figure 8, but for sources for which $30° < |b| < 90°$ 69

10 Astrometric accuracy of ERCSC 72

11 Comparison between ERCSC and WMAP 74

12 Comparison between ERCSC and WMAP 75

13 Sky distribution of 30 GHz *Planck* Sources 76

14 Sky distribution of 44 GHz *Planck* Sources 77

15 Sky distribution of 70 GHz *Planck* Sources 78

16 Sky distribution of 100 GHz *Planck* Sources 79

17 Flux accuracy through comparison with external catalogs 81

18 SEDs of predictive flux catalog sources 83

19 ECC photometric accuracy versus SNR 94

20 ECC photometric accuracy versus temperature 95

21 ECC recovery of fitted parameters 96

22 ECC reliability calibration 97

23 Sky distribution of ECC sources 98

24 Very cold sources in the ECC 103

25 Sky distribution of ESZ cluster candidates 111

26 Redshift distribution of ESZ cluster candidates 111

27 Postage stamp cutouts of representative ESZ clusters 112

28 Reconstructed Compton-y maps for representative ESZ clusters 113

List of Tables

1 *Planck* In-Flight Specifications and ERCSC Sensitivity 10

2 All-Sky and High-Latitude Source Statistics in ERCSC 18

3 ERCSC Delivery Contents 19

4 Center Frequencies and Multiplicative Conversion Factors 25

5 Gaussian Fitting Parameters 30

6 PSF Fitting Parameters 30

7 Key Configuration Parameters 36

8 Source Matches in Adjacent Bands 67

9 QSO Matches in ERCSC Catalogs 70

10 Predictive Flux Catalog 82

11 ERCSC FITS Header Contents 84

12 ERCSC FITS Binary Table Contents 86

12 ERCSC FITS Binary Table Contents 87

13 Example of Notes for ERCSC 30 GHz Sources 91

14 Color Corrections 91

15 ECC FITS Binary Table Primary Header 99

16 ECC FITS Binary Table Extension Contents 100

17 ESZ Catalog Columns 119

1. Introduction

Planck is a European Space Agency (ESA) mission, with significant contributions from the U.S. National Aeronautics and Space Agency (NASA). It is the third generation of space-based cosmic microwave background experiments, after the Cosmic Background Explorer (*COBE*) and the Wilkinson Microwave Anisotropy Probe (*WMAP*). *Planck* was launched on 14 May 2009 on an Ariane 5 rocket from Kourou, French Guiana. Following a cruise to the Earth-Sun L2 Lagrange point, cooling and in orbit checkout, *Planck* initiated the First Light Survey on 13 August 2009. Since then, *Planck* has been continuously measuring the intensity of the sky over a range of frequencies from 30 to 857 GHz (wavelengths of 1 cm to 350 μm) with spatial resolutions ranging from $\sim 33'$ to $\sim 5'$ respectively (Table 1). The Low Frequency Instrument (LFI) on *Planck* provides temperature and polarization information using radiometers which operate between 30 and 70 GHz. The High Frequency Instrument (HFI) uses pairs of polarization-sensitive bolometers at each of four frequencies between 100 and 353 GHz but does not measure polarization information in the two upper HFI bands at 545 and 857 GHz. The lowest frequencies overlap with WMAP, and the highest frequencies extend far into the submillimeter in order to improve separation between Galactic foregrounds and the cosmic microwave background (CMB). By extending to wavelengths longer than those at which the Infrared Astronomical Satellite (*IRAS*) operated, *Planck* is providing an unprecedented window into dust emission at far-infrared/submillimeter wavelengths.

The *Planck* Early Release Compact Source Catalogue (ERCSC) is a list of all high reliability sources, both Galactic and extragalactic, derived from the first sky coverage. The data that went into this early release comprise all observations undertaken between 13 August 2009 and 6 June 2010, corresponding to *Planck* operational days 91−389. Since the *Planck* scan strategy results in the entire sky being observed every 6 months, the data considered in this release correspond to more than the first sky coverage. Table 1 provides the fraction of the sky that has coverage in this early release. The source lists have reliability goals of $> 90\%$ across the entire sky and $> 95\%$ at high Galactic latitude. The goals on photometric accuracy are 30% while the positional accuracy goal translates to a positional root mean square (RMS) uncertainty that is less than 1/5 of the beam full width at half maximum (FWHM).

Table 1 gives the nominal frequencies, wavelengths, and beam sizes in each of the 9 frequency bands together with three different measures of the sensitivity of the ERCSC. Early science results from the first *Planck* data release can be found in *Planck* Collaboration (2011a–u).

Table 1. *Planck* In-Flight Specifications and ERCSC Sensitivity

Channel	1	2	3	4	5	6	7	8	9
Band [GHz]	30	44	70	100	143	217	353	545	857
λ [μm]	10000	6818	4286	3000	2098	1382	850	550	350
Sky Coverage (%)	99.96	99.98	99.99	99.97	99.82	99.88	99.88	99.80	99.79
Beam FWHM [$'$][a]	32.65	27.00	13.01	9.94	7.04	4.66	4.41	4.47	4.23
10σ[b] [mJy]	1173	2286	2250	1061	750	807	1613	2074	2961
10σ[c] [mJy]	487	1023	673	500	328	280	249	471	813
Flux Density Limit[d] [mJy]	480	585	481	344	206	183	198	381	655

[a]The precise beam values are presented in Zacchei et al. (2011) and Planck HFI Core Team (2011b). This table shows the values which were adopted for the ERCSC.

[b]Flux density of the median $>10\sigma$ source at $|b| > 30^\circ$ in the ERCSC. σ is the photometric noise which is a combination of sky background and instrument noise.

[c]Flux density of the faintest $>10\sigma$ source at $|b| > 30^\circ$ in the ERCSC.

[d]Faintest source at $|b| > 30^\circ$ in the ERCSC.

2. Summary of ERCSC Data Products

In this section, we summarize the data products associated with the *Planck* Early Release Compact Source Catalogue (ERCSC). A full description can be found in Section 10. The entire catalogue is available from both the ESA *Planck* Legacy Archive[1] and the NASA Infrared Science Archive[2].

2.1. Individual Frequency Source Lists

The ERCSC consists of single frequency source lists, one at each of the *Planck* frequencies. The source lists are FITS tables and contain 35 columns per source at the LFI bands and 36 columns at the HFI bands. The one additional column for the HFI bands compared to the LFI bands is due to the inclusion of a cirrus estimate, described below. The 857 GHz source list has six additional columns which give the flux densities and flux density uncertainties at the three adjacent lower frequencies, 217, 353 and 545 GHz for each source detected at 857 GHz. The number of sources in the lists range from 705 at 30 GHz to 8988 at 857 GHz (Table 2).

Maps of the sky distribution of sources in Galactic coordinates are provided. In addition, we also provide for each source in the catalogue, a postage stamp cutout of the source from the all sky intensity map of the corresponding frequency, after a model for the CMB has been subtracted. The size of the cutout is 4×FWHM at the corresponding frequency and is linear in intensity. The primary purpose of these cutouts is to aid in the visual validation of sources. We also provide notes in text files, one per frequency, which gives possible associations of the ERCSC sources with sources in ancillary catalogues, as well as potential variability information.

2.2. Cold Cores and Galaxy Cluster Candidates

Two additional catalogues which consist of a list of Cold Cores of interstellar molecular clouds within the Galaxy and a list of galaxy clusters detected through the Sunyaev-Zel'dovich effect, are provided. These are candidate sources that have been detected using multifrequency algorithms that use the distinct spectral signature of such sources through the

[1]http://www.sciops.esa.int/index.php?project=planck&page=Planck_Legacy_Archive

[2]http://irsa.ipac.caltech.edu/Missions/planck.html

Planck frequency channels to identify them. The number of sources in the early Cold Cores (ECC) list and the early Sunyaev-Zel'dovich (ESZ) cluster list are 915 and 189 respectively.

The sky distribution of the ECC and ESZ sources in Galactic coordinates are also provided. Image cutouts of the ECC candidates at the three upper HFI bands are provided on the same spatial scale as for the 9 single frequency sources. The ESZ candidates do not have associated cutouts since the multifrequency maps themselves have low utility for the visual validation of clusters. Ancillary X-ray data which were used for the validation of the majority of the clusters are discussed in these release notes. Notes for both the ECC and ESZ sources are also provided.

The entire data release thus consists of 11 source list files, 11 source distribution maps on the sky, 11 notes files and postage stamp cutouts of all the sources detected at the nine individual frequencies as well as in the ECC list. A full listing of the data products is provided in Table 3.

3. User's Guide to ERCSC

3.1. Usage of the Source Lists

The relative contributions of astrophysical sources of "noise" such as the cosmic microwave background and the emission from the Galactic interstellar medium (ISM) vary across the *Planck* frequencies. The CMB contribution peaks between 100 and 143 GHz while the ISM contribution is highest above 857 GHz. These variations in the sources of noise have motivated two separate detection algorithms for the ERCSC. The PowellSnakes (PwS) source detection algorithm was used at frequencies ≤ 143 GHz while the SExtractor algorithm was adopted for frequencies ≥ 217 GHz. The algorithms are described in Section 6. However, it should be noted that PwS has been evolving since the ERCSC runs were performed. The improvements implemented in the code as a result of the knowledge gained from the ERCSC runs, might result in significantly different performance in future runs.

The key columns in the ERCSC are:

1. source identification: NAME (string)
2. position: GLON, GLAT, POS_ERR which gives the Galactic coordinates in degrees and the estimated 1σ positional uncertainty in arcminutes.
3. flux density: FLUX, FLUX_ERR in mJy measured in a circular aperture with radius equal to the nominal FWHM of the beam.

Individual sources can be searched for in the list either by Galactic coordinates GLON, GLAT, or by the equivalent J2000 equatorial coordinates RA, DEC. POS_ERR is in arcminutes, and depends on the local background RMS and SNR. This uncertainty is only a measure of the uncertainty for fitting the location of the source in the maps and does not take into account any astrometric offset in the maps. Furthermore, POS_ERR is measured from the positional uncertainty of artificial point sources injected into the maps. As a result, extended sources might have larger positional uncertainties which are not reflected in this value.

When a source is classified as extended, the EXTENDED column is set to 1. This implies that the square root of the product of the major and minor axes of the source is 1.5 times larger than the square root of the product of the major and minor axes of the estimated *Planck* point spread function at the location of the source. That is,

$$\sqrt{\text{GAU\_FWHMMAJ} \times \text{GAU\_FWHMMIN}} > 1.5 \times \sqrt{\text{BEAM\_FWHMMAJ} \times \text{BEAM\_FWHMMIN}} \quad (1)$$

At the upper HFI bands, sources which are extended are frequently associated with structure in the Galactic interstellar medium. Some individual nearby galaxies are also extended sources at the spatial resolution of *Planck*.

Four measures of flux density are provided, all in mJy. These flux density values all have a local background subtracted but have not been color corrected. Users should identify appropriate color corrections from Section 10.5 and apply them to the flux densities.

1. The FLUX and FLUX_ERR columns give the flux densities, measured in an aperture of radius the nominal sky-averaged FWHM. Appropriate corrections have been applied for the flux outside the aperture assuming that the source profile is a point source.

2. The PSFFLUX and PSFFLUX_ERR columns give flux densities estimated by fitting the source with the *Planck* point spread function at the location of the source.

3. The GAUFLUX and GAUFLUX_ERR columns give flux densities estimated by fitting the source with an elliptical Gaussian model.

4. The FLUXDET and FLUXDET_ERR columns give the flux densities estimated by the native detection algorithm. For the frequencies at which PwS is used, this is estimated by using the posterior distribution of all parameters for the matched filter, while for frequencies at which SExtractor is used, it is the flux density in an elliptical Kron aperture, i.e., FLUX_AUTO. The FLUXDET values at the frequencies where PwS is used have been corrected for an average bias that was seen in the difference between

the extracted and input flux density of the Monte Carlo sources. This is most likely due to an inaccurate representation of the true beam inside the PwS detection algorithm. We do not recommend using the PwS FLUXDET values unless the source is known to be a point source and in low background regions of sky, in which case the flux density is found to be in good agreement with FLUX. For faint extended sources in the upper HFI frequencies, the SExtractor FLUXDET values might be useful.

For extended sources, both FLUX and PSFFLUX will likely be significant underestimates of the true source flux density. Furthermore, at faint flux densities corresponding to low signal-to-noise ratios (< 20), the PSF fit might have failed. This would be represented either by a negative flux density, or a NaN, or by a significant difference between the PSFFLUX and FLUX values. In general, for bright extended sources, we recommend using the GAUFLUX and GAUFLUX_ERR values although even these might be biased high if the source is located in a region of complex, diffuse foreground emission.

Uncertainties in the flux density measured by each technique are reflected in the corresponding "_ERR" column. The flux uncertainties derived from the artificial point sources injected into the maps are available in MCQA_FLUX_ERR. MCQA_FLUX_ERR is the standard deviation of $(S_{input}-S_{output})/S_{input}$ and is therefore dimensionless. Here, S_{input} is the injected flux density of an artificial source, and S_{output} is the extracted flux density of the source. The flux density measures used for the estimate of MCQA_FLUX_ERR are based on the aperture flux density (i.e., FLUX) at the signal-to-noise ratio of the source. The most conservative flux uncertainty is the quadrature sum of the Monte Carlo estimate of the flux density uncertainty (i.e., MCQA_FLUX_ERR converted into an uncertainty in S_{output}) and the "_ERR" value relevant for the appropriate flux density (FLUX, PSFFLUX, GAUFLUX or FLUXDET).

MCQA_FLUX_BIAS provides the median in the difference between the injected flux density and extracted aperture flux density of the artificial point sources i.e. median of $(S_{input}-S_{output})/S_{input}$. In principle, the bias should be close to zero if the aperture corrections are precisely known, the aperture is perfectly centered on each source and the background can be precisely estimated. In reality, there is an offset of a few percent, which can become large at the lowest signal to noise ratios or in high background regions. This is a median offset estimated as a function of signal to noise ratio from the artificial point sources, and has already been applied to the FLUX value of all sources. The bias correction has been applied such that the FLUX in the catalogue is the measured flux density divided by (1−MCQA_FLUX_BIAS) which typically has increased the value of the flux density.

The 1σ point source flux uncertainty due to structure in the background is given in BACKGROUND_RMS in units of mJy. At the lowest frequencies this is a combination of

CMB noise and instrumental noise, with the latter dominating. At 143 GHz, the noise is dominated by the CMB. At the highest frequencies, it is dominated by Galactic ISM. The ratio of source flux density to BACKGROUND_RMS is the primary parameter which is used to calibrate the RELIABILITY of sources.

The dates on which the source was observed are included in DATESOBS (UTC) in the yyyymmdd format. This will be useful in the analysis of time variable sources. The flux density value in the ERCSC is an average over all the dates of observations. The DATESOBS values provided are the dates on which the source centroid was separated from the beam center to within a radius of the beam half-width at half-maximum at the corresponding frequency (Table 3; Planck Collaboration 2011a). For example, a DATESOBS entry of 20100114 means that the axis of one or more of the horns for the selected band passed within 0.5×FWHM of the position of the source given in the ERCSC at some time between 0h and 24h TAI (International Atomic Time) on 2010-01-14. Due to the arrangement of the focal plane, this date might correspond to the middle of a range of dates over which the Planck beams traversed through the source.

Sources in the HFI bands each have a CIRRUS number which is based on the number of sources (both low and high reliability) within a 2° radius of the source, in raw 857 GHz catalogues derived from the maps. The number has been normalized to a peak value of unity. The normalization factor is derived from the number density of sources in the Large Magellanic Cloud region where the maximum number of 857 GHz sources are located.

Finally, each source has a CMBSUBTRACT flag. This flag has values of 0, 1 or 2. The value is 0 if the source is detected in the CMB subtracted maps (See Section 7.3) and has an aperture flux density difference $|(S_{\rm intensity} - S_{\rm nocmb})/S_{\rm intensity}| < 30\%$ where $\rm S_{intensity}$ is the FLUX of a source in the intensity maps and $\rm S_{nocmb}$ is the FLUX of the same source in the CMB subtracted maps. The value is 1 if the source is detected in the CMB subtracted maps but has a flux difference of $> 30\%$. The value is 2 if the source is not detected in the CMB subtracted maps. CMB subtraction results in artifacts in the maps which might remove real sources. It is recommended that a conservative user who wants a guarantee of source detection in follow up observations neglect sources with CMBSUBTRACT=2.

Planck Collaboration (2011c) is an abbreviated version of this explanatory supplement and can be referenced in papers that use the ERCSC, ECC or ESZ catalogues. *Planck* Collaboration (2011s) and *Planck* Collaboration (2011d) discuss the properties of the ECC and ESZ catalogues respectively.

3.2. Cautionary Notes

In this section, we list some cautionary notes associated with usage of the ERCSC list.

- *Statistical Character:* The ERCSC list is an early list of highly reliable sources from the first *Planck* all sky survey. It is not a flux density limited sample or even a complete sample of sources and therefore care should be taken before undertaking statistical studies such as source counts. This is partly due to the fact that the scan strategy results in significant variation in instrumental sensitivity as a function of position on the sky. In addition, the relative contribution of astrophysical sources of "noise" such as the CMB and the emission from the Galactic interstellar medium (ISM) vary across the *Planck* frequencies. The CMB contribution peaks between 100 and 143 GHz while the ISM contribution peaks above 857 GHz. In conjunction with the varying spatial resolution, this results in varying limits to the sensitivity of sources that can be detected both as a function of position on the sky and as a function of frequency. The Monte-Carlo analysis presented later, does quantify this variation in sensitivity for the overall catalogue. However, the estimates for the fraction of sky area above a particular completeness limit, have not been factored into the catalogue.

- *Variability:* At radio frequencies, many of the extragalactic sources are highly variable. A small fraction of them vary even on time scales of a few hours based on the brightness of the same source as it passes through the different *Planck* horns. Follow-up observations of these sources might show significant differences in flux density compared to the values in the data products. Although the maps used for the ERCSC are based on 1.6 sky coverages i.e. 60% of the sky has been observed a second time by *Planck*, the ERCSC provides only a single average flux density estimate over all *Planck* data samples that were included in the all sky maps and does not contain any measure of the variability of the sources. The *Planck* Quick Detection System (QDS; Aatrokoski et al. 2010) attempts to quantify the variability of sources seen by *Planck*. The information from the QDS has been included in the notes for certain sources.

- *Contamination from CO:* At infrared/submillimeter frequencies ($\geq$ 100 GHz), the *Planck* bandpasses straddle energetically significant CO lines (Figure 2). The effect is the most significant at 100 GHz, where the line might contribute as much as 50% of the measured flux density. Follow-up observations of these sources, especially those associated with Galactic star-forming regions, at a similar frequency but different bandpass, should correct for the potential contribution of line emission to the continuum flux density of the source. See *Planck* HFI Core Team (2011b) for details.

- *Photometry:* Each source has multiple measures of photometry: FLUX, GAUFLUX, PSFFLUX and FLUXDET, as defined above. The appropriate photometry to be used depends on the nature of the source. For sources which are unresolved at the spatial resolution of *Planck*, FLUX and PSFFLUX are most appropriate. For faint resolved sources in the upper HFI bands, FLUXDET, which is the flux density in an elliptical Kron aperture provided by SExtractor, might give the most accurate numbers. The user should also note that the requirements for the ERCSC are a flux density accuracy of $\lesssim$30% although the absolute calibration of *Planck* is known to far greater precision.

- *Cirrus/ISM:* A significant fraction of the sources detected in the upper HFI bands could be associated with Galactic ISM features or cirrus. The IRAS 100 μm surface brightness in MJy/sr for each of the sources, which is commonly used as a proxy for cirrus, is available through an online search of the ERCSC with IRSA. Candidate ISM features can be selected by choosing objects with EXTENDED=1 although Galactic and nearby extragalactic sources which are extended at *Planck* spatial resolution will meet this criterion. Alternately, the value of CIRRUS in the catalogue can be used to flag sources which might be clustered together and thereby associated with ISM structure.

- *Cold Core Temperatures:* The estimated temperatures of the Cold Cores are uncertain because of the degeneracy between the emissivity index and temperature. This results from that fact that the fit employs only one flux density estimate at wavelengths shortward of the peak in the blackbody spectrum. This issue is discussed in detail in *Planck* Collaboration (2011s).

Table 2. All-Sky and High-Latitude Source Statistics in ERCSC

Band [GHz]	Number of Sources	
	All Sky	$\|b\| > 30°$
030	705	307
044	452	143
070	599	157
100	1381	332
143	1764	420
217	5470	691
353	6984	1123
545	7223	2535
857	8988	4513

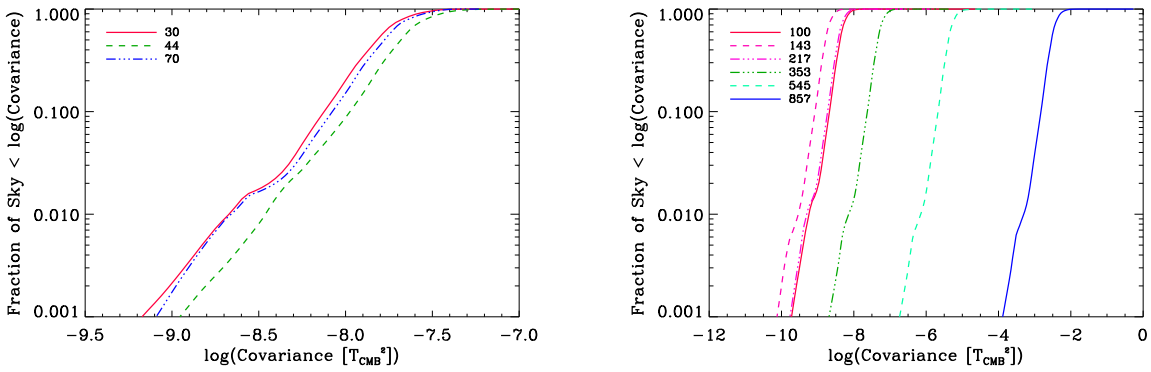

Fig. 1.— The variance in units of Kelvin^2 per pixel across the entire sky with the left panel showing the variance for the LFI frequencies and the right panel showing the variance for the HFI frequencies. At any single frequency, the variance in the all sky maps span almost two orders of magnitude over the entire sky.

Table 3. ERCSC Delivery Contents

File Name	Description
Documentation – documents/	
explanatory_supplement.pdf	This file
Source Lists – catalogs/	
ERCSC_f030.fits	30 GHz PwS-based list
ERCSC_f044.fits	44 GHz PwS-based list
ERCSC_f070.fits	70 GHz PwS-based list
ERCSC_f100.fits	100 GHz PwS-based list
ERCSC_f143.fits	143 GHz PwS-based list
ERCSC_f217.fits	217 GHz SExtractor-based list
ERCSC_f353.fits	353 GHz SExtractor-based list
ERCSC_f545.fits	545 GHz SExtractor-based list
ERCSC_f857.fits	857 GHz SExtractor-based list, *includes 217, 353, 545 GHz aperture photometry at the location of 857 GHz sources*
ECC.fits	Cold Cores list
ESZ.fits	SZ Cluster list
Images of Sky Distribution – skymaps/	
ERCSC_f030_skymap.pdf	
...	
ERCSC_f857_skymap.pdf	
ECC_skymap.pdf	
ESZ_skymap.pdf	
Collated Source Postage Stamps – cutouts/	
ERCSC_f030_cutouts.pdf	CMB subtracted postage stamps of sources
...	
ERCSC_f857_cutouts.pdf	
ECC_cutouts.pdf	ECC postage stamps from maps at 353, 545, 857 GHz
ERCSC_f030_psf_cutouts.pdf	postage stamps of *Planck* PSF at location of source
...	
ERCSC_f857_psf_cutouts.pdf	
Notes on Individual Sources – notes/	
ERCSC_f030_notes.txt	
...	
ERCSC_f857_notes.txt	
ECC_notes.txt	
ESZ_notes.txt	

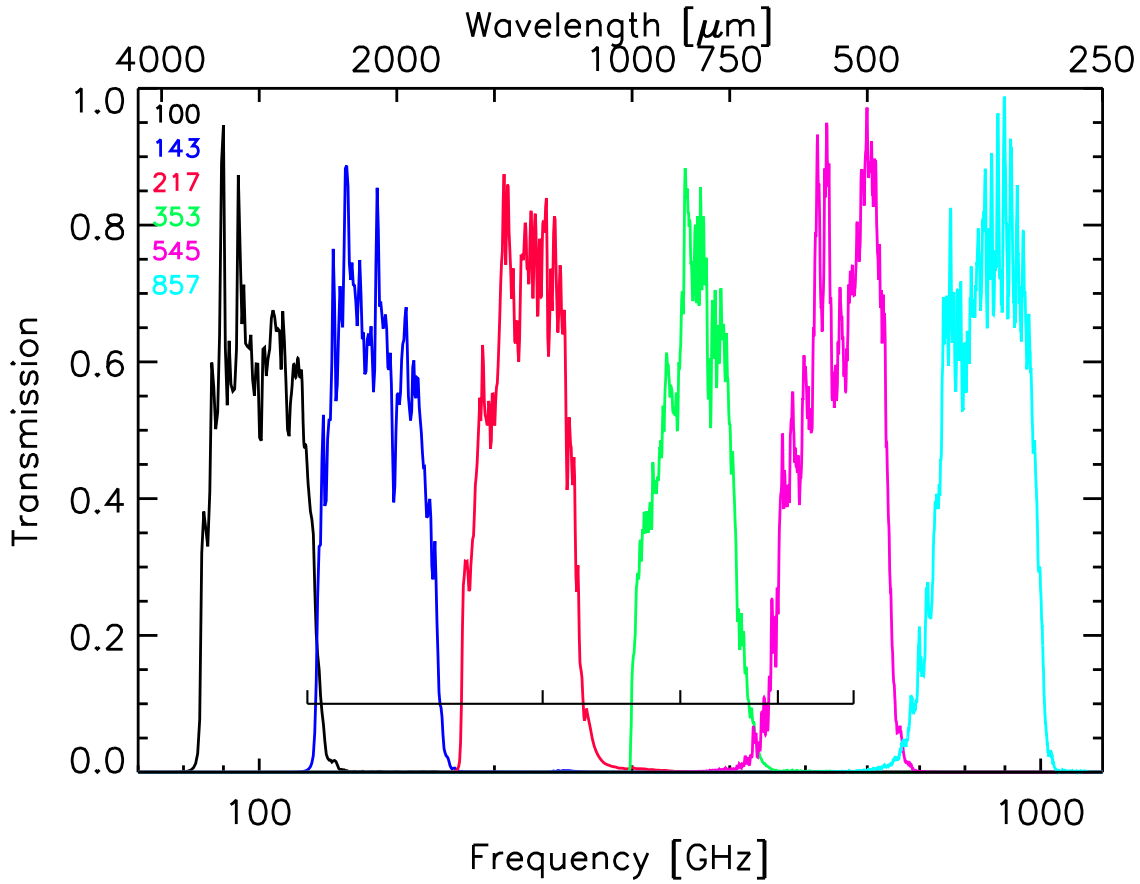

Fig. 2.— Bandpasses of HFI with the location of bright CO rotational lines ($J = 1 \rightarrow 0$, $2 \rightarrow 1$, $3 \rightarrow 2$, $4 \rightarrow 3$, and $5 \rightarrow 4$ from left to right) shown as the horizontal black line with tick marks. The CO lines can introduce a significant positive bias in the flux density of the sources, particularly those associated with Galactic star-forming regions. The effect is the most significant at 100 GHz.

4. *Planck* Data Sets

The ERCSC was generated from full-sky intensity maps per frequency that were produced at the *Planck* LFI & HFI data processing centers (DPCs). The two *Planck* instruments utilize different detector technology and read-out schemes requiring separate, specialized processing. The processes are described in detail in the companion papers (Zacchei et al. 2011; Planck HFI Core Team 2011b), but we summarize the important steps here. Both pipelines have the same broad outline:

- Re-assemble raw, time-ordered information (TOI) from the satellite packets
- Clean instrumental effects from the timelines (TOI processing)
- Determine focal plane offsets and beam shapes from local maps of planet observations
- Characterize noise properties
- Photometric calibration (against the dipole for frequencies < 500 GHz)
- Full-sky mapmaking using destriping methods
- Jack-knife validation by differencing 1st & 2nd half of each pointing period
- Subtraction of CMB component from the entire ensemble of frequency maps

The most computationally-expensive part of both pipelines is the mapmaking, requiring operations on the entire pointing history and TOI. Both LFI and HFI data processing pipelines employ destriping algorithms that allow a solution to be determined by practical project-sized computing resources (see Ashdown et al. 2007). Destriping assumes that *Planck*'s stability and redundant scan-strategy allow the noise to be approximated by a low-frequency offset and a high-frequency uncorrelated white component. The map can then be obtained by solving for the offsets and then simply binning the offset-subtracted TOI.

4.1. LFI

The LFI DPC is a distributed structure including three sites: Geneva (ISDC), Trieste (OAT and SISSA) and Garching (MPA), with significant contributions from *Core Team* members at other sites. The main TOI processing steps are:

- Time-domain subtraction of signal contamination from the unshielded housekeeping clock (44 GHz channels only; Meinhold et al. 2009)
- Differencing of sky signal against 4K reference load to reduce 1/f noise (after calculation of nulling gain factor per pointing period)
- Combination of the two output diodes for 100% duty cycle and $\sqrt{2}$ noise reduction (after relative noise weighting, fixed for entire mission)

Points of note within the later steps are:

- Focal plane/beam reconstruction using Jupiter, the brightest source in the sky
- Mars, Jupiter & Saturn are flagged before mapmaking within a region 3 times the angular extent of Jupiter
- Iterative calibration/removal of both the Cosmological and orbital dipoles following WMAP first year procedure (Hinshaw et al. 2003). This is initially determined per pointing period then refined by a multi-element smoothing scheme to reduce noise.
- Mapmaking using version 3.6.2 of the `Madam` code (see Keihänen et al. 2010, and references therein), using one minute baselines and uniform weighting between radiometers

4.2. HFI

The HFI DPC is organized as an international consortium coordinated from the IAP (Paris, France) with the help of the IAS (Orsay, France). The major TOI cleaning steps are:

- Demodulation of readout AC bias then low-pass filtering to remove the 90.19 Hz modulation carrier
- Removal of cosmic rays glitches. Cosmic rays are identified by iterative estimation of the true sky signal using the scan strategy redundancy. The strongest part of the glitches is flagged ($10 - 15\%$ of the data) and tails of the glitches are subtracted by stacked template fitting.
- Correction of the non-linear response of the bolometer to strong sources (order of few 10^{-4} for Galaxy or dipole) by an instrumental gain model

- Removal of temperature fluctuations (and reduction in low-frequency 1/f noise) of the 103 mK bolometer plate by decorrelating the dark bolometer signals
- Removal of narrow spectral lines due to pickup from the mechanical 4K cooler by subtraction of Fourier series components from time-line data. Rare resonance between these lines, strong sources and the spin frequency which required masking in the final maps (see Section 7.2 and *Planck* HFI Core Team 2011b)
- Decorrelation of temporal transfer (see Planck HFI Core Team 2011a)

Differences between LFI and HFI processing in the later steps include:

- Focal plane/beam reconstruction using Mars & Saturn rather than Jupiter, which would drive some detectors into the non-linear regime.
- All planets Mars-Neptune are flagged from the data (to twice the beam extent), along with 27 asteroids which are flagged to 1.5 times the beam extent
- Three detectors (143-8, 545-3 & 857-4) are dropped from analysis due to their noise properties
- The data is binned into ring objects (same binning as final maps in order to avoid additional pixelization effects) as an intermediate step before mapmaking, increasing signal to noise for calibration and reducing the amount of data to be handled
- Frequencies 353 GHz and below are photometrically calibrated by χ^2 minimization of rings against the WMAP Cosmological dipole. The Cosmological and orbital dipoles are subtracted from the rings before mapmaking
- The 545 & 857 GHz channels are calibrated in the map plane by correlation against FIRAS which is dependent on a detailed knowledge of the HFI bandpasses and FIRAS beams
- Mapmaking by an internal destriper code `polkapix` and inverse noise weighting between bolometers

4.3. Specification of Input Maps

The ERCSC pipeline thus starts with clean and consistent data compressed to map form. The specification of the maps were:

- Temperature only - polarization is beyond the scope of this early analysis
- Full-sky maps. The input maps were constructed from almost 300 days of data from continuous observations between 2009 August 12 until 2010 June 6 for HFI and 2009 August 12 until 2010 June 7 for LFI (*Planck* mission operational days 91-389, rings 240-9466). This is ∼1.6 sky surveys (*Planck* scans the entire sky in 6 months). While the entire sky was observed, there are a few small gaps in the final maps due to flagging of data, particularly around the planets. Sky coverage numbers are listed in Table 1; the lowest is 99.79% at 857 GHz.
- A single map per frequency band merging all detectors
- Matching covariance maps required by the SExtractor algorithm (see Section 6.2.3)
- Both pre & post CMB-subtraction; the ERCSC is based on maps with the CMB present but the CMB subtracted maps were run through the ERCSC pipeline and a CMBSUBTRACT flag is provided for each source as explained in Section 3.1.
- HEALPix-format (Górski et al. 2005)
- The 30, 44, and 70 GHz LFI maps were supplied as $N_{side} = 1024$, corresponding to a pixel scale of $3.4'$ per pixel.
- The HFI maps at 100, 143, 217, 353, 545, and 857 GHz were pixelized at $N_{side} = 2048$ corresponding to $1.7'$ pixels to match the smaller beam FWHM at those frequencies
- The maps were in Galactic coordinates
- The maps were calibrated in K_{CMB}
- The planets were removed

The maps are then converted from K_{CMB} to K_{RJ}, a unit of brightness temperature, using the conversion factors in Table 4. These K_{RJ} maps are input to the ERCSC pipeline which makes the appropriate conversions from K_{RJ} to mJy. Given that flux densities in the ERCSC are stated in mJy and the characteristic beam and source sizes vary with position on the sky, users of the ERCSC may note that MJy sr^{-1} values can be directly converted to mJy arcmin^{-2} by multiplying by 84.615956. For details, the user is referred to Zacchei et al. (2011) and *Planck* HFI Core Team (2011a and 2011b).

Table 4. Center Frequencies and Multiplicative Conversion Factors

Band Name	Center Frequency [GHz]	K_{CMB} to K_{RJ}	K_{RJ} to MJy sr^{-1}
030	28.5	0.979328	24.845597
044	44.1	0.95121302	59.666236
070	70.3	0.88140690	151.73238
100	100	0.76581996	306.81118
143	143	0.59714682	627.39818
217	217	0.31573332	1444.7432
353	353	0.071041398	3823.1434
545	545	0.0059757149	9113.0590
857	857	9.6589431e-05	22533.716

5. ERCSC Data Processing

The ERCSC is generated by a multi-step pipeline that takes as input the HEALPix formatted all-sky maps and produces as output a FITS binary table file for each of the nine Planck bands. The three core processing steps within the ERCSC pipeline are source detection, source extraction, and bandfilling at 857 GHz. These three steps are first run on the intensity maps to obtain catalogs of sources. The process is then repeated on maps which have a population of artificial point sources of varying flux densities injected directly into the maps. The performance of the algorithms are evaluated based on the positions and extracted flux densities of the artificial sources whose real flux density and positions are precisely known. Based on the properties of the extracted artificial sources, signal to noise cuts are defined such that the properties of the extracted artificial sources are robust both in terms of position and flux density. The same signal to noise cut is then applied to the real catalogs of sources generated from the intensity maps to obtain high reliability catalogs.

Secondary quality assessment cuts are applied to the catalog to eliminate sources associated with known artifacts in the maps. Additional properties of the reliable sources such as the dates they were observed, their presence in CMB subtracted maps, their flux density estimated from point source fitting, and the potential contribution of cirrus are evaluated in the final stages of the pipeline. We describe the core steps in more details below; the quality assessment and selection criteria are discussed in §7.

5.1. Source Detection

Four source detection algorithms were initially run as part of the ERCSC pipeline. These are the Paris Matched Filter (Melin et al. 2006), PowellSnakes (Carvalho et al. 2009), SExtractor (Bertin & Arnouts 1996), and a Mexican Hat Wavelet code under development at Instituto de Fisica de Cantabria [IFCA; Santander] (López-Caniego et al. 2006). After comparing their performance, the PowellSnakes method was chosen for the 30 to 143 GHz channels, and the SExtractor method was chosen for the 217 GHz channel and above. A detailed description of the two detection codes and the tuning of their performance is discussed in §6.

Each of the source detection modules produces a list of sources with their positions and flux densities, which is then converted into a standard FITS binary table. The source positions are given in the FITS file in both galactic coordinates (GLON, GLAT) and celestial coordinates (RA, DEC); the source flux density and its uncertainty computed by the detection module are listed as FLUXDET and FLUXDET_ERR. These values are propagated to

the final ERCSC catalog (see Table 12).

5.2. Source Extraction

For each of the objects in the detected source catalog we apply a multi-step source extraction algorithm in order to obtain photometric, astrometric, and morphological information. The specific analysis steps we take are aperture photometry, moment analysis, general 2-D Gaussian fitting and model beam Point Spread Function [PSF] fitting.

5.2.1. Aperture Photometry

We compute the object flux density (FLUX) by subtracting an estimate of the local background from the summed flux density within a specified radius, in this case 1.0 times the beam FWHM, around the source position. The local background ($B_{aperture}$) is computed as the median flux density within a sky annulus spanning 1.0 to 2.0 times the beam FWHM, centered on the source position. Uniform weighting of the pixels is adopted.

The RMS of the background is computed as the standard deviation of the flux densities of each pixel within the sky annulus. The flux density error (FLUX_ERR) is the square-root of the sum of three terms: the first term is the product of the variance within the sky annulus and the number of pixels in the aperture; the second term is an estimate of the Poisson noise arising from the source flux density, and is set to zero since this is in general, negligibly small; the final term is the variance within the sky annulus divided by the number of sky annulus pixels and multiplied by the square of the number of pixels in the aperture.

Under the assumptions that the source is unresolved and that the beam is approximated by a circular Gaussian having the specified FWHM, the multiplicative aperture correction factor is estimated by numerically integrating the Gaussian which is then applied to the FLUX values. Naturally, if the source is extended or has a non-Gaussian profile, the aperture correction will be inaccurate. In that scenario, the user might find the GAUFLUX values based on Gaussian profile fitting (see §5.2.3) to be more relevant.

5.2.2. Moment Analysis

The moment analysis step computes the first and second order moments within the specified radius (1.5×FWHM) for each source using the background subtracted flux den-

sities. The first and second order moments can be used to estimate the centroid position and σ values for sources resembling 2-D Gaussians; in the more general case they provide information on the object position and shape.

$$M_{x1} = \frac{\int (x-x_0) f'(x,y) dxdy}{\int f'(x,y) dxdy} \quad (2)$$

$$M_{y1} = \frac{\int (y-y_0) f'(x,y) dxdy}{\int f'(x,y) dxdy} \quad (3)$$

$$M_{x2} = \sqrt{\frac{\int (x-x_0)^2 f'(x,y) dxdy}{\int f'(x,y) dxdy}} \quad (4)$$

$$M_{y2} = \sqrt{\frac{\int (y-y_0)^2 f'(x,y) dxdy}{\int f'(x,y) dxdy}} \quad (5)$$

$$M_{xy} = \sqrt{\frac{\int (x-x_0)(y-y_0) f'(x,y) dxdy}{\int f'(x,y) dxdy}} \quad (6)$$

where x_0 and y_0 are the positions determined by the previous source detection step and

$$f'(x,y) = f(x,y) - B_{aperture} \quad (7)$$

Results from the moment analysis are also propagated to the ERCSC catalog; see MX1, MY1, MXY, MX2, MY2 in Table 12. The X axis in moments corresponds to Galactic longitude while the Y axis corresponds to Galactic latitude. The sign of the moments corresponds to that of Galactic coordinates; e.g. a positive X moment implies that the centroid of the source is offset compared to the listed position estimated by the detection algorithm, in the direction East; a negative Y moment implies that the centroid of the source is offset relative to the listed position estimated by the detection algorithm, in the direction South.

5.2.3. Gaussian Fitting

The non-background-subtracted intensities around each source are fit to the sum of a general 2-D Gaussian plus linear background:

$$f(x,y) = A_{gauss} e^{-0.5\left([\frac{x'}{\sigma_x}]^2 + [\frac{y'}{\sigma_y}]^2\right)} + S_{x,gauss} x' + S_{y,gauss} y' + B_{gauss} \quad (8)$$

where

$$x' = (x - x_{0,gauss}) \cos(\theta) - (y - y_{0,gauss}) \sin(\theta) \quad (9)$$

and

$$y' = (x - x_{0,gauss})\sin(\theta) + (y - y_{0,gauss})\cos(\theta). \quad (10)$$

The fitted parameters are defined in Table 5, and the ERCSC table columns contributed by the Gaussian fitting are GAUFLUX, GAUFLUX_ERR, GAU_FWHMMAJ, GAU_FWHMMIN and GAU_THETA. As mentioned above, the flux density derived from Gauss fitting may be more appropriate to use for bright, extended sources.

5.2.4. PSF Fitting

Due to the scan strategy and the asymetric nature of the *Planck* beam, the effective point spread function varies as a function of position on the sky. The FEBeCoP algorithm (Mitra et al. 2010) has been successful in estimating the effective beam of *Planck* at each frequency at each location, we therefore adopt it to calculate the flux density from PSF fitting. The non-background-subtracted intensities for each source in the ERCSC are fit to a scaled model of the FEBeCoP derived PSF plus a linear background. The PSF is treated as a circular 2-D Gaussian having a FWHM equal to that of the *Planck* beam at that position:

$$f(x,y) = A_{psf} e^{-0.5\left([\frac{x'}{\sigma_x}]^2 + [\frac{y'}{\sigma_y}]^2\right)} + S_{x,psf}x' + S_{y,psf}y' + B_{psf} \quad (11)$$

where

$$x' = x - x_{0,psf}, \quad (12)$$

$$y' = y - y_{0,psf}, \quad (13)$$

and

$$\sigma = \frac{FWHM}{2\sqrt{2\ln(2)}}. \quad (14)$$

The definition of the fitted parameters are given in Table 6, and the ERCSC columns provided by the PSF fitting code are PSFFLUX and PSFFLUX_ERR.

5.3. Bandfilling

Bandfilling is the process by which flux density estimates at specific bands are generated based on source positions defined in another band. For the ERCSC release we compute the

Table 5. Gaussian Fitting Parameters

Column Name	Description
A_{gauss}	Amplitude in mJy/arcmin^2
B_{gauss}	Background in mJy/arcmin^2
σ_x	Semi-X Axis in arcmin
σ_y	Semi-Y Axis in arcmin
$S_{x,gauss}$	Background X-Slope in mJy/arcmin
$S_{y,gauss}$	Background Y-Slope in mJy/arcmin
$x_{0,gauss}$	X Centroid in arcmin
$y_{0,gauss}$	Y Centroid in arcmin
θ	Rotation Angle in degree

Table 6. PSF Fitting Parameters

Column Name	Description
A_{psf}	Amplitude in mJy/arcmin^2
B_{psf}	Background in mJy/arcmin^2
$S_{x,psf}$	Background X-Slope in mJy/arcmin
$S_{y,psf}$	Background Y-Slope in mJy/arcmin
$x_{0,psf}$	X Centroid in arcmin
$y_{0,psf}$	Y Centroid in arcmin

flux density at 217, 353, and 545 GHz at the positions of each source detected at 857 GHz, using aperture photometry. Bandfilling is not attempted at other frequencies due to the variation in spatial resolution across the bands, which makes multifrequency associations challenging, especially in crowded regions such as the Galactic Plane.

The source flux density is computed within a radius equal to the beam FWHM, and the background sky flux density is set as the median within radii of 1.2 and 1.7 times the beam FWHM. The original 857 GHz source catalog, combined with the aperture photometry at 217, 353, and 545 GHz, comprise the ERCSC delivered catalog at 857 GHz.

In most cases, due to centroid offsets, the flux density in the corresponding frequency catalog may be more accurate than the bandfilled flux density for the same source. Figure 3 shows the comparison between the bandfilled flux densities and the flux densities in the individual frequency ERCSC catalogs for sources that are common in the 857 GHz catalog and the lower frequency ones.

The median difference in the flux densities is $\lesssim$2.3% with the bandfilled flux densities being lower compared to the ERCSC flux densities. This is expected, since the centroid in the bandfilled flux densities is the location of the 857 GHz source; mis-centering generally results in an underestimation of the source flux density. Sources which have larger differences are close to regions of strong ISM emission where contamination by the Galaxy to the aperture photometry is substantial.

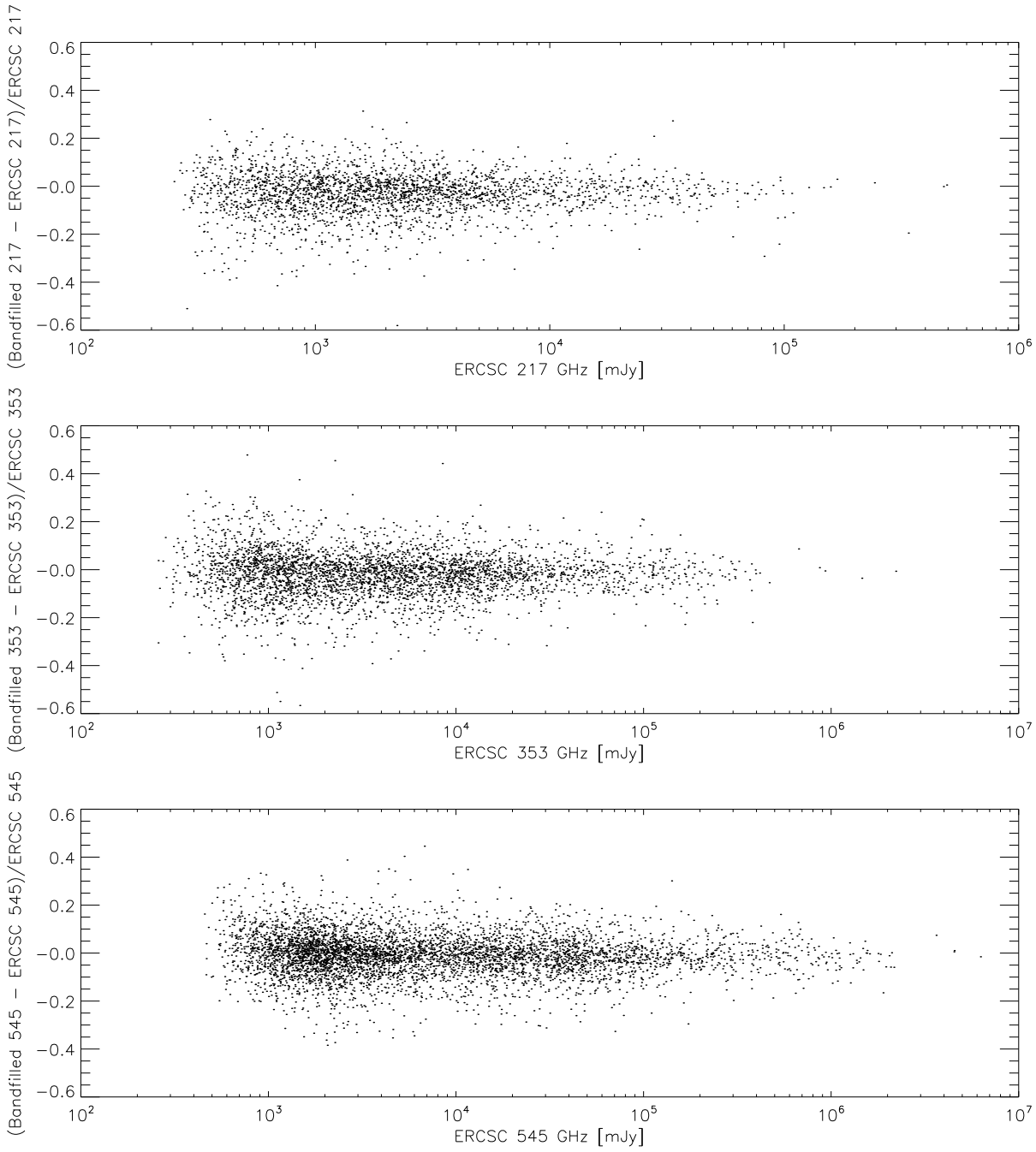

Fig. 3.— The 3 panel plot shows the comparison between bandfilled and individual frequency flux densities at 217, 353 and 545 GHz. The median difference is $\lesssim$2.3%, with the standard deviations being 9.0, 9.4 and 8.6% at 217, 353 and 545 GHz, respectively.

6. Detection Algorithms

6.1. PowellSnakes

The source detection algorithm used by the ERCSC for frequencies 30–143 GHz is PowellSnakes. PowellSnakes has been developed by Carvalho et al. (2009). It is a fast Bayesian method for the detection of discrete objects immersed in a diffuse background. For ERCSC, version 2 of the algorithm was used; this incorporates a number of improvements over version 1 (Carvalho et al., in preparation). PowellSnakes has also been extended to multi-frequency source detection, e.g., to locating candidate SZ clusters using a template spectrum, but for ERCSC it was used in a single-frequency mode. The application of Bayesian model selection and the Bayesian information criterion to source detection and extraction have been reviewed by Hobson & McLachlan (2003) and Savage & Oliver (2007). PowellSnakes builds on these ideas and incorporates them in a fast implementation.

The map is modeled as a set of discrete objects, of known shape, embedded in a stochastic background, with added instrumental noise. The object shape is chosen to be a circular Gaussian approximation to the effective PSF, and the background and instrumental noise are modeled as a Gaussian random field with power spectrum to be estimated from the data. Because both PSF and background vary with sky position, the analysis is performed on overlapping sky patches within which the properties can be assumed to be uniform. At high latitudes and low frequencies the background is dominated by the CMB, so the Gaussian assumption is a good one; near the Galactic plane, however, the background is dominated by emission from the ISM and the assumption breaks down. In practice, however, PowellSnakes gives good results, albeit less than optimum, in these cases. At the highest frequencies SExtractor was found to perform better than PowellSnakes, probably because the model of the background statistics is poor, and also because many of the sources are peaks in the ISM emission and are not well represented by the PSF model.

Given these assumptions, PowellSnakes estimates source parameters by maximizing the posterior probability (i.e., the product of the likelihood and an assumed prior). The maximization is performed using a simultaneous multiple minimization code based on Powell's direction set algorithm (hence the name) to rapidly locate the local maxima in the posterior. This novel feature makes PowellSnakes substantially faster than Monte Carlo Markov chain methods used by Hobson & McLachlan (2003). Whether or not a posterior peak corresponds to a source is determined by Bayesian model selection using an approximate evidence value based on a local Gaussian approximation to the peak. In this step, PowellSnakes minimizes the average loss matrix rather than maximizing either reliability or completeness: that is, it treats spurious detections and missing detections as equally undesirable.

In practice, PowellSnakes proceeds as follows:

1. It resamples the spherical HEALPix map on a set of overlapping flat patches (gnomonic projection). For the ERCSC runs, the patches were 256 or 512 pixels square, with a pixel width of 3.34 or 1.718 arcmin respectively. These pixels are slightly smaller than the 3.4 and 1.7 arcminute sizes of the pixels in the N_{side}=1024 and 2048 HEALPix representation of the all sky maps. It then analyzes each patch separately, merging the results at the end. PowellSnakes does not make use of the variance map, i.e., it assumes (incorrectly) that all pixels have equal weight.

2. For each patch, it estimates the power spectrum of the background. The algorithm is run iteratively, and in later iterations the sources discovered in the previous iteration are subtracted before power-spectrum estimation (very bright sources are masked rather than subtracted). The power spectrum is used with the expected Gaussian PSF to construct a matched filter that is applied to the patch map. The filtered map can be regarded as the likelihood manifold projected into the subspace of the sources' positions. Each peak in the filtered map gives the position and amplitude of a candidate source.

3. For each candidate, PowellSnakes estimates parameter values (position, amplitude, and size [Gaussian FWHM]) by Powell minimization. To assess the quality of the source, it explores the posterior distribution around the optimum parameter values and uses a generalized likelihood ratio test to accept or reject the hypothesis that a source is present at this location.

For detection of sources with high signal-to-noise ratio, PowellSnakes is fairly insensitive to the choice of priors. For v2 of the algorithm which was used for ERCSC, a flat distribution of priors was adopted with the distribution of priors on the source radius being uniform between 0 and $3.435'$ for all frequencies. We note that this is the source size before convolution with the *Planck* beam.

After merging the results from each patch, the output of PowellSnakes is a set of source positions with estimated flux densities. The *srcext* photometry algorithms are then applied at each position to obtain other measures of flux density and size, taking into account the instrumental noise in each pixel.

In tests on high-latitude regions, PowellSnakes detected more sources at the ERCSC 90% reliability threshold than two competing methods, the Matched Filter and the Mexican-Hat Wavelet filter. Both of these algorithms perform a filtering step and locate sources from peaks in the filtered map; they differ in how they estimate the filter from the data. However,

all three algorithms gave good results at high latitudes and the differences are probably due primarily to the details of the implementation and the criteria adopted for source selection.

6.2. SExtractor

SExtractor (Bertin & Arnouts 1996) is a program that is widely used for the automated detection and photometry of sources from astronomical images. It is easy to install and use, and has a number of useful features including the capacity to handle large FITS files in a very quick manner (typically 1 Mpixel/second with a 2 GHz processor), robust deblending of objects for crowded fields, real-time filtering to improve detectability, the ability to detect sources in one image and do the photometry in another (dual image mode), handling of user-supplied weight maps and flag maps, optimum handling of images with variable SNR and flexible catalogue output of desired parameters. In particular, the dual image mode and the handling of images with variable SNR are important for the ERCSC due to the large variance in noise across the sky, both due to the Galactic foregrounds and scan strategy (Figure 1).

6.2.1. Flat Patches

SExtractor, as for other source-detection algorithms considered, requires local flat patches created from gnomonic (tangent plane) projections. 746 flat patches in each band are created from each of the HEALPix formated (Górski et al. 2005) all-sky maps using the *gnomview* procedure provided by the HEALPix IDL library. Flat patches that subtend 10° by 10° on the sky with a 1 degree overlap and that are aligned along Galactic longitude and latitude are produced. The flat patches are 512 by 512 pixels for HFI frequencies, with pixel sizes of 1.17 arcminutes. These pixels are slightly smaller than the 1.7 arcminute sizes of the pixels in the N_{side}=2048 HEALPix representation.

6.2.2. The Method

The SExtractor package works in a series of steps, as shown in Figure 4. The major steps are listed below:

1. Estimate and map the background as well as the rms noise of the image

2. Filter the background-subtracted image to maximize detectability

3. Find objects by isolating connected group of pixels above certain threshold

4. Deblend detections if a saddle point is found in the intensity distribution

5. Clean the spurious detections due to neighboring bright objects

6. Fit for astrometry and perform photometry on each source

6.2.3. Tuning of SExtractor for ERCSC

In the ERCSC pipeline, each map is pre-filtered with a Gaussian kernel the same size as the beam in each frequency. The built-in filtering step within SExtractor is not chosen as it uses a digitalized filtering grid. Typically, a Mexican hat filter gives slightly more reliable detections of point sources in the presence of noise and background, however, bright extended sources are often missed. We choose the Gaussian filter because simulations show that it performed almost as well as the Mexican hat for high latitude compact sources and is still sensitive to sources that are extended.

There are a large number of configuration parameters in SExtractor that can be tuned to improve the performance of the code. We list in Table 7 some of the important parameters and their optimized values in ERCSC. One key parameter is BACK_SIZE, which defines the size of the grid on which the local background is calculated. If it is too small, the background estimation will be affected by the flux of the object. If it is too large, it cannot reflect the small scale variations of the background. Once the initial background map is constructed, a median filter of size BACK_FILTERSIZE is applied to smooth possible local over-estimations

Table 7. Key Configuration Parameters

Parameter Name	Values used in ERCSC	Description
BACK_SIZE	2	Size (in beams) of a background mesh
BACK_FILTERSIZE	3	Size (in background meshes) of the median filter of the background map
WEIGHT_TYPE	BACKGROUND (1st pass) MAP_WEIGHT (2nd pass)	Type of weights to use for detection/photometry
DET_THRESH	5	Detection threshold
DET_MINAREA	0.2	Minimum area (in beams) above threshold
DEBLEND_MINCONT	0.05	Minimum contrast parameter for deblending
DEBLEND_NTHRESH	8	Number of deblending sub-thresholds

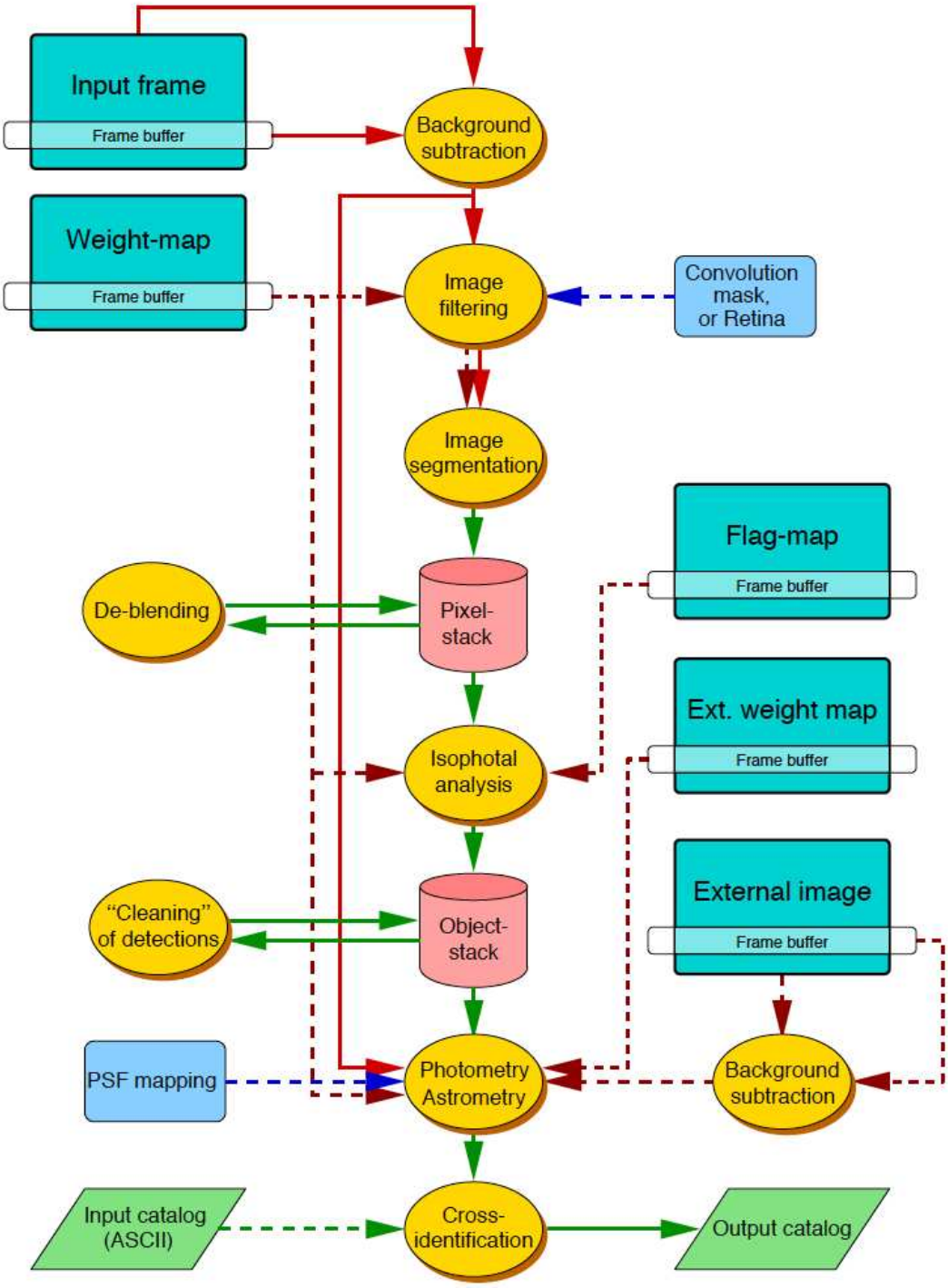

Fig. 4.— Layout of the main SExtractor procedures from the v2.5 user's manual. Dashed arrows represent optional inputs.

due to bright or extended objects.

A 5σ detection threshold is used in the pipeline. The measure of σ used is the photometric noise which is a combination of the sky background noise and the instrumental noise. Confusion noise due to unresolved sources below the detection limit is generally negligible. Upon testing on simulated *Planck* maps, it was noticed that the threshold level cannot be defined using exclusively the covariance map (representing the approximate instrumental noise in each pixel) as it yields far too many detections that are mostly spurious in regions with strong Galactic emission, particularly near the plane. To allow SExtractor to take into account both the instrumental noise and the background fluctuations, we run the code twice in the pipeline. In the first pass, we obtain RMS estimates of the background (i.e. setting WEIGHT_TYPE = BACKGROUND). The background RMS map is then combined with the covariance map to make a weight map, which is supplied to SExtractor in the second pass (i.e. setting WEIGHT_TYPE = MAP_WEIGHT) to derive a variance map. Pixels with noise values greater than the robust 5σ value are given 0 weight in the combination weight map. This step is shown to improve the reliability significantly at low Galactic latitudes.

Due to the scanning strategy of *Planck*, it is inevitable that some pixels will have very few or no hits, resulting in a small number of noisy pixels. These tend to be at low Ecliptic latitudes and at higher *Planck* frequencies. Although DET_MINAREA is used to limit spurious detections from noisy pixels by regulating the minimum number of connected pixels to define an object, such sources often leak into the catalog due to the fact that the data are pre-filtered, which spreads these noisy pixels over a larger region. These sources are further examined and eliminated in the source selection stage (see §7.2).

The performance of SExtractor's own adaptive aperture photometry (MAG_AUTO) is good at high latitudes for all *Planck* frequencies, providing flux densities to within 10% accuracy, and errors that are reasonable (typically 1-5%). Nevertheless, at low Galactic latitudes, particularly at the highest frequencies, the photometry accuracy is significantly degraded. This is because it uses a variable Kron radius which becomes unstable in crowded fields with strong residual background fluctuations. Therefore, an alternate measure of photometry is obtained from an external source extraction code (see §5.2).

Overall, at the highest frequencies, SExtractor appears to identify $> 50\%$ more reliable sources (as measured by the Monte-Carlo technique described later) than the nearest competing technique. Some significant fraction of these sources are potentially associated with Galactic ISM features, and would thereby be extended compared to the *Planck* beam. However, we do consider these as robust astrophysical sources and include them in the catalog, with appropriate flags indicating their extended nature and potential association with cirrus substructure.

7. Quality Assessment Cuts

Quality assessment (QA) is an integral step in the validation of a catalog. It helps quantify flux density biases and flux density uncertainties, positional errors, completeness and reliability in a catalog. In the earlier stages of the pipeline development, QA of the source detection algorithm performance was accomplished by comparison against a truth or input catalog. While this is manageable for simulated maps where the input catalog is known, it is challenging for flight data since observations that are close in time and at a similar frequency need to be undertaken to ensure that both the position and flux density of a source are reliable. The truth catalog QA methodology has been replaced by a Monte-Carlo QA system that incorporates artificial source injection into the *Planck* maps. Primary reasons for this change include the lack of a "truth" catalog when dealing with flight data and the ability of the MCQA system to generate robust statistics across the entire range of source parameters, e.g. flux density. Truth catalog based QA metrics suffer at the brightest flux densities since source numbers are sparse and resultant QA metrics are dominated by the Poisson noise. As a result, the Monte-Carlo QA approach is our primary criterion for selecting high reliability sources.

7.1. The Monte-Carlo QA Approach

The goals of the Monte-Carlo QA system are:

1. To quantify flux density biases and flux density uncertainties as a function of background.
2. To quantify completeness in extracted sources as a function of flux density.
3. To quantify contamination or "spurious sources" as a function of flux density.
4. To assess positional offsets between extracted and input sources.
5. To assess systematics associated with beam shape, gaps in coverage, scan strategy etc.

Although some might argue that the Monte-Carlo system is an incomplete measure of spurious sources, it is the only one which can systematically be applied at all frequencies. Adopting a validation technique that is based on source extraction techniques run on imprecise simulations of the entire sky (such as the FFP simulations) could yield different results and are currently a work in progress. This is the primary reason why postage stamps for source visualization, validation with other ancillary catalogs and other characteristics of the

detected sources are provided in the ERCSC catalog, so the user can assess the robustness of the *Planck* sources for themselves.

7.1.1. Technique

The first step of a MC QA run is to run the ERCSC pipeline on the input maps to generate a source catalog for the true sky. We then inject unresolved point sources whose full-width at half maximum is identical to the derived effective beam, into the maps and re-run the main ERCSC pipeline. The typical run parameters are ∼1000 sources per iteration, uniformly distributed across the sky. In order to minimize sqrt(N) statistics in our estimates of QA parameters while keeping confusion low, we execute 10 iterations. The present set of runs use a flat dN/dlogS distribution at all flux densities ranging from 100 mJy to 100 Jy. We have previously tested Monte-Carlo runs where the injected sources follow a flux density distribution that is similar to the *Planck* Sky Model. We find no significant issue associated with the choice of flux density distribution particularly because source extraction in the *Planck* maps are not significantly affected by source confusion.

At the end of the Monte-Carlo runs, we have one catalog which only comprises the sources detected in the original map and 10 catalogs which have the original sources in addition to the detected fraction of the fake sources that were injected into the maps. We first match the sources in the original map to each of the remaining 10 catalogs with a matching threshold of 2×FWHM. This leaves only the artificial sources in the catalogs, whose properties can then be compared to the known flux densities and positions of the injected sources.

Completeness is quantified as the fraction of input sources which have extracted flux densities to within 30%, while reliability specifies the fraction of extracted sources that differ from their input flux densities to within 30%. Both completeness and reliability are measured as a function of signal-to-background RMS where the background RMS is measured in a 2° radius annulus as described below.

7.1.2. Background Thresholding

Since the ERCSC is an all sky catalog, QA parameters need to be measured as a function of position due to significant substructure in the background. For example, source position uncertainties and flux density errors in the Galactic plane are higher than at high Galactic latitudes. The simplest proxy for position is Galactic latitude. However, at the higher HFI

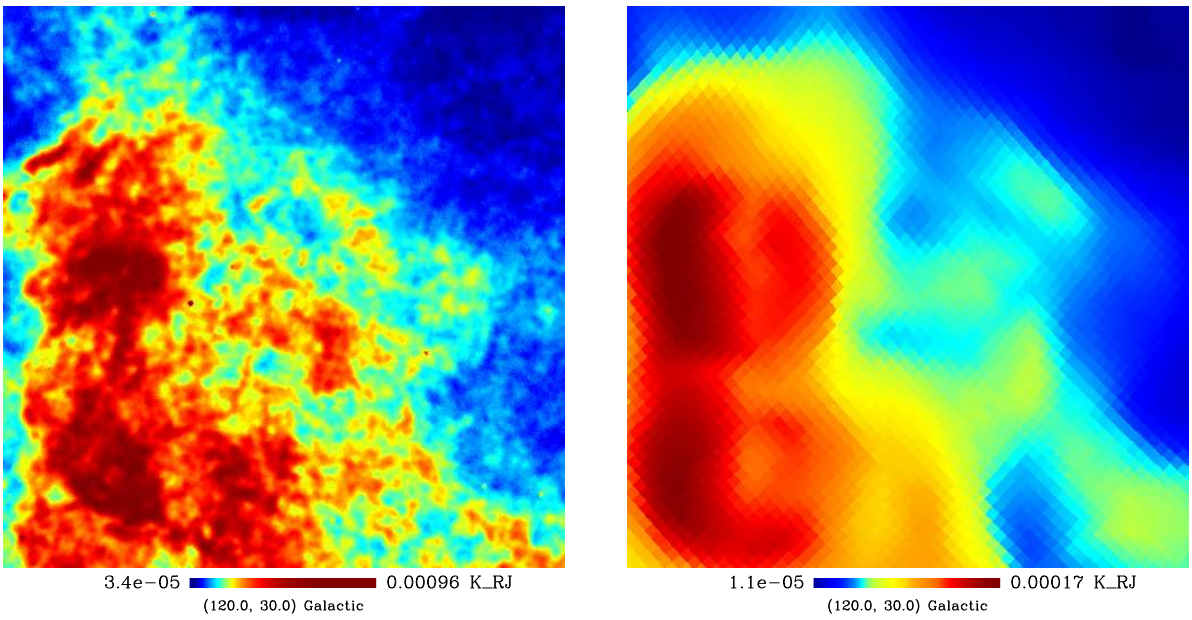

Fig. 5.— Example of a threshold map at 857 GHz, in a region dominated by Galactic ISM emission. *Left:* Original intensity map. *Right:* Background threshold map estimated by measuring the RMS in a 2° annulus around each pixel. The background threshold map is converted to a 1σ point source flux uncertainty before it is used in the SNR calculation. The threshold map appears to be spatially offset from the intensity map. This is because the RMS increases along edges of structures due to the fact that the annulus includes pixels with a wider range of intensities i.e. regions of high intensity dont necessarily correspond to regions of high RMS.

frequencies a simple Galactic latitude cut is a poor proxy for structure in the background due to significant ISM structure even at high Galactic latitudes. As a result, it was decided to measure the RMS in the background at each Healpix pixel by taking a map with all detected source subtracted, centering an annulus at each pixel with inner radius and outer radius being 0.5×FWHM and 2° respectively and measuring the RMS in that annulus. The choice of 2° was made empirically. We found that if the outer radius were too small i.e. 10s of arcminutes, the RMS was similar to the RMS returned by the detection codes which identify sources as peaks above the local background RMS. These RMS returned by the codes are typically lower than the RMS measured in the larger annulus used here. If the outer radius were too large (several degrees), background structure gets smoothed out. 2° represents a trade-off between these two extremes and yields a background RMS which is a combination of substructure in the background and the instrumental noise in the maps. Figure 5 shows an example threshold map generated at 857 GHz.

We have verified that using such a background threshold is a reasonable estimate of the RMS by demonstrating that the reliability vs signal-to-background RMS ratio plots are similar both at low and high Galactic latitudes while if the background RMS were a poor representation of the substructure in the background, these relationships would be different as a function of Galactic latitude.

7.1.3. Flux Accuracy

The overall catalog has been characterized such that >90% of the sources have a flux density accuracy of within 30%. The 30% requirement for the flux density accuracy imposed for both the completeness and reliability criteria implies a flux density range of almost a factor of 2 i.e. 0.7×flux to 1.3×flux. We believe for the catalog to be scientifically useful, flux densities need to be accurate within that range. Imposing the requirement implies that the catalog is equivalent to a catalog with a $>5\sigma$ cut if the noise were Gaussian. That is, a typical 5σ source would have a flux density error that is smaller than 20%, 68% of the time, which translates to a flux density error of <30% for 90% of the sources, for a Gaussian distribution of errors. It is well known that the contribution from the Galaxy and the CMB results in a non-Gaussian distribution for the background RMS, at least on large spatial scales. Future work will attempt to build upon our increased knowledge of the foregrounds from the *Planck* maps and undertake a more precise characterization of the noise, to identify sources with greater reliability.

7.1.4. Performance of Codes

The ERCSC pipeline involves running four source detection codes mentioned earlier. The versions of the codes were limited to those which were available prior to June 1, 2010. Thus, we used v2.0 of PowellSnakes, the "non-blind" runs of IFCAMex and the Feb 2009 version of PMF. The version and parameters of SExtractor have been described in an earlier chapter.

Figure 6 shows the relative performance of the codes over the entire sky as derived from the Monte-Carlo analysis. The first plot shows the distribution of injected vs extracted flux densities for the Monte-Carlo sources as a function of SNR where SNR is the extracted flux density divided by the background RMS. The RMS is the value of the threshold map at the location of the source. Only the lowest SNR are shown in the plots since that is the regime in which differences between the codes begin to appear. We note that for these plots, aperture photometry was used as the primary measure of extracted flux density for all techniques. The colored point show the median and standard deviation of the underlying points.

The second panel shows the differential reliability of extracted sources as a function of SNR while the third panel shows the differential completeness of injected sources as a function of SNR. Differential values are more illustrative than cumulative values since they clarify the signal to noise limit where the performance of an algorithm starts to degenerate. Cumulative reliability and completeness estimates integrate the differential reliability and completeness up to the highest signal to noise ratio and are therefore an average over a range of SNR values. The remarkable feature of the plots is the similarity between the different techniques even at low SNR regimes although PMF does perform markedly worse at many frequencies.

The results that are shown for the Monte-Carlo sources are translated into a measure of reliability and completeness for each of the sources that are present in the original map. The signal to noise of each original source can be estimated by dividing the aperture flux density of the source by its corresponding background RMS from the threshold map. The properties of the Monte-Carlo sources that are shown in the plots can then be associated to the original sources, by simply interpolating the reliability vs SNR curves that are plotted to the SNR of the source. Thus, the primary quantifier for estimating the completeness, reliability, flux density uncertainties and flux density biases of the original sources is the SNR of the source.

For the ERCSC pipeline, the reliability estimated described above are derived for both the aperture flux density and the native algorithm derived flux density (FLUXDET). The larger of the two measures of reliability are passed on since it implies that one of the two flux density measures are more appropriate for compact sources at the corresponding SNR.

Once we have estimated the reliability of each source in the original map, we sort the sources in decreasing order of SNR and apply a cut at the lowest SNR such that the cumulative reliability of the cut sources is greater than 90%. This is the primary criterion used to select high reliability sources. The technique that is chosen at each frequency is the one that returns the maximum number of $|b| > 30^\circ$ sources above a cumulative reliability of 90%. These happen to be PowellSnakes from $30 - 143$ GHz and SExtractor from $217 - 857$ GHz. Additional steps that validate the usage of this technique and validate the sources in the catalogs are discussed in forthcoming sections.

7.1.5. Positional Accuracy and Flux Density Limit

Based on the algorithm selection criteria outlined in the previous section, we next show the flux accuracy, the positional accuracy and the differential completeness and reliability as a function of flux density for each frequency based on the Monte-Carlo analysis (Figure 7). PowellSnakes performance is shown at 5 frequencies (30, 44, 70, 100, 143) and SExtractor at the remaining 4 frequencies (217, 353, 545, 857 GHz). The plots are generated only for the half of the sky corresponding to the lowest background and are therefore our best estimate of the limiting flux density in the maps at each of the frequencies.

The top left panel shows the fractional error between the injected and extracted fluxes for the artificial injected sources for the low background regions. The red points and uncertainties represent the median and standard deviation of the points in that bin. At almost all frequencies, at the bright end, the median is centered around zero while the standard deviation increases as one moves towards faint flux densities, exactly as one would expect due to the increasing contribution of background noise.

The second plot and third plot show the distribution of spatial offsets between the injected and extracted sources, along with the median and standard deviation of the separation. The last plot shows the differential completeness and contamination in the lowest background regions of sky. As explained earlier, the completeness is the fraction of injected sources at a particular flux density that are extracted with a flux density within 30% of the injected flux density. The contamination is the fraction of extracted sources at a particular flux density that are injected with a flux density that is larger than 30% of the extracted flux density. Thus, the sum of completeness and contamination need not add up to 100%. Contamination can also be defined as $(1-\text{reliability})\times 100$.

The translation from S/N ratio shown in the abcissa of Figure 6 to flux density as shown in the abcissa of Figure 7 is not straightforward since it depends on the the local RMS. To do

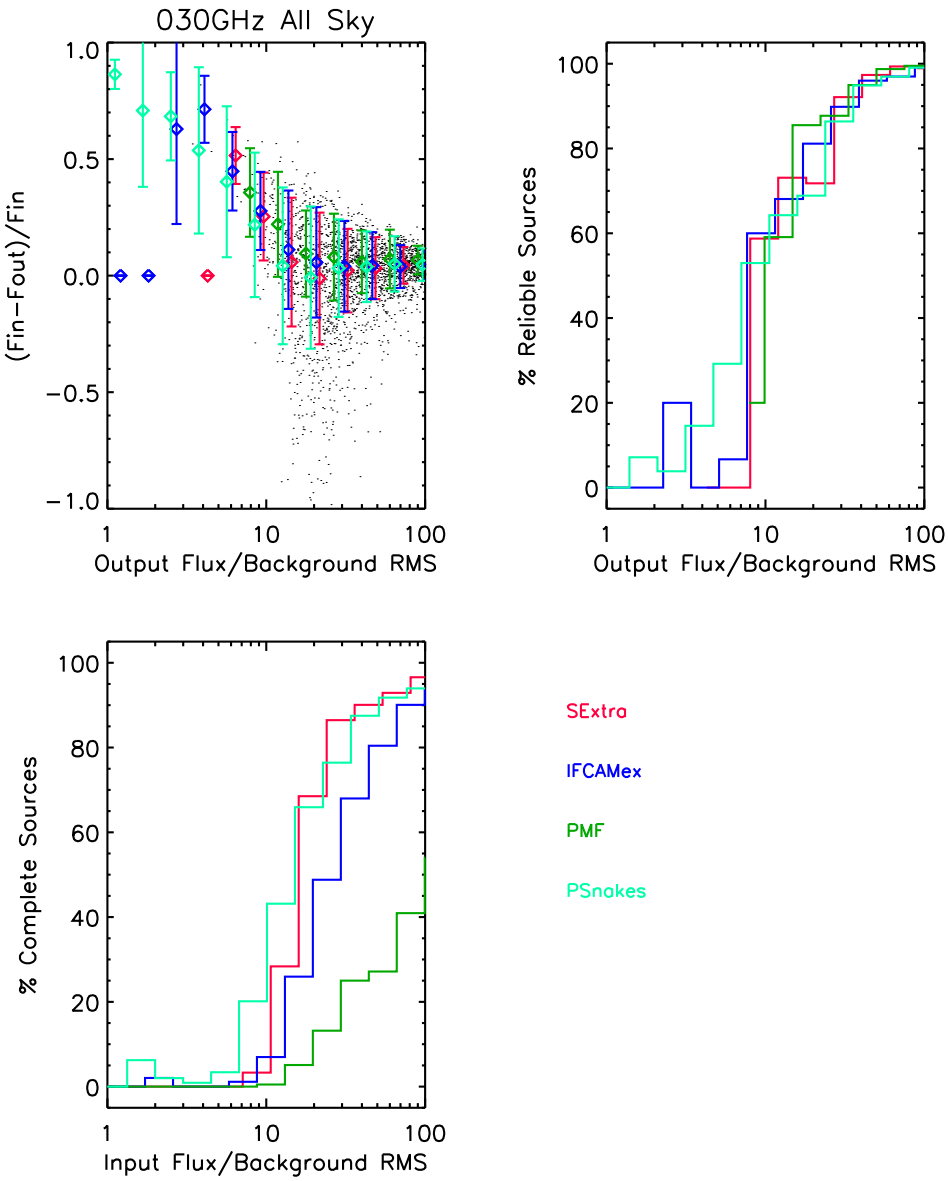

Fig. 6.— Plots showing the flux uncertainty, differential reliability and differential completeness of the Monte-Carlo sources for the different codes in the low SNR regime where differences between the codes are the most vivid. Each page shows the plots at a different frequency. The most striking aspects of these plots are the similarity between the performances of IFCAMex, PowellSnakes and SExtractor despite using completely different algorithms. The current version of PMF appears to show worse performance at many frequencies. The catalog that is chosen at each frequency is the one that returns the maximum number of sources above a cumulative 90% reliability cut.

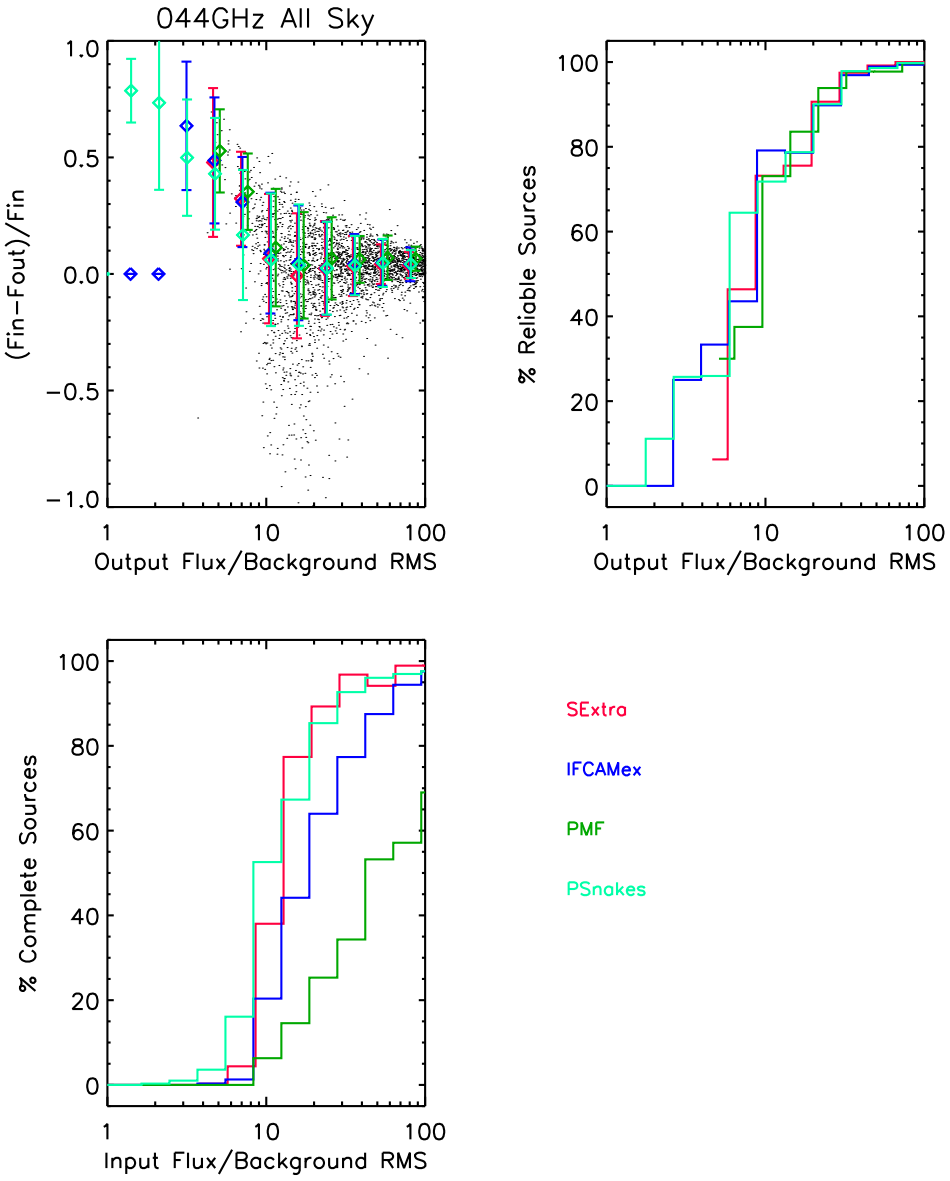
044GHz All Sky
(Fin−Fout)/Fin
1.0
0.5
0.0
−0.5
−1.0
1
10
100
Output Flux/Background RMS
% Reliable Sources
100
80
60
40
20
0
1
10
100
Output Flux/Background RMS
% Complete Sources
100
80
60
40
20
0
1
10
100
Input Flux/Background RMS
SExtra
IFCAMex
PMF
PSnakes

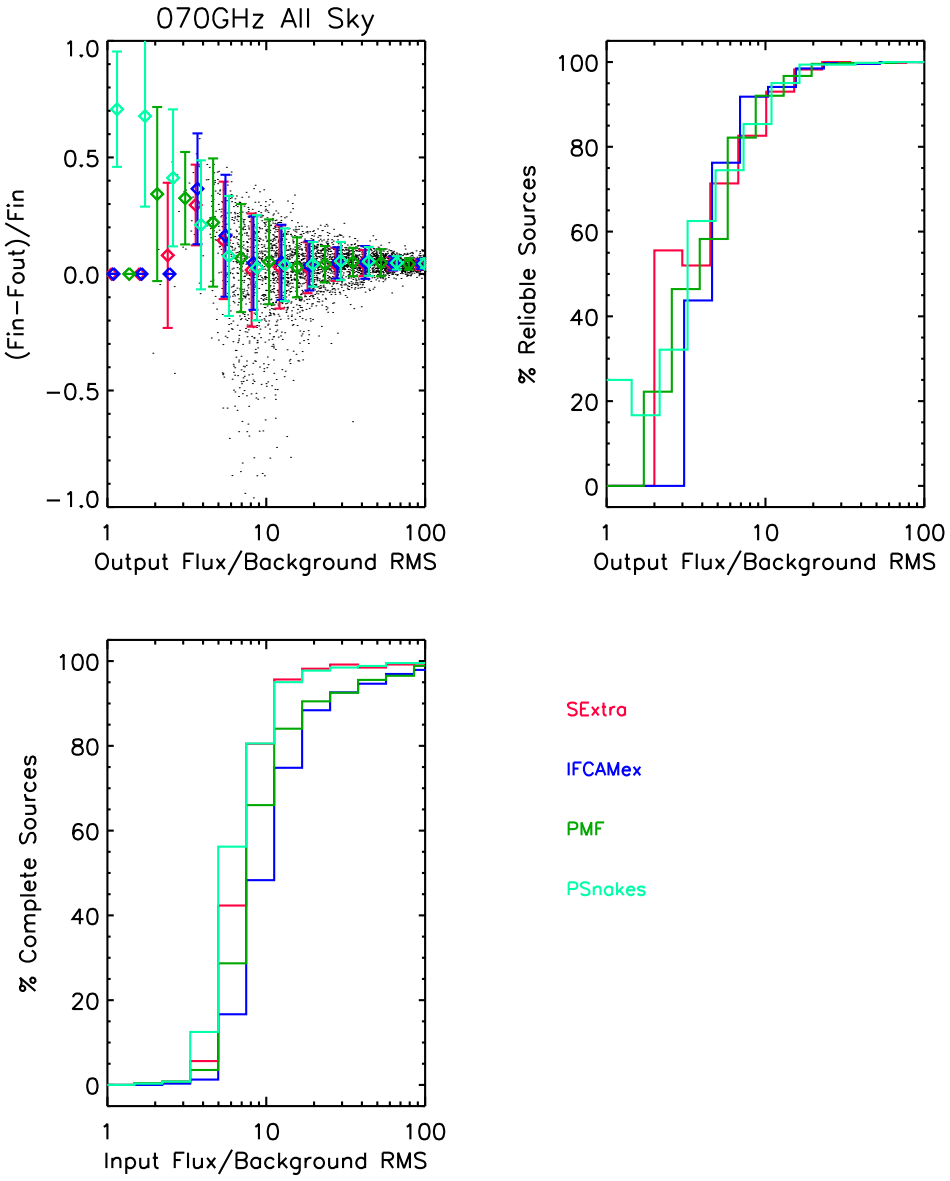
070GHz All Sky
(Fin−Fout)/Fin
1.0
0.5
0.0
−0.5
−1.0
1
10
100
Output Flux/Background RMS
% Reliable Sources
100
80
60
40
20
0
1
10
100
Output Flux/Background RMS
% Complete Sources
100
80
60
40
20
0
1
10
100
Input Flux/Background RMS
SExtra
IFCAMex
PMF
PSnakes

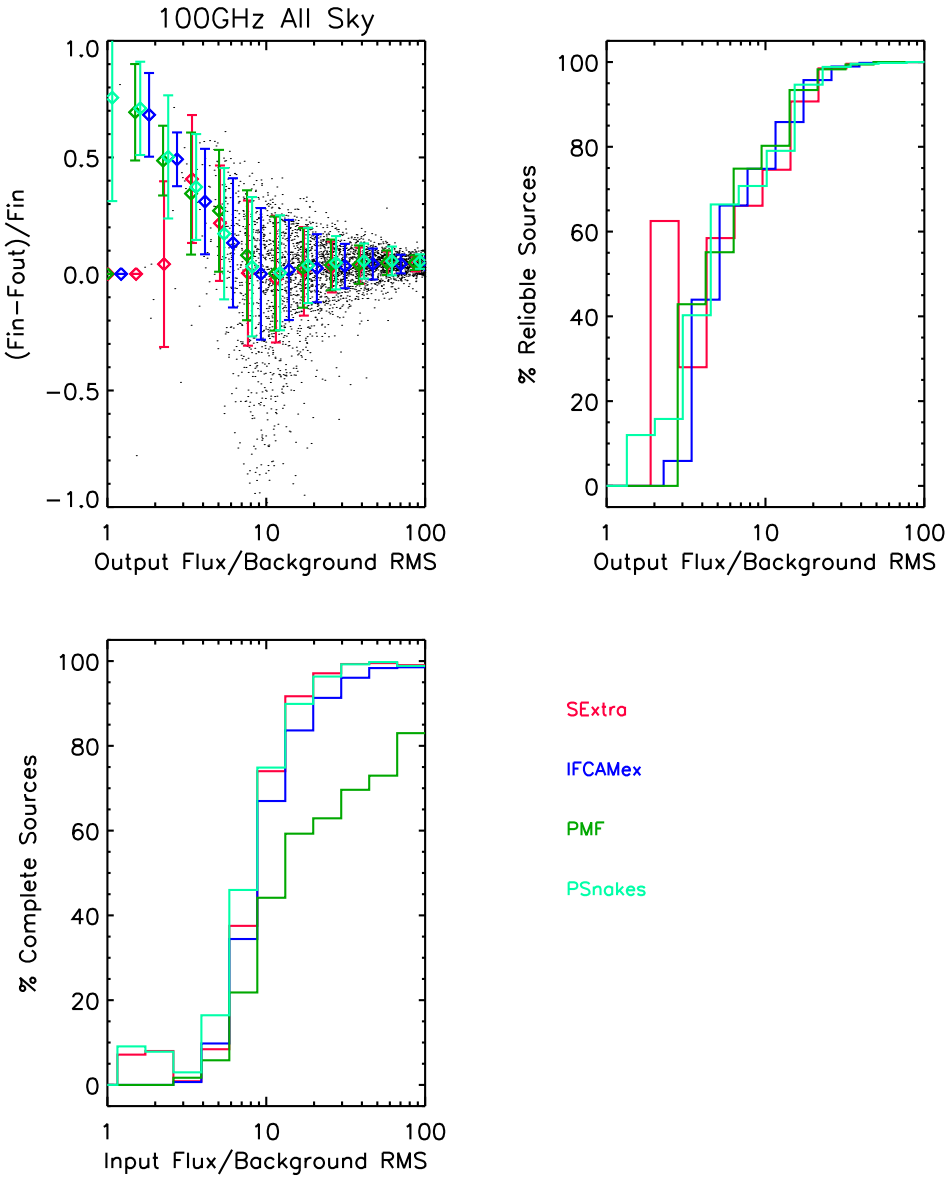
100GHz All Sky
(Fin−Fout)/Fin
1.0
0.5
0.0
−0.5
−1.0
1
10
100
Output Flux/Background RMS
% Reliable Sources
100
80
60
40
20
0
1
10
100
Output Flux/Background RMS
% Complete Sources
100
80
60
40
20
0
1
10
100
Input Flux/Background RMS
SExtra
IFCAMex
PMF
PSnakes

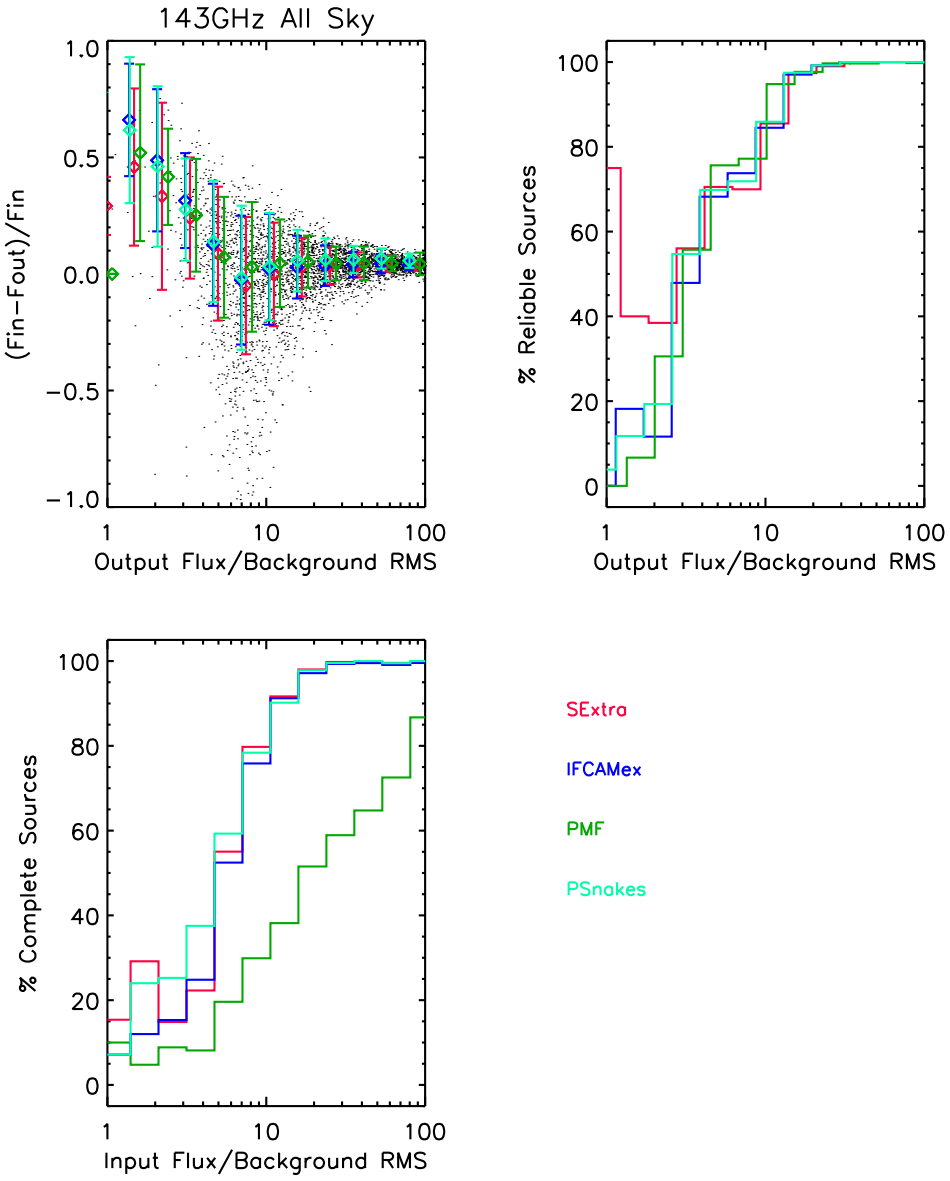
143GHz All Sky
(Fin−Fout)/Fin
1.0
0.5
0.0
−0.5
−1.0
1
10
100
Output Flux/Background RMS
% Reliable Sources
100
80
60
40
20
0
1
10
100
Output Flux/Background RMS
% Complete Sources
100
80
60
40
20
0
1
10
100
Input Flux/Background RMS
SExtra
IFCAMex
PMF
PSnakes

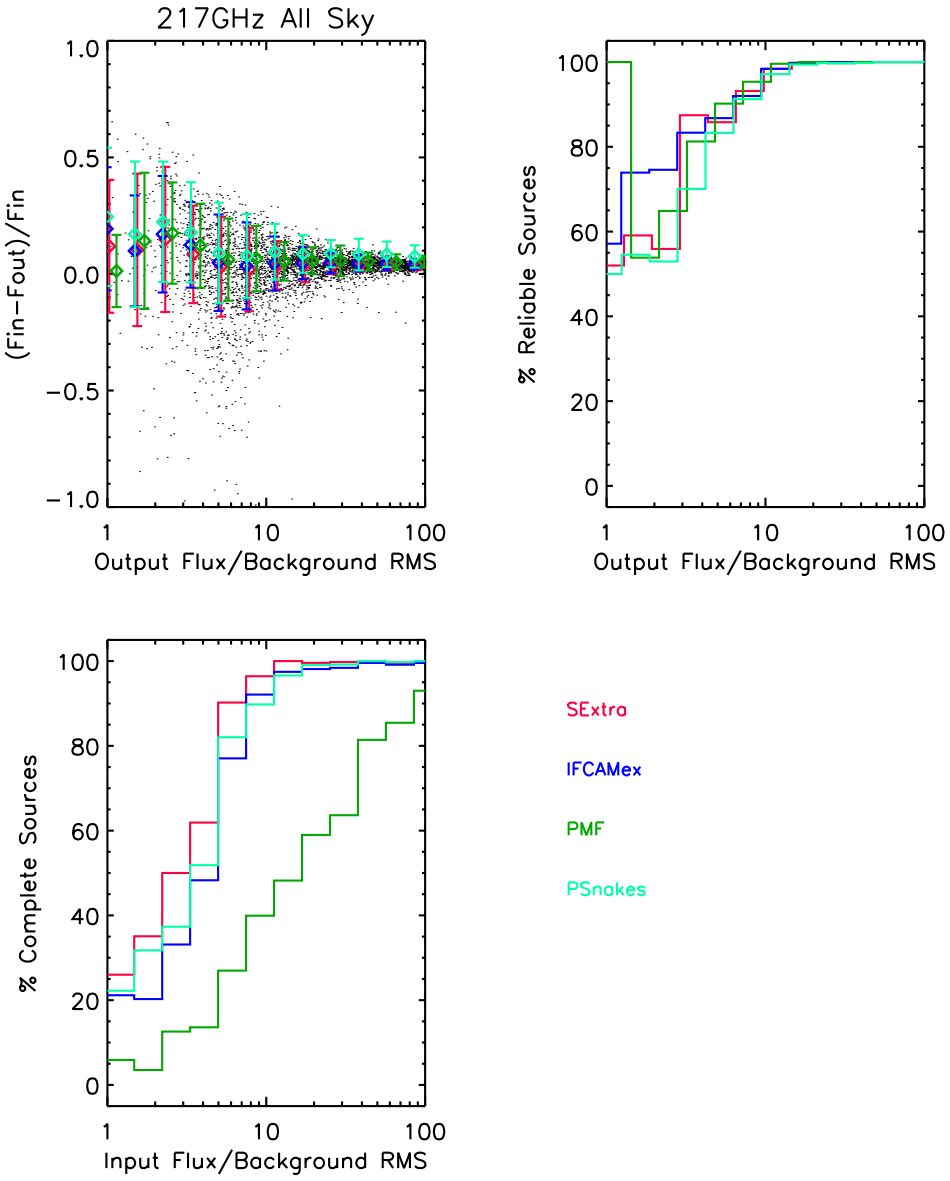
217GHz All Sky
(Fin−Fout)/Fin
1.0
0.5
0.0
−0.5
−1.0
1
10
100
Output Flux/Background RMS
% Reliable Sources
100
80
60
40
20
0
1
10
100
Output Flux/Background RMS
% Complete Sources
100
80
60
40
20
0
1
10
100
Input Flux/Background RMS
SExtra
IFCAMex
PMF
PSnakes

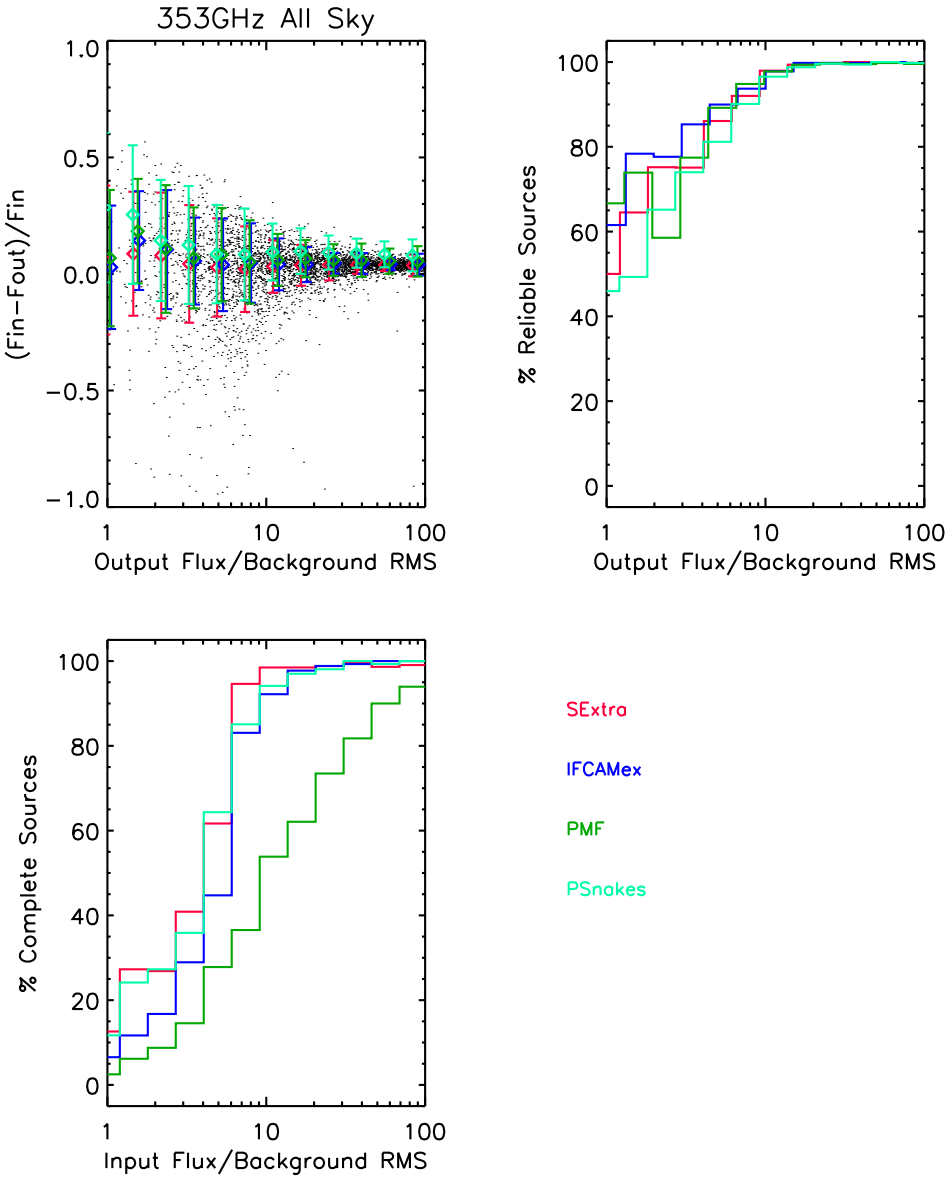
353GHz All Sky
(Fin−Fout)/Fin
1.0
0.5
0.0
−0.5
−1.0
1
10
100
Output Flux/Background RMS
% Reliable Sources
100
80
60
40
20
0
1
10
100
Output Flux/Background RMS
% Complete Sources
100
80
60
40
20
0
1
10
100
Input Flux/Background RMS
SExtra
IFCAMex
PMF
PSnakes

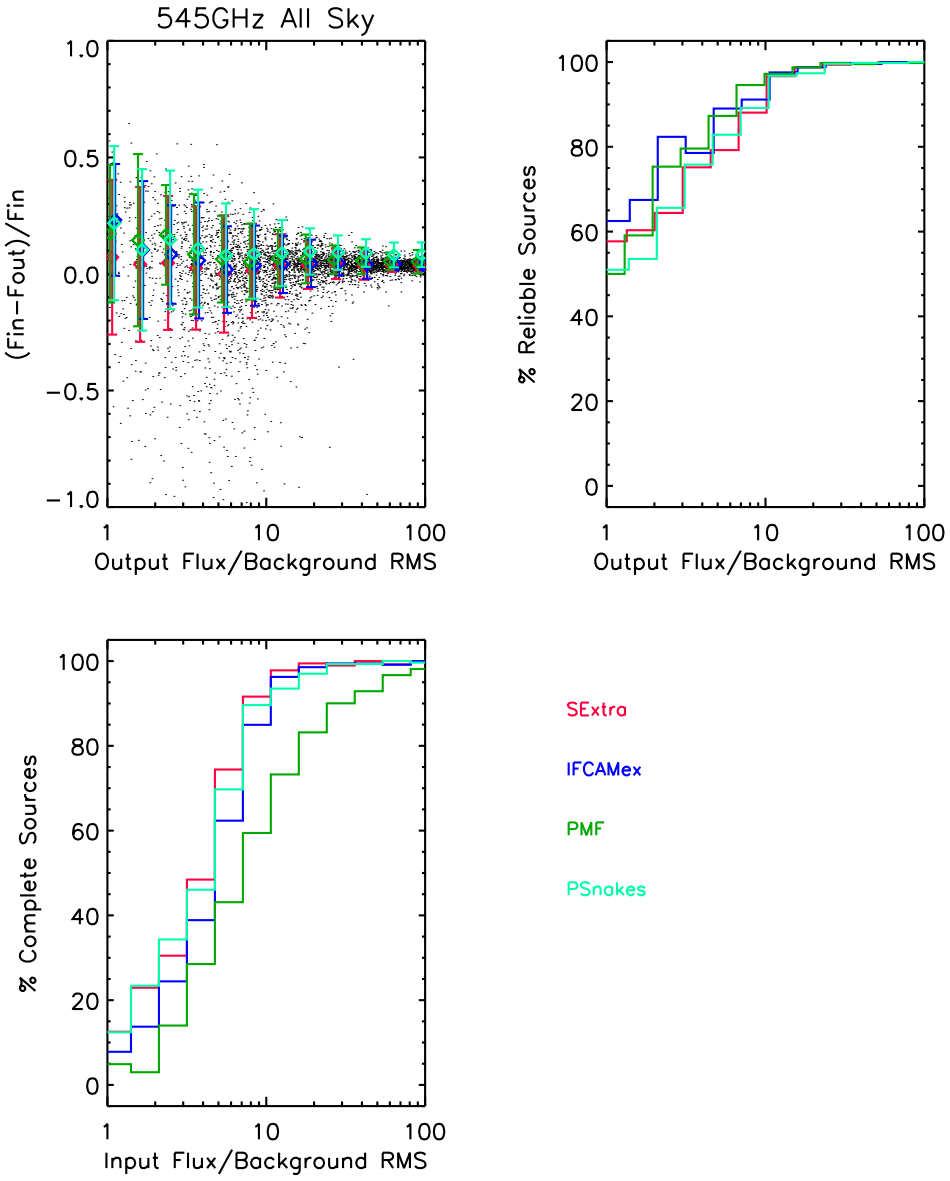
545GHz All Sky
(Fin−Fout)/Fin
1.0
0.5
0.0
−0.5
−1.0
1
10
100
Output Flux/Background RMS
% Reliable Sources
100
80
60
40
20
0
1
10
100
Output Flux/Background RMS
% Complete Sources
100
80
60
40
20
0
1
10
100
Input Flux/Background RMS
SExtra
IFCAMex
PMF
PSnakes

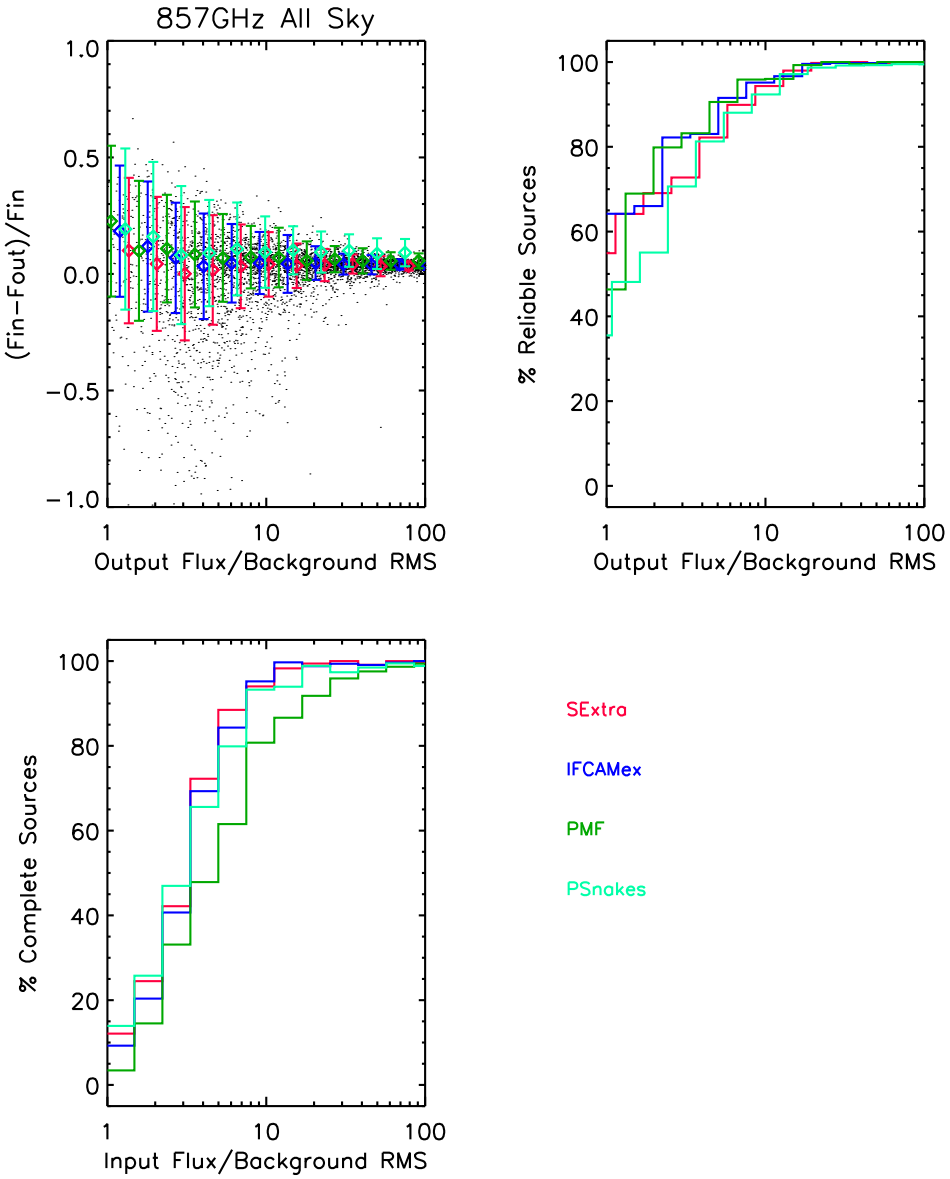
857GHz All Sky
(Fin−Fout)/Fin
1.0
0.5
0.0
−0.5
−1.0
1
10
100
Output Flux/Background RMS
% Reliable Sources
100
80
60
40
20
0
1
10
100
Output Flux/Background RMS
% Complete Sources
100
80
60
40
20
0
1
10
100
Input Flux/Background RMS
SExtra
IFCAMex
PMF
PSnakes

this translation, we construct a two-dimensional matrix $P(i, j)$ where i is bins of input flux density and j is bins of output flux density (Chary et al. 2004). The elements of the matrix are the number of sources of a particular input flux extracted with a particular output flux. At the brightest flux densities, this is typically a diagonal matrix since all input sources have extracted flux densities very similar to the output flux density. As one goes towards fainter flux densities, the uncertainties in the extracted flux increase such that $P(i, *)$ is a gaussian distribution centered on $j = i$. The completeness is a sum of the elements of the matrix $P(i, *)$ where the flux density error is less than 30%, divided by the total number of injected sources in that flux bin. This number is multiplied by 100 to convert to a percentage. The contamination at a flux density j is the sum of all $P(*, j)$ where the difference between the extracted and injected flux density is >30% i.e. if an extracted source has an input flux density which is outside its extracted flux density bin, it is a contaminant. It is converted to a percentage by dividing by the sum of all $P(*, j)$ and multiplying by 100.

To summarize, the Monte-Carlo technique is our primary metric for selecting high reliability sources from the raw catalog. The result of the Monte-Carlo QA technique was a relationship between the SNR, defined as the ratio of the aperture flux to the local threshold map value, and the (differential) reliability. The differential reliability was converted to a cumulative reliability by integrating the differential reliability in decreasing order of SNR. We imposed a cumulative reliability threshold of 90% and a maximum standard deviation in the reliability of 10% for sources with this SNR as inferred from Poisson statistics. After selecting the sources that meet these criteria, we have an initial list of high reliability sources.

7.2. Secondary Quality Assessment Cuts

After selecting high reliability source from the Monte-Carlo analysis, a set of additional secondary cuts which take into account known source artifacts are applied. First, the transit of bright sources, especially planets, across the beam, results in a pattern of bright and dark patches that is repeated every $36'$ along the scan pattern, at the upper HFI bands. They are due to the imprecise removal of an instrumental artifact (the 4K cooler line). A subset of these patterns have been visually identified in the maps and masks have been generated for those patches of sky. These masks are reflected in the incomplete sky coverage in Table 1. If more than 5% of the pixels within a radius of a FWHM from the source fall on the mask, the source is rejected. Even among rings which havent been masked, we visually inspect the sources at 545 and 857 GHz and eliminate those that appear to overlap with this bright and dark pattern.

In addition, there are known gaps in the maps associated with the masking of planets

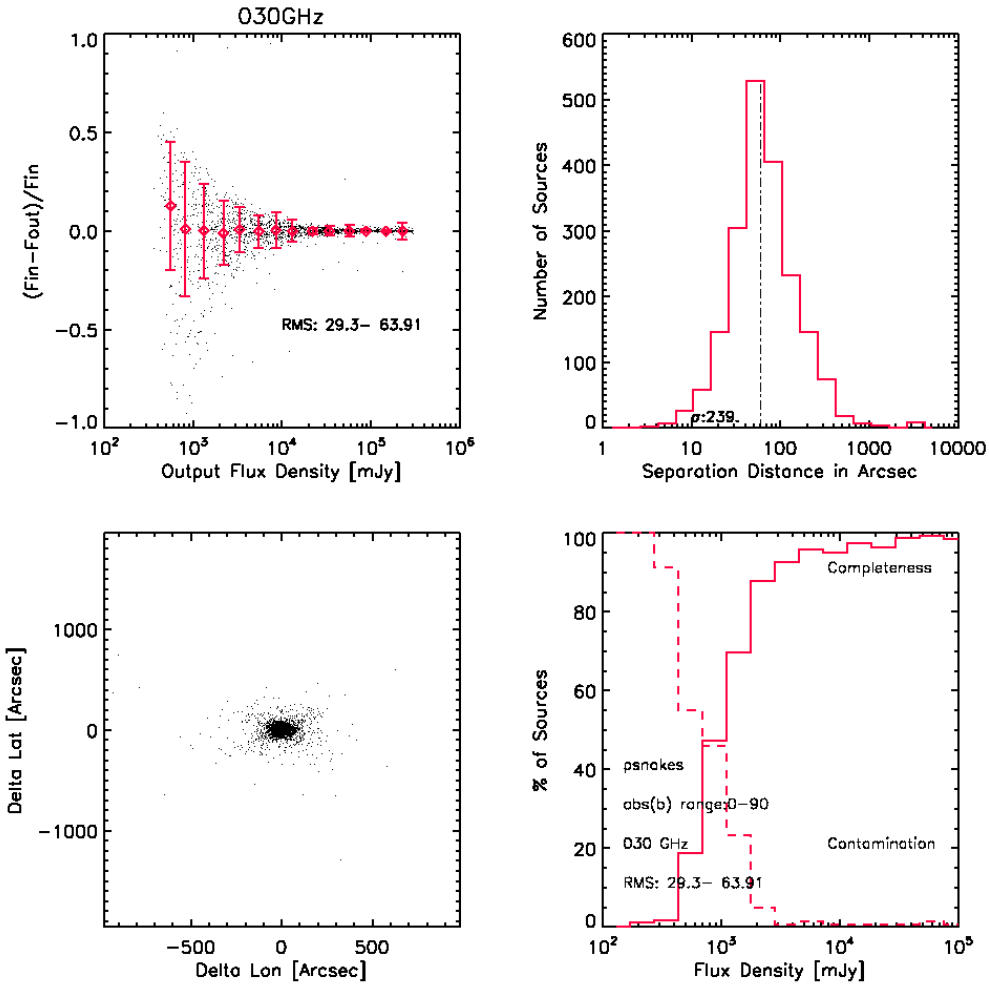

Fig. 7.— Plots showing the flux density accuracy (top left), positional accuracy (top right) and positional difference (bottom left). The bottom right shows the differential completeness and contamination as a function of flux density (See text for details). PowellSnakes is shown for 5 frequencies (30, 44, 70, 100, 143) while SExtractor is shown for 4 frequencies (217, 353, 545 and 857 GHz). The plots are for the lowest background regions (1σ background RMS for a point source shown as an inset in the top left panel in mJy) and are therefore our best estimate of the limiting flux density in the deepest parts of the maps. For example, the 90% differential completeness at 30 GHz is almost ∼3 Jy while at 857 GHz it is 2 Jy, in low background regions of sky. Similarly, by examining the differential contamination plot, it is possible to infer that at 2 Jy at 30 GHz, about 5% of sources have flux density errors >30%. At 857 GHz, at 3 Jy, almost 8% of sources have flux density errors >30%. Naturally, close to the Galactic Plane the sensitivity is markedly poorer due to the contribution from the Galaxy.

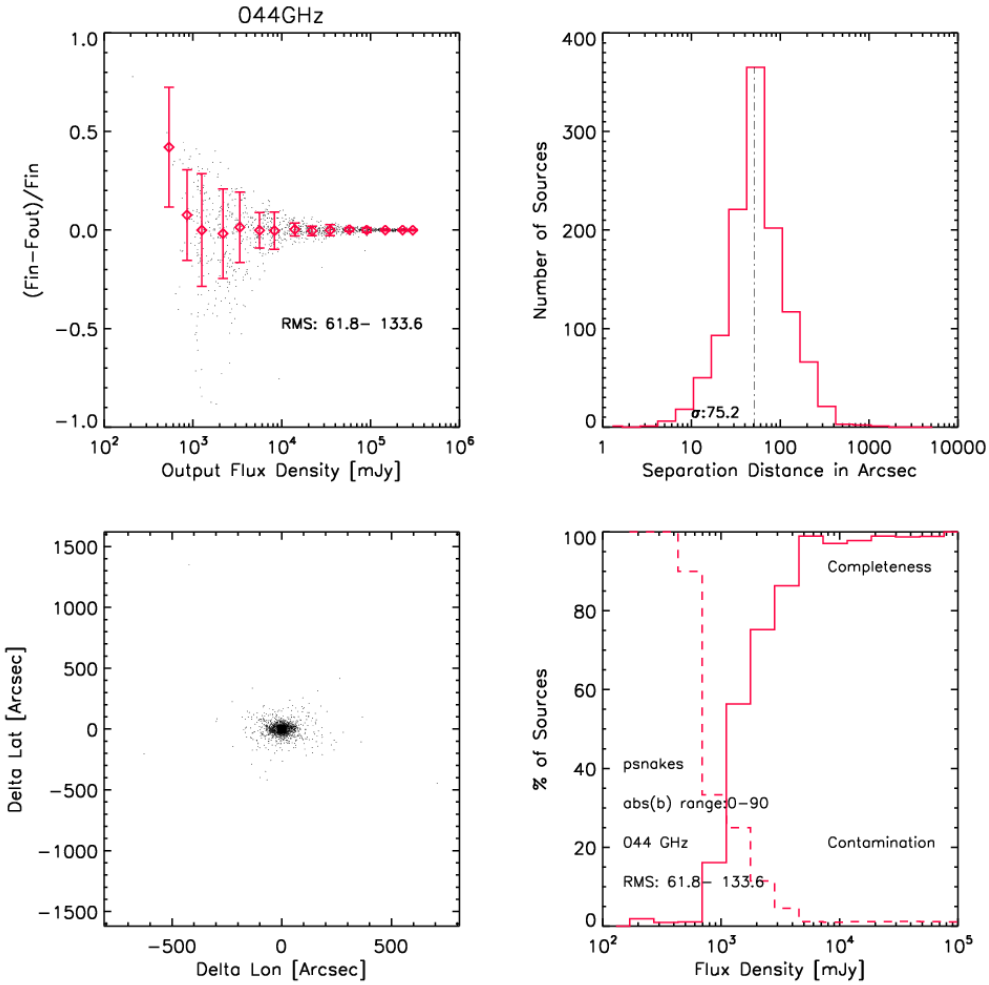
044GHz
(Fin−Fout)/Fin
Output Flux Density [mJy]
RMS: 61.8− 133.6
Number of Sources
Separation Distance in Arcsec
σ:75.2
Delta Lat [Arcsec]
Delta Lon [Arcsec]
% of Sources
Completeness
Contamination
psnakes
abs(b) range:0−90
044 GHz
RMS: 61.8− 133.6
Flux Density [mJy]

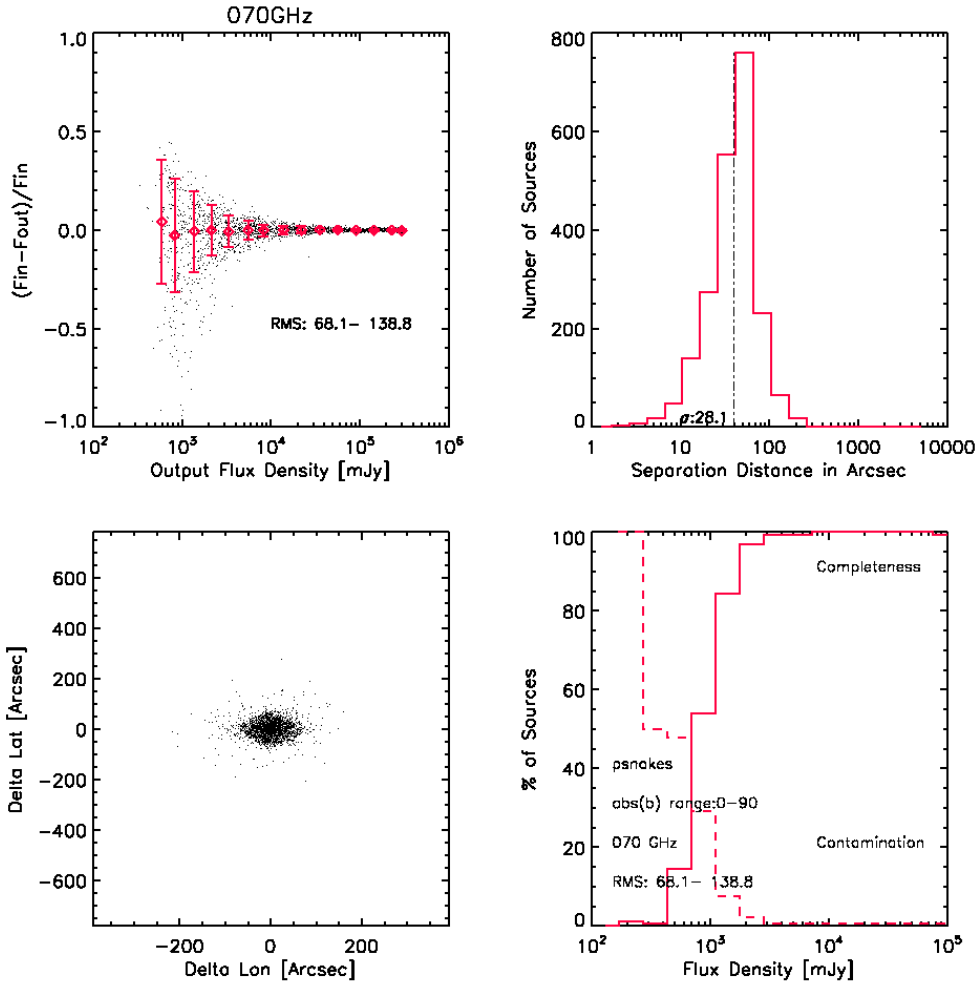
070GHz
(Fin−Fout)/Fin
Output Flux Density [mJy]
RMS: 68.1− 138.8
Number of Sources
σ:28.1
Separation Distance in Arcsec
Delta Lat [Arcsec]
Delta Lon [Arcsec]
% of Sources
Completeness
psnakes
abs(b) range:0−90
070 GHz
Contamination
RMS: 68.1− 138.8
Flux Density [mJy]

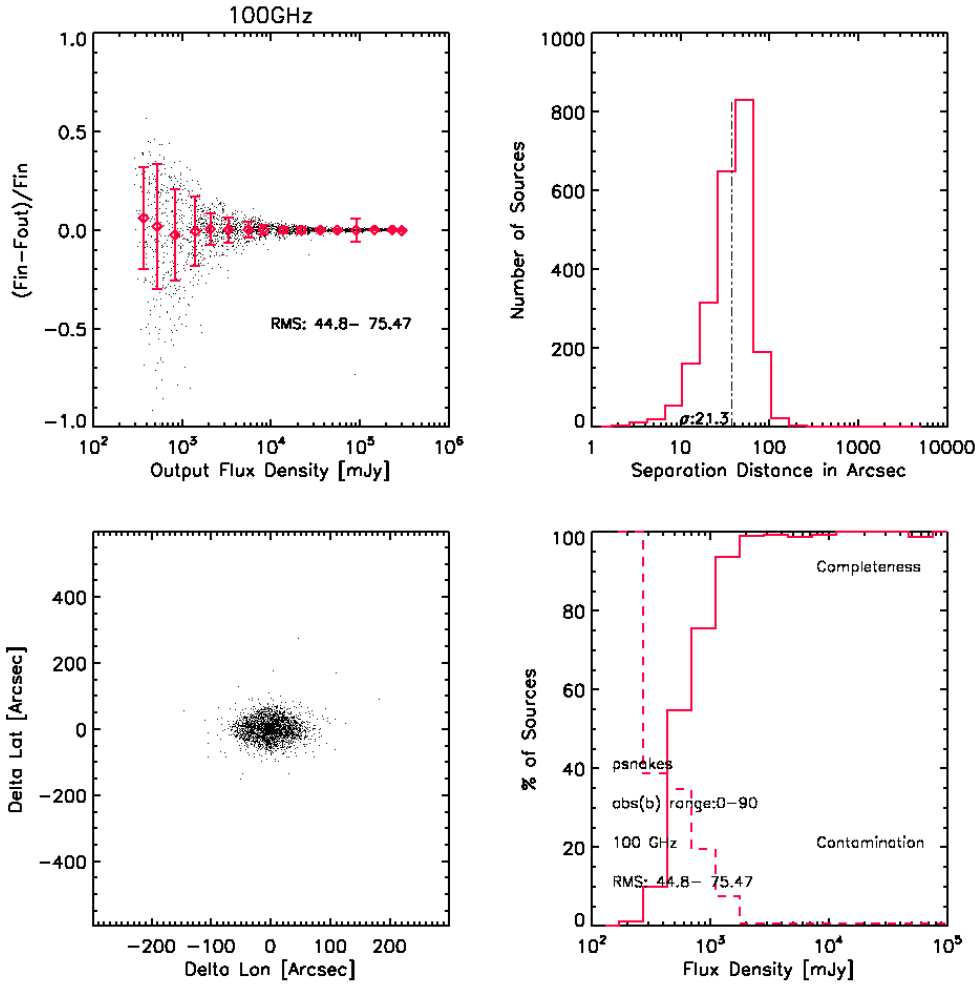
100GHz
(Fin−Fout)/Fin
Output Flux Density [mJy]
RMS: 44.8− 75.47
Number of Sources
Separation Distance in Arcsec
σ:21.3
Delta Lat [Arcsec]
Delta Lon [Arcsec]
% of Sources
Completeness
Contamination
psnakes
abs(b) range:0−90
100 GHz
RMS: 44.8− 75.47
Flux Density [mJy]

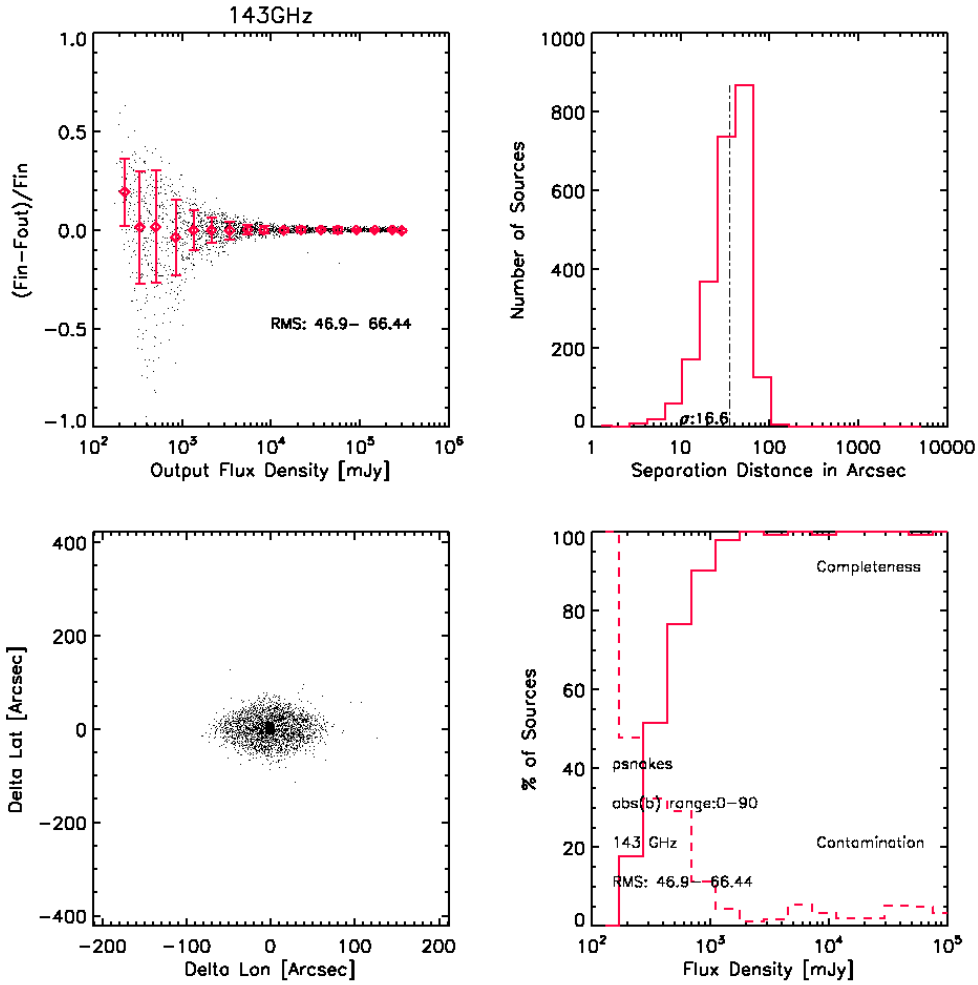
143GHz
(Fin−Fout)/Fin
Output Flux Density [mJy]
RMS: 46.9− 66.44
Number of Sources
Separation Distance in Arcsec
σ:16.6
Delta Lat [Arcsec]
Delta Lon [Arcsec]
% of Sources
Flux Density [mJy]
Completeness
Contamination
psnakes
abs(b) range:0−90
143 GHz
RMS: 46.9 −66.44

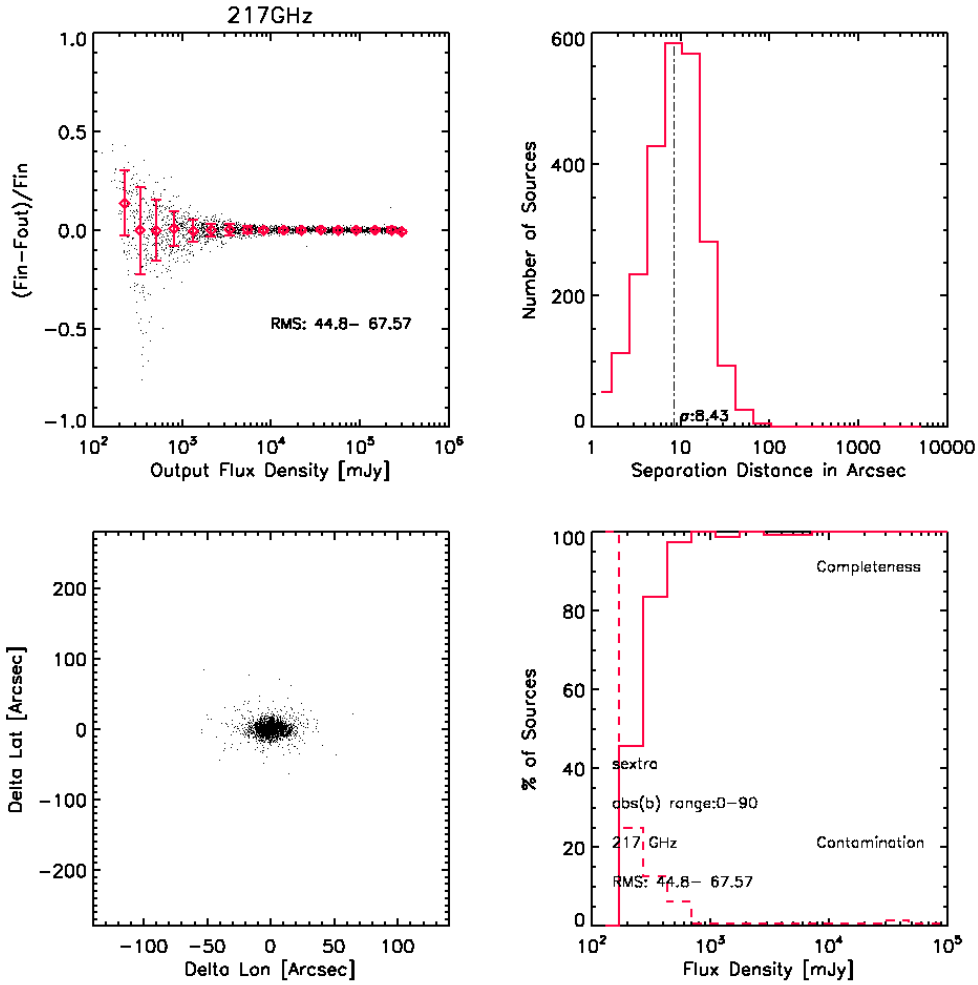
217GHz
(Fin−Fout)/Fin
Output Flux Density [mJy]
RMS: 44.8− 67.57
Number of Sources
ρ:8.43
Separation Distance in Arcsec
Delta Lat [Arcsec]
Delta Lon [Arcsec]
% of Sources
Completeness
sextra
abs(b) range:0−90
217 GHz
Contamination
RMS: 44.8− 67.57
Flux Density [mJy]

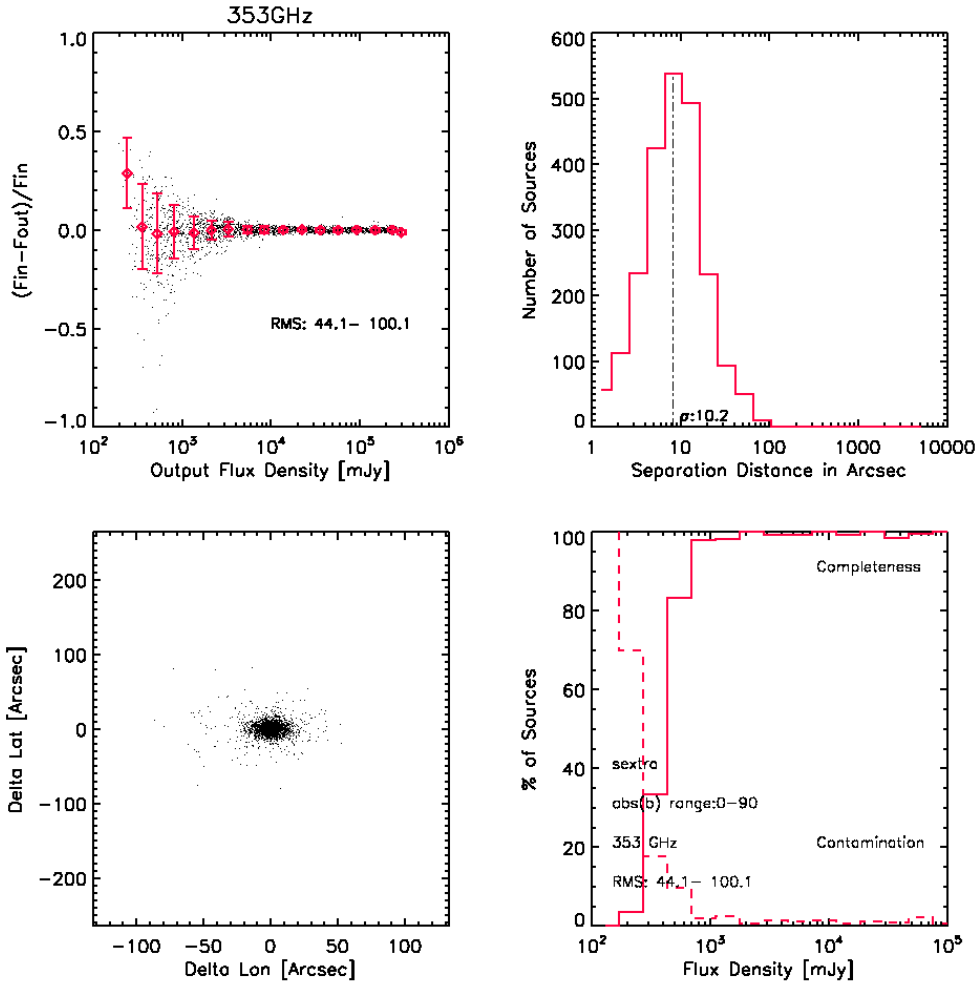
353GHz
(Fin−Fout)/Fin
Output Flux Density [mJy]
RMS: 44.1− 100.1
Number of Sources
Separation Distance in Arcsec
ρ:10.2
Delta Lat [Arcsec]
Delta Lon [Arcsec]
% of Sources
Completeness
Contamination
sextra
abs(b) range:0−90
353 GHz
RMS: 44.1− 100.1
Flux Density [mJy]

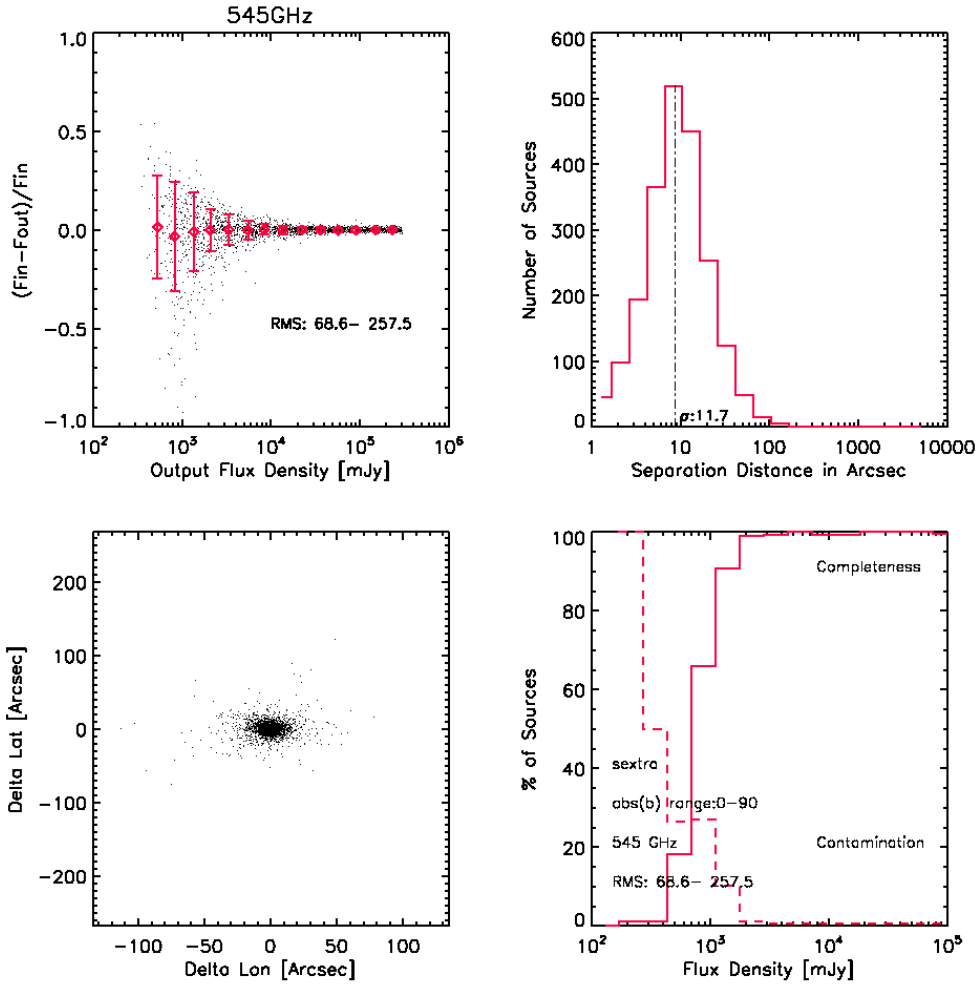
545GHz
(Fin−Fout)/Fin
Output Flux Density [mJy]
RMS: 68.6− 257.5
Number of Sources
Separation Distance in Arcsec
σ:11.7
Delta Lat [Arcsec]
Delta Lon [Arcsec]
% of Sources
Flux Density [mJy]
Completeness
Contamination
sextra
abs(b) range:0−90
545 GHz
RMS: 68.6− 257.5

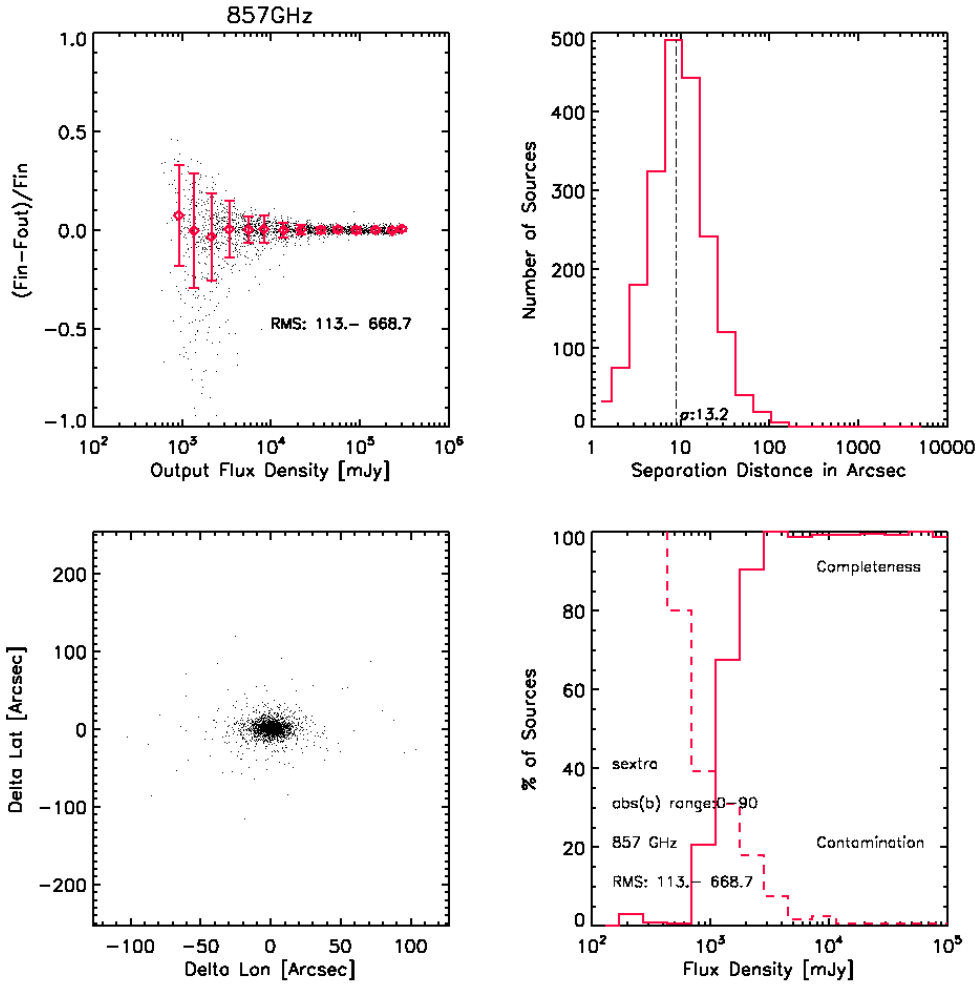
857GHz
(Fin−Fout)/Fin
Output Flux Density [mJy]
RMS: 113.– 668.7
Number of Sources
Separation Distance in Arcsec
σ:13.2
Delta Lat [Arcsec]
Delta Lon [Arcsec]
% of Sources
Flux Density [mJy]
Completeness
Contamination
sextra
abs(b) range:0–90
857 GHz
RMS: 113.– 668.7

and if sources have any of the pixels within a radius of a FWHM being associated with a gap, the source is rejected. This prevents edge effects due to the side lobes of bright planets from being classified as sources.

Second, the source is required to have either an aperture photometry SNR ≥ 5 or a detection method photometry SNR ≥ 5. This implies that either FLUX/FLUX_ERR ≥ 5.0 or a FLUXDET/FLUXDET_ERR ≥ 5.0. The distinction is important due to the fact that the detection method (i.e. PowellSnakes) photometry consistently underestimates the flux density for even marginally extended sources at the lower frequencies.

Third, due to the requirements on the flux density accuracy in the catalog, the standard deviation in the photometric error for Monte-Carlo sources with this SNR is required to be less than 30%.

In order to eliminate extended sources associated with substructure in the Galactic ISM, we eliminate non-circular sources (ELONGATION $\leq$3.0) in the upper HFI bands. These are sources whose ratio of major to minor axis is greater than 3. The quantity is only defined for the frequencies where SExtractor is used.

We also insist that the aperture flux density is positive (FLUX ≥ 0), which alleviates problems due to sources whose sky background estimate is biased high by the presence of bright sources in the sky annulus. These sources will have uncertain photometry and are therefore rejected.

The final ERCSC compilation is the list of sources which have satisfied the primary Monte-Carlo based reliability criterion as well as all the aforementioned secondary QA criteria. These cuts imply that about half the sources in the uncut lower frequency catalogs and about a third of the sources in the upper frequency catalogs are classified as high reliability sources.

7.3. CMB Subtraction

The entire ERCSC is generated on the intensity maps. In addition, a set of all sky maps have been generated which have the contribution of the CMB estimated and removed at each frequency. This has been done independent of the ERCSC pipeline. In the first step, a Mexican hat wavelet filter is used to detect sources. All sources with an SNR greater than 5 were masked with a masking radius of 1.27 FWHM of the effective beam at that frequency. A series of Galactic masks were then constructed from the 30 GHz and 353 GHz frequency channel maps. The missing pixels due to the point source and Galactic masking

are then filled in by a simple "diffusive inpainting" technique. The maps were smoothed to a common resolution of 1°. A Needlet Internal Linear Combination method was used to fit for the CMB template. This technique which uses spherical wavelets, allows localization of emission both in multipole and sky direction. It was preferred to other techniques since it contained the lowest noise level at small scales.

The goal of the CMB estimation step is twofold. The first is to reduce the noise contribution of the CMB in the maps. The second is to identify possible sources which might have the spectrum of the CMB and would have been misidentified as real sources in the ERCSC. At the present time, the estimation of the CMB from the intensity maps is still imprecise and subject to some uncertainty. Real sources which are confused or faint are propagated into the maps of the CMB because of insufficient masking. As a result, we do not use the CMB subtracted maps for the ERCSC catalog but instead use the maps for the generation of the postage stamp cutouts for each ERCSC source since it provides a cleaner, higher SNR visualization for the majority of sources.

In addition, the ERCSC pipeline has been re-run on these CMB subtracted maps and a separate catalog of sources generated. If high reliability ERCSC sources are present in the raw catalogs from the CMB subtracted maps with a flux density difference of less than 30% compared to the ERCSC flux density, they have the CMBSUBTRACT flag set to 0. If high reliability ERCSC sources are present in the raw catalogs from the CMB subtracted maps with a flux density difference of more than 30% compared to the ERCSC flux density, they have the CMBSUBTRACT flag set to 1. The value of CMBSUBTRACT is 2 if an ERCSC source is not present in the CMB subtracted maps. The most likely reason for this is that the source was initially not masked and therefore propagated into the CMB maps. When the CMB contribution was subtracted from the intensity maps, the source was thereby subtracted. However, in certain cases, the ERCSC source may indeed be a CMB bump but this scenario cannot be clearly identified at the spatial resolution of *Planck*. A conservative user should be inclined to neglect sources with CMBSUBTRACT=2.

8. Characterization of ERCSC Between the *Planck* Bands

In order to characterize the nature of sources seen in the ERCSC list, we attempted to identify association between adjacent frequencies. A source, called source 1, at frequency 1 is associated with a source, called source 2, at frequency 2 if it lays within $(\mathrm{FWHM}_1 + \mathrm{FWHM}_2)/2$, if source 2 is the closest source at frequency 2 to source 1, and if source 1 is the closest source at frequency 1 to source 2. The results are summarized in Table 8. Naturally, at the lowest frequency, 30 GHz, it is impossible to find associations at a lower frequency and hence columns B & C are blank. Similarly, at the highest frequency, 857 GHz, it is impossible to find associations at a higher frequency and hence columns B & D are blank.

Armed with these associations, we then investigate the spectral indices of the sources in column (B) above (i.e., those sources for which we have detections in three consecutive bands), assuming a frequency dependence of $S_\nu \propto \nu^\alpha$. The results are shown in Figures 8 and 9.

As might be expected, there seem to be at least three populations: at the lowest frequencies, there is a population of sources with $\alpha \simeq -2$. Across most of the *Planck* bands, there exists a population with $\alpha \simeq -1/2$. And at the higher Planck frequencies, there is a population with $\alpha \simeq 3$.

These colors also clearly demonstrate the contamination of the 100 GHz flux density by CO emission. Near the Galactic plane (in figure 8), the "dust-like" sources have spectral indices near 3. However, in the central plot, this changes drastically to almost zero for the 143/100 index. Similar, but smaller deviations at the higher frequencies may indicate contamination from other lines. These lines should be taken into account in any analysis.

9. Validation of ERCSC with Ancillary Catalogs

We have also attempted to validate the properties of source in the ERCSC catalogs by comparing with ancillary catalogs (Planck Collaboration 2011n). As noted earlier, this is challenging since sources vary, ancillary catalogs are not at the same frequency and all sky coverage at frequencies corresponding to the *Planck* frequencies is not available. Yet, at specific radio frequencies, surveys of similar depth exist and we assess if the ERCSC sources are present in those surveys.

Table 8. Source Matches in Adjacent Bands

Frequency	A	B	C	D	E	F
30	705	-	-	379	379	0.54
44	452	334	379	388	433	0.96
70	599	363	389	520	546	0.91
100	1381	496	520	1104	1128	0.82
143	1764	929	1106	1357	1534	0.87
217	5470	1067	1357	4190	4480	0.82
353	6984	2848	4189	4244	5585	0.80
545	7223	3404	4245	5363	6204	0.86
857	8988	-	5365	-	5365	0.60

[A]Total Number of sources detected

[B]Number of sources detected both at frequency just below and just above given frequency

[C]Number of sources detected at frequency just below given frequency

[D]Number of sources detected at frequency just above given frequency

[E]Number of sources detected either at frequency just below or just above given frequency

[F]Fraction of sources detected either at frequency just below or just above given frequency

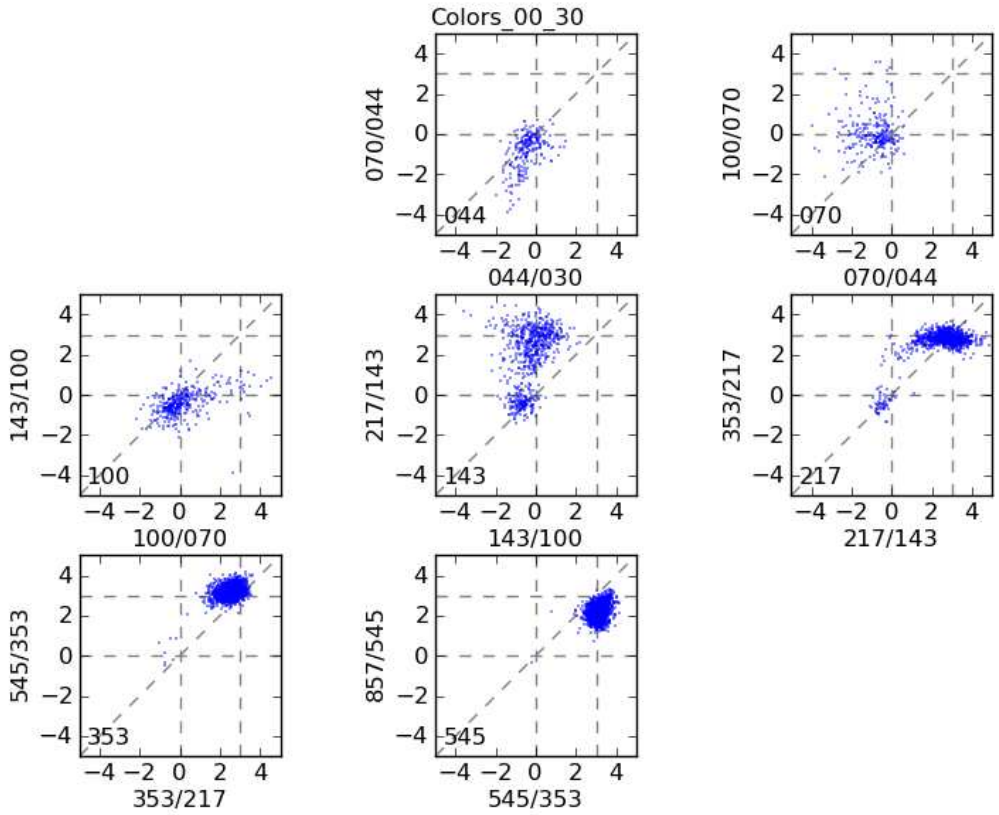

Fig. 8.— Colors of sources detected in three consecutive bands for which $0° < |b| < 30°$, assuming $S_\nu \propto \nu^\alpha$, where S_ν is in Janskys. The axis labels indicate the two frequencies for which the spectral index corresponds. E.g., 143/100 indicates a spectral index between 100 and 143 GHz. Dashed lines are overplotted at values of 0 and 3 and are meant only to guide the eye. A line of unit slope and zero offset is also overplotted in each panel. Note that the sources are in general, not the same across different panels. In particular, between 143 and 217 GHz, the transition from the radio source population to the far-infrared luminous population is clearly evident.

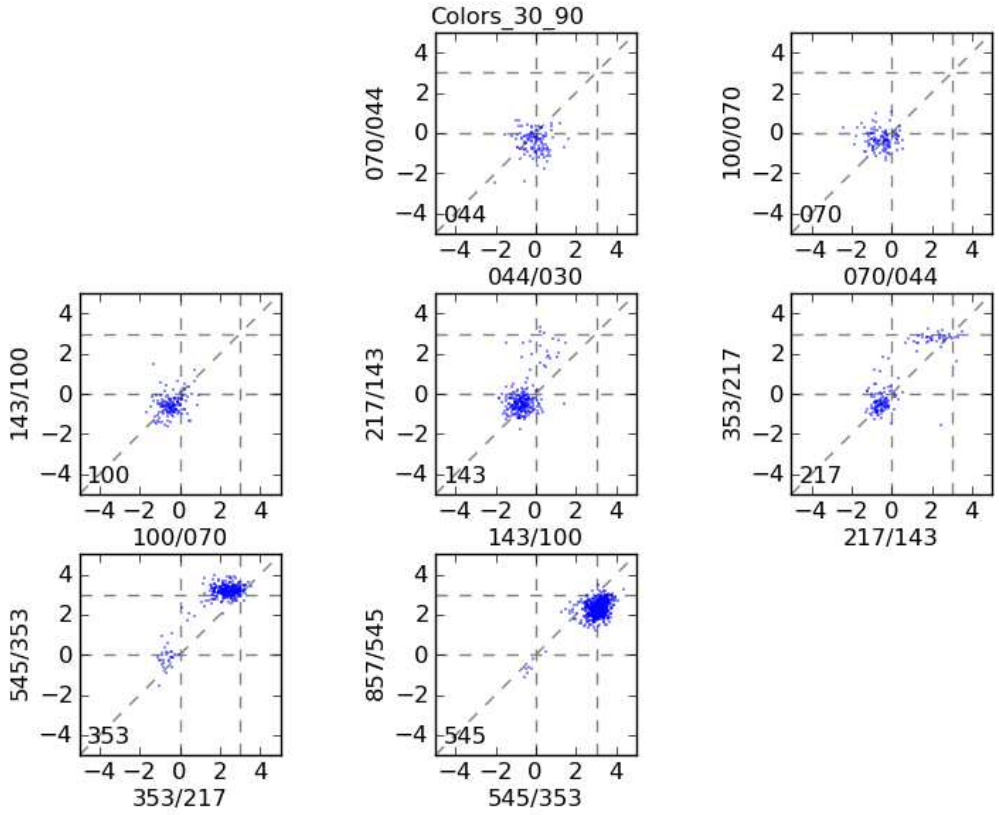

Fig. 9.— Same as figure 8, but for sources for which $30° < |b| < 90°$

9.1. Positional Accuracy

Although the Monte Carlo analysis returns the uncertainty in the source positions due to fitting/centroiding uncertainties, it does not account for any absolute astrometric offsets in the map. We assessed the absolute pointing uncertainties of the ERCSC catalogs by comparing the ERCSC sources with a list of GB6 (Gregory et al. 1996) and PMN (Griffith et al. 1994, 1995; Wright et al. 1994, 1996) quasars obtained from NED at 30 to 353 GHz bands. For a given quasar, a searching radius of 1 FWHM is used to select a ERCSC match at each band. The number of matches and the median offsets between the ERCSC source positions and the quasar centroids are given in Table 9.

Figure 10 shows the histograms of centroid separations for matched quasar/ERCSC sources, along with the centroid separation scatter plots. We find no systematic offset in the GLON or GLAT positions of the ERCSC sources. The median radial offsets at all bands are smaller than a tenth of the Planck beams, showing that the ERCSC pipeline is recovering the source positions as expected.

9.2. Comparison Between *Planck* and WMAP

The WMAP seven-year catalog (Gold et al. 2010) contains a total of 471 sources in the five WMAP bands. We have compared the WMAP 5σ sources at 33, 41, 61, 94 GHz with the sources in the ERCSC catalogs at 30, 44, 70 and 100 GHz, respectively. A searching radius of 1 FWHM of the WMAP beam at each frequency (0.66°, 0.51°, 0.35°, 0.22° at 33 to 94 GHz channels) is used to find a match of WMAP source in the ERCSC catalog. Figure 11 shows the histogram distribution of WMAP sources with respect to their flux densities: the WMAP 5σ sources are shown in gray, and the ones with an ERCSC match are in red. The ERCSC catalogs include 88%, 62%, 81% and 95% of the WMAP 5σ sources at the

Table 9. QSO Matches in ERCSC Catalogs

Band [GHz]	FWHM [’]	Detection method	matches	median offset [’]
30	32.65	PowellSnakes	357	1.99
44	27.00	PowellSnakes	185	1.68
70	13.01	PowellSnakes	198	1.09
100	9.94	PowellSnakes	353	0.79
143	7.04	PowellSnakes	421	0.66
217	4.66	SExtractor	308	0.31
353	4.41	SExtractor	138	0.35

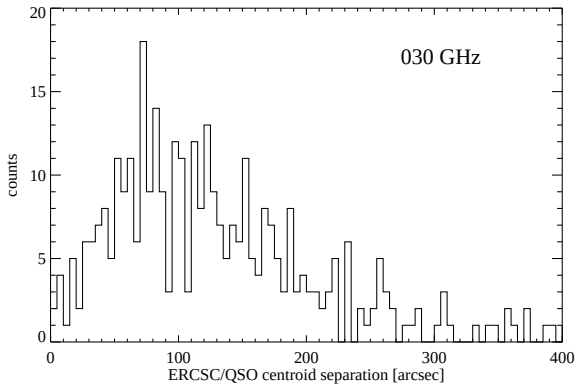
030 GHz
counts
ERCSC/QSO centroid separation [arcsec]

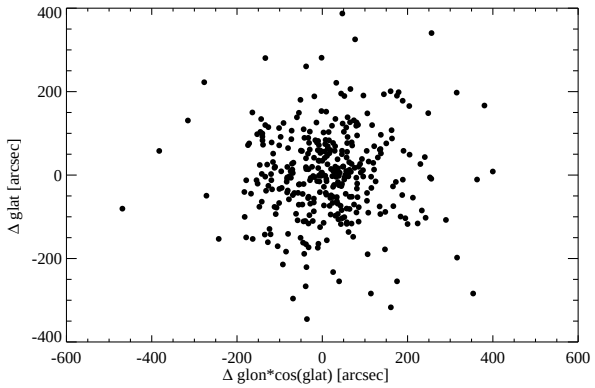
Δ glat [arcsec]
Δ glon*cos(glat) [arcsec]

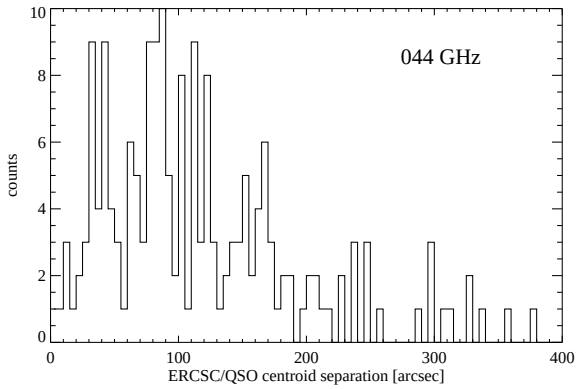
044 GHz
counts
ERCSC/QSO centroid separation [arcsec]

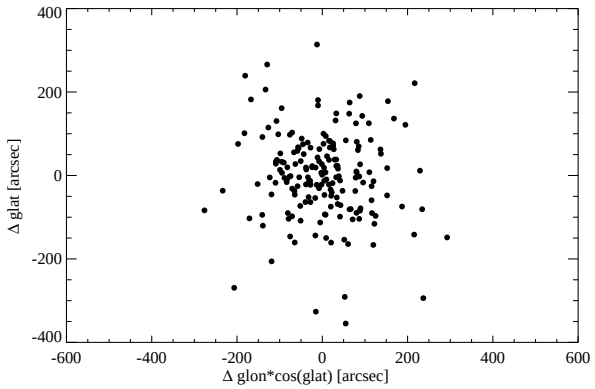
Δ glat [arcsec]
Δ glon*cos(glat) [arcsec]

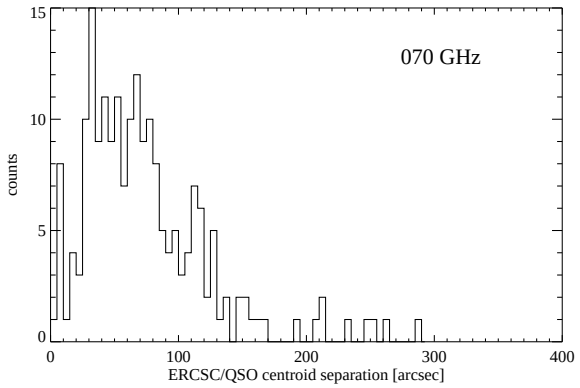
070 GHz
counts
ERCSC/QSO centroid separation [arcsec]

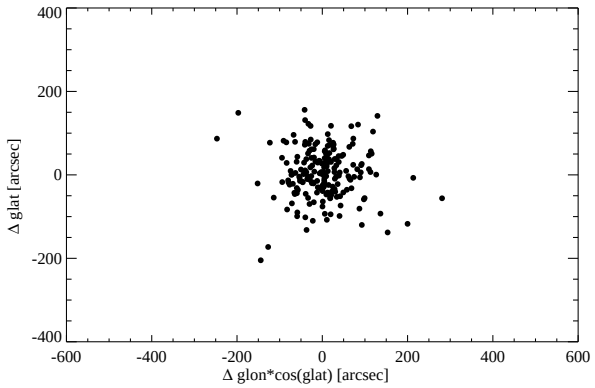
Δ glat [arcsec]
Δ glon*cos(glat) [arcsec]

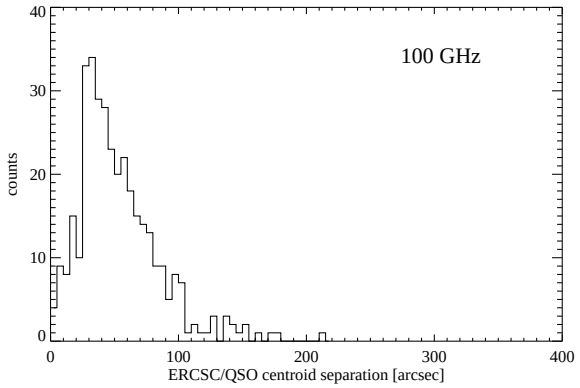
100 GHz
counts
ERCSC/QSO centroid separation [arcsec]

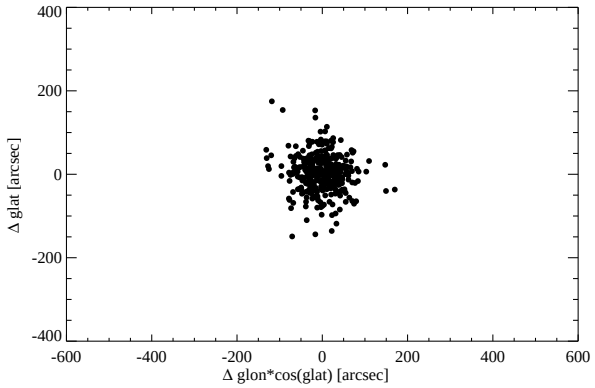
Δ glat [arcsec]
Δ glon*cos(glat) [arcsec]

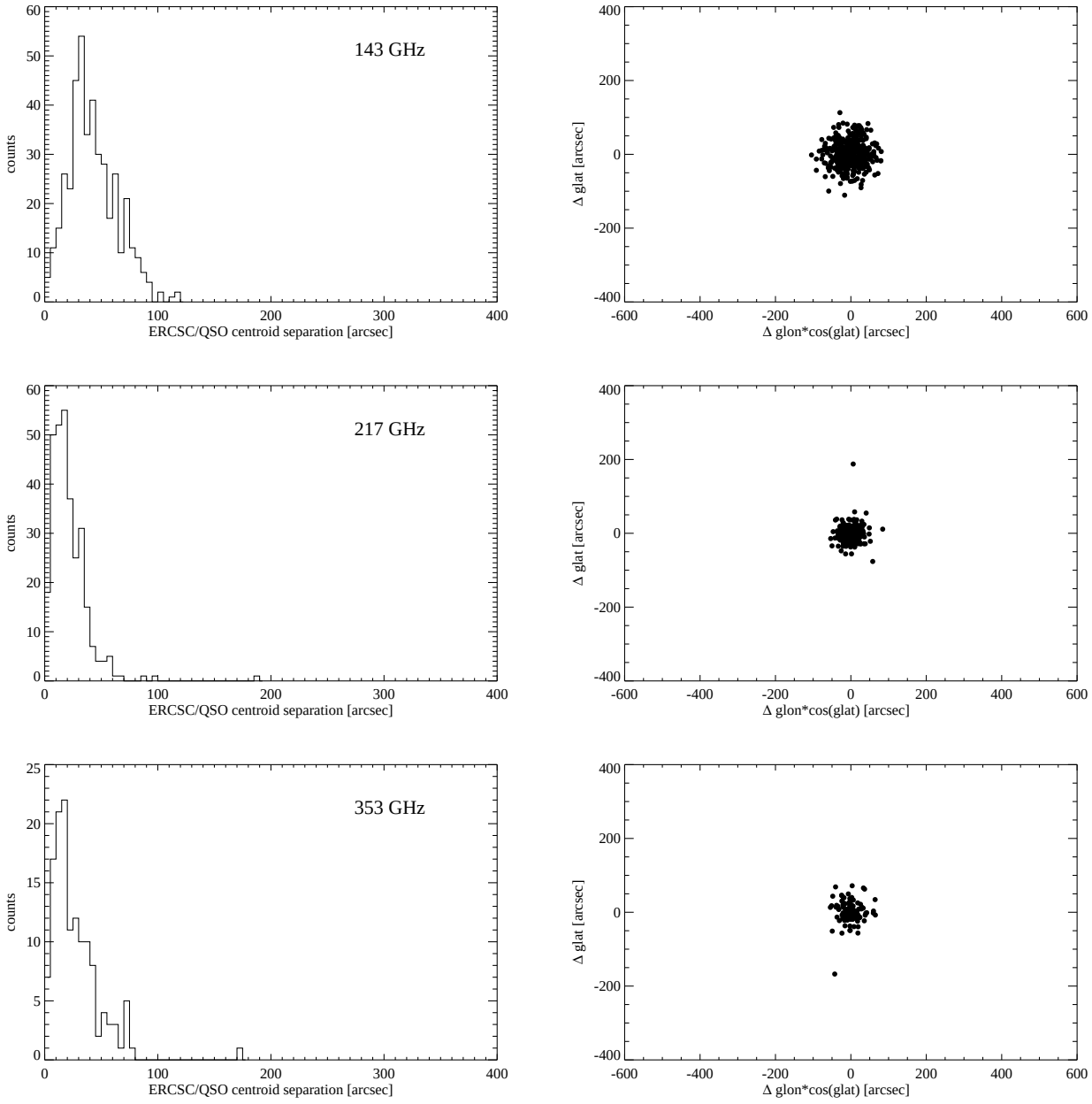

Fig. 10.— Quasar matches and position offsets in ERCSC 30 to 353 GHz catalogs. There are insufficient numbers of detected quasars at the upper HFI frequencies.

four bands, individually. Figure 12 is a similar plot, but shows the histogram distribution of the ERCSC sources with respect to their flux densities: the ERCSC sources are shown in gray, and the ones with a WMAP match are in red. The WMAP seven-year point source catalog mask which excludes the Galactic Plane and the LMC/SMC region has been applied to the ERCSC catalogs beforehand to ensure the same sky coverage. It is evident that the ERCSC is a much deeper and more complete catalog than WMAP, especially at the 100 GHz channel.

In Figure 13 to Figure 16, we have plotted the sky distribution of the WMAP sources (red open circle) and *Planck* sources (black dot). A black dot circled with red naturally indicates a match. For the matched sources, we then checked their flux densities and position offsets. Overall there is no systematic difference between WMAP and ERCSC flux densities at the corresponding bands. The large scattering suggests that variability is likely an issue. There is no variability analysis of the WMAP seven-year point sources, but an analysis of the variability on the five-year WMAP point sources shows that 35% of the sources are variable at greater than 99% confidence, and these are in general the brighter sources (Wright et al. 2009). The median position offsets between ERCSC sources and its WMAP companions are at its largest of 2.5 arcmin at 30 GHz.

The WMAP 5σ detections that are missed in the ERCSC catalogs at 30, 70 and 100 GHz are further investigated. The 44 GHz channel is skipped since it is known to have low sensitivity. It is found that at 100 GHz, all the missed WMAP sources can be explained by that the WMAP source either does not have a 5 GHz ID or weakly associated with a 5 GHz source (so they could be spurious). At 70 GHz, $\sim 41\%$ of the unmatched sources are variable (this is a lower limit as the variability info was obtained from the WMAP five-year catalog, which is a subset of the WMAP seven-year catalog), $\sim 13\%$ of the unmatched sources have no 5 GHz ID or only loosely associated with a 5 GHz source, $\sim 38\%$ are recovered after the CMB subtraction. At 30 GHz, $\sim 17\%$ of the unmatched sources are variable (again, this is only a lower limit), $\sim 34\%$ of the unmatched sources have no solid identification, $\sim 54\%$ are recovered after the CMB subtraction. All above suggests that the reason these sources are not detected in *Planck* is a combination of source variability, map sensitivity (different scanning strategy of WMAP and *Planck* result in the difference of local background noise; also ERCSC is based on 1.6 sky survey whereas the WMAP catalog is based on 14 sky surveys), and incompleteness of the ERCSC catalogs.

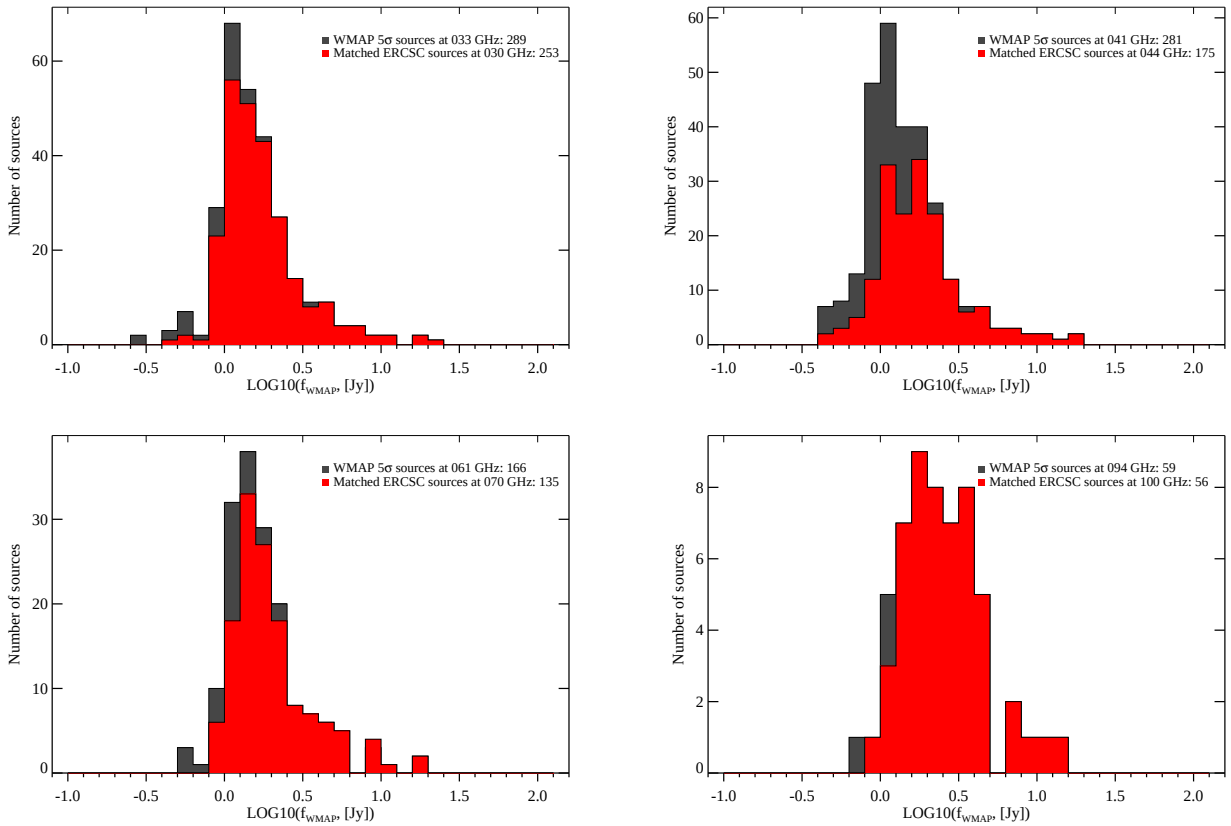

Fig. 11.— Histogram distribution of WMAP 5σ sources at each band in gray, with those included in the ERCSC catalogs in red.

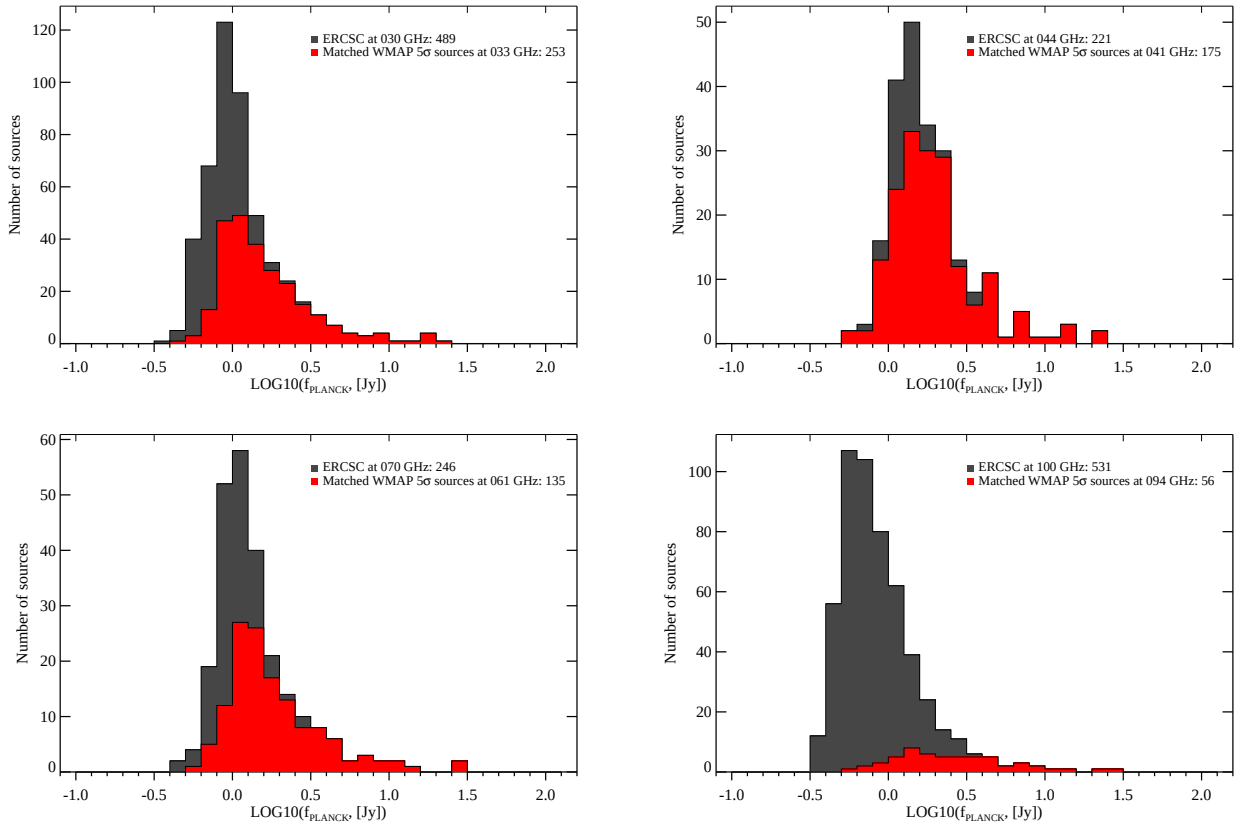

Fig. 12.— Histogram distribution of ERCSC sources at each band in gray, with the matched WMAP 5σ sources at each band in red. The WMAP 7 year point source catalog mask (see text) has been applied to the ERCSC catalogs to ensure the same sky coverage.

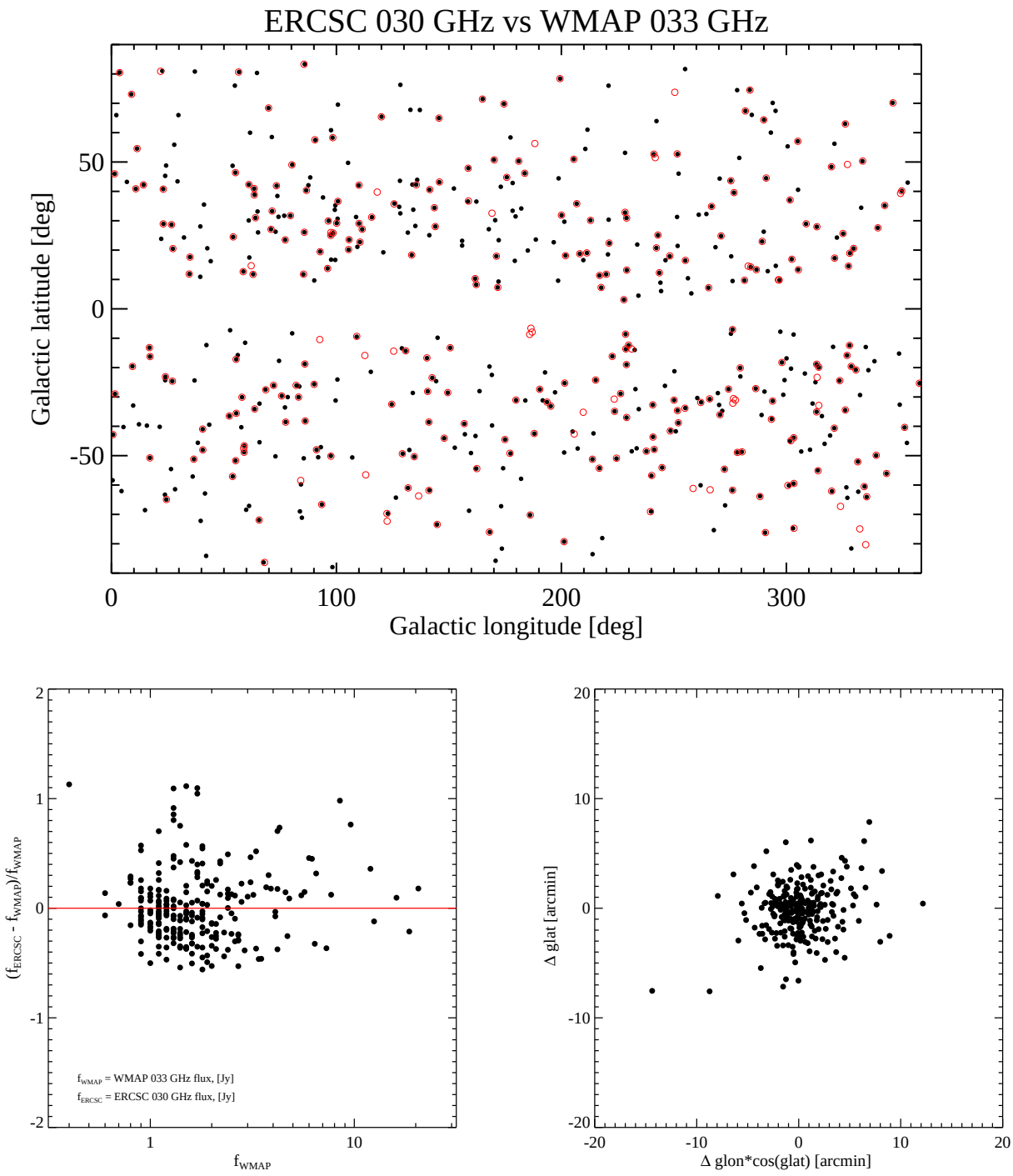

Fig. 13.— Upper plot: Sky distribution of the ERCSC sources at 30 GHz (black dots), WMAP sources at 33 GHz (red open circles). The matches are indicated by black dots circled with red. Lower left: Flux comparison of the matched sources. The red line is to guide the eye to see where the data points should be if WMAP 33 GHz and *Planck* 30 GHz flux densities were the same. Lower right: Position offset of ERCSC sources with respect to their WMAP counterparts.

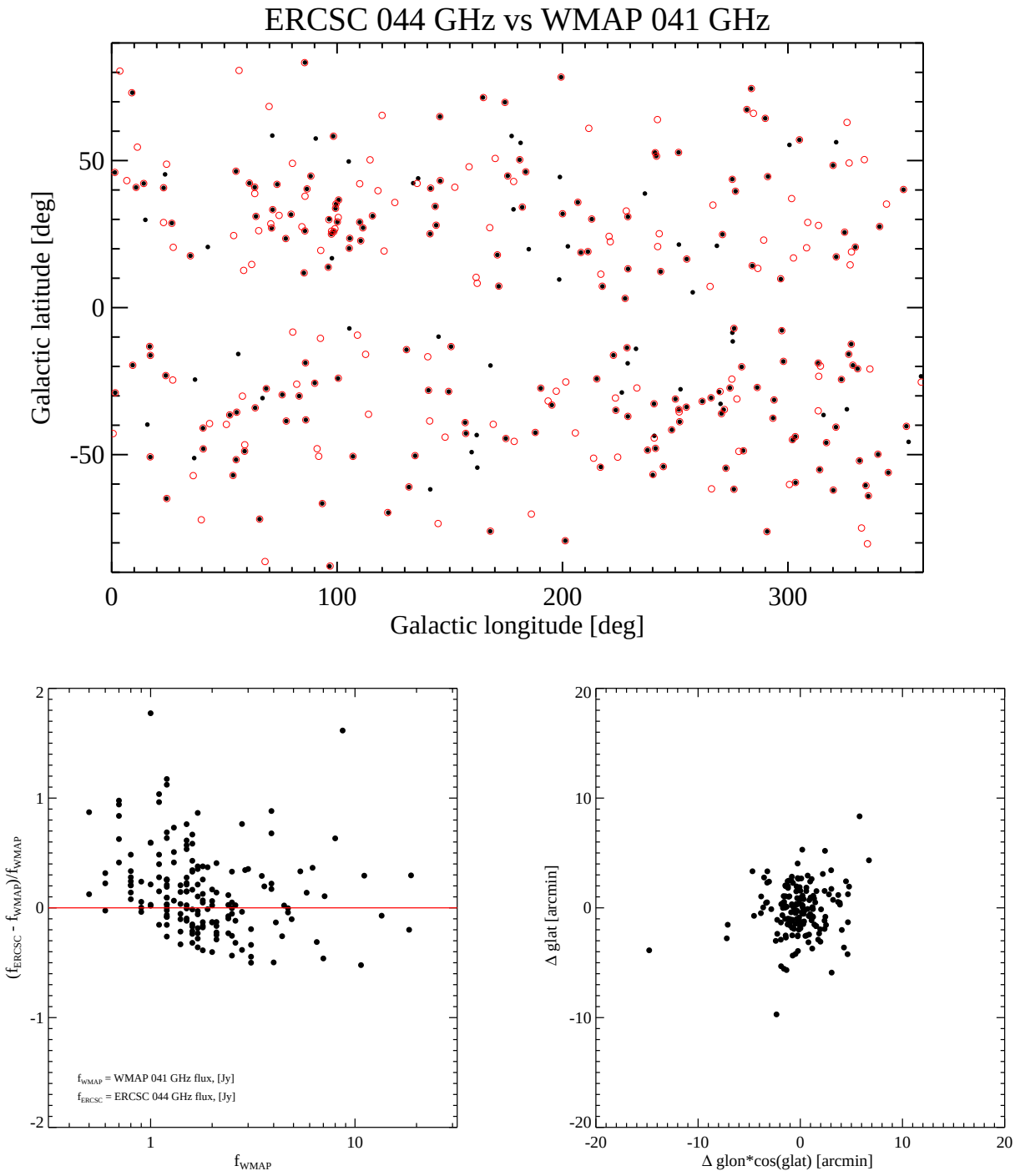

Fig. 14.— Upper plot: Sky distribution of the ERCSC sources at 44 GHz (black dots), WMAP sources at 41 GHz (red open circles). The matches are indicated by black dots circled with red. Lower left: Flux comparison of the matched sources. The red line is to guide the eye to see where the data points should be if *Planck* 44 GHz and WMAP 41 GHz flux densities were the same. Lower right: Position offset of ERCSC sources with respect to their WMAP counterparts.

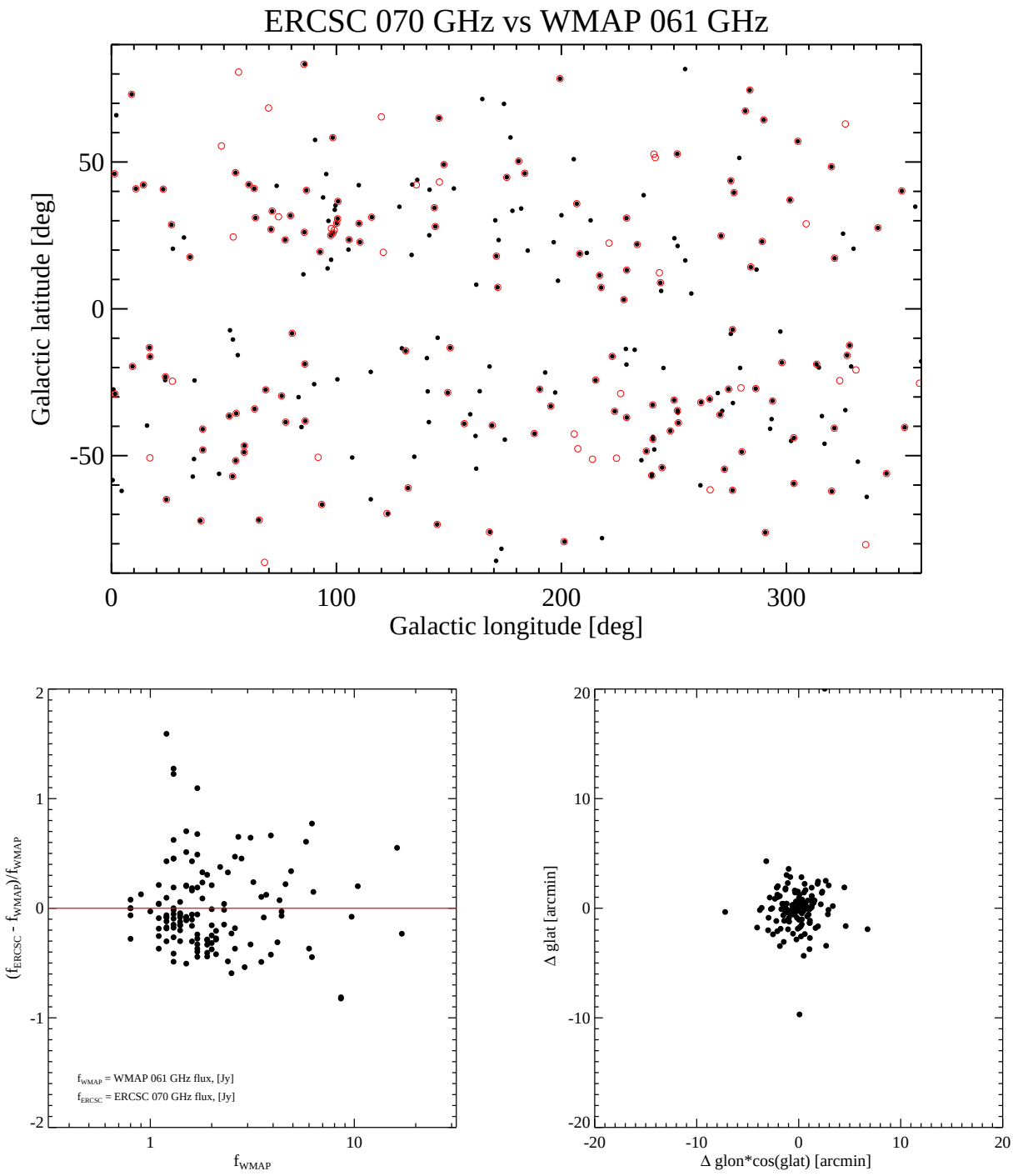

Fig. 15.— Upper plot: Sky distribution of the ERCSC sources at 70 GHz (black dots), WMAP sources at 64 GHz (red open circles). The matches are indicated by black dots circled with red. Lower left: Flux comparison of the matched sources. The red line is to guide the eye to see where the data points should be if *Planck* 70 GHz and WMAP 64 GHz flux densities were the same. Lower right: Position offset of ERCSC sources with respect to their WMAP counterparts.

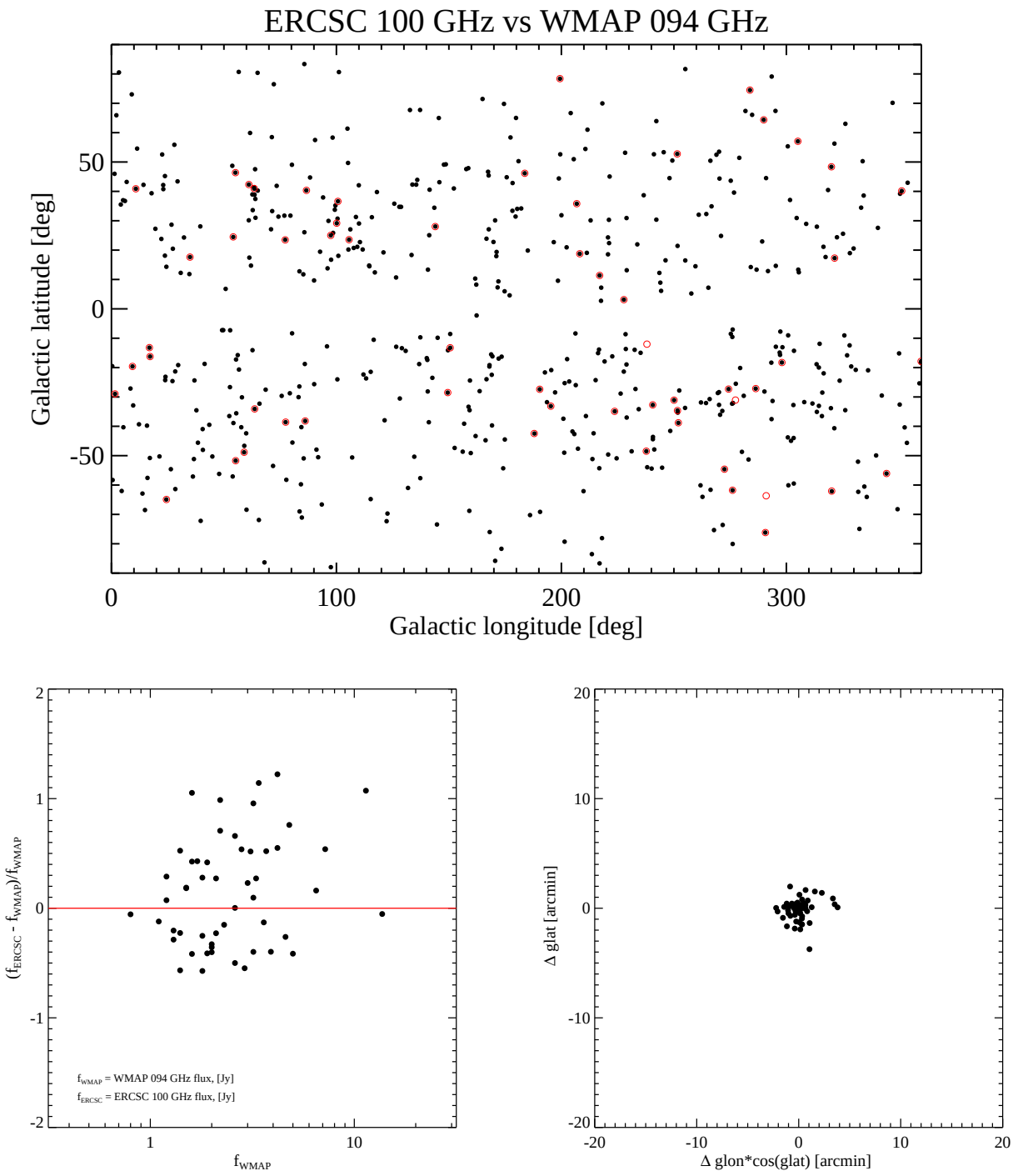

Fig. 16.— Upper plot: Sky distribution of the ERCSC sources at 100 GHz (black dots), WMAP sources at 94 GHz (red open circles). The matches are indicated by black dots circled with red. Lower left: Flux comparison of the matched sources. The red line is to guide the eye to see where the data points should be if WMAP 94 GHz and *Planck* 100 GHz flux densities were the same. Lower right: Position offset of ERCSC sources with respect to their WMAP counterparts.

9.3. Assessment of Flux Densities with a Predictive Flux Catalog

A predictive flux catalog has been compiled which consists of the predicted flux densities at *Planck* frequencies for some bright, well-known sources. It uses data from the comprehensive NASA/IPAC Extragalactic Database (NED), and thus can be easily updated. The catalog is built from measurements available in the literature and extrapolated to the *Planck* frequency bands using a simple model of the SED for each source. Such a catalog is intended for testing and quality assessment of the ERCSC catalog. It is also a useful check on the absolute calibration of Planck data.

Candidate sources must be point like, bright (>>1 Jy in *Planck* bands), in an uncrowded region of sky at high galactic latitude, non-variable and have known measurements around the *Planck* bands for a reliable prediction to be made. The predictive flux catalog comprises 22 sources, which are summarized in Table 10. The SED models used to predict the flux densities at *Planck* bands are:

- Simple power law, $S = A_0\nu^{A_1}$, 2 parameters
- One component dust model, $S = A_4 \times \nu^{A_5} B(\nu, A_6)$, 3 parameters
- Power Law plus one component dust model, $S = A_0\nu^{A_1} + A_4 \times \nu^{A_5} B(\nu, A_6)$, 5 parameters

A_0 and A_1 are the amplitude and spectral index of the power law respectively. A_4, A_5 and A_6 are the amplitude of the blackbody, the dust emissivity index and the blackbody temperature respectively. The values of these parameters for a representative subset of the predictive flux catalog sources is shown in Figure 18.

We compare the predicted fluxes with the flux density ("FLUX" in the catalogs) from the ERCSC pipeline, and the results are shown in Figure 18. Overall, this comparison suggests that the ERCSC flux densities for these sources are as expected. There are two exceptions, 545 and 857 GHz, where, even though there is a large scatter, the ERCSC flux densities appear to be systematically greater than the predictions. It must be noted that complex dust properties makes it difficult to accurately predict flux densities in the higher HFI bands and therefore we interpret the large scatter as a measure of our ignorance of the far-infrared/submillimeter properties of galaxies rather than as a measure of the uncertainty in the ERCSC flux densities.

The SEDs of the predicted flux catalog sources must be individually examined to determine if the ERCSC is performing as expected or whether the predicted flux density is incorrect. The SED of a representative sample of 6 predictive flux catalog sources is shown

in Figure 19. The SED plots show the ERCSC is getting good results in all bands for M1 (Crab) and Pictor A. For the thermal dust emission, the ERCSC flux densities appear to be higher than the predictions. This is partly attributable to the difficulty in predicting the far-infrared/submillimeter flux densities for galaxies from the existing ground-based data (e.g. *Planck* Collaboration 2011p). It could also partly be due to the contribution from Galactic cirrus and CO emission in some of these bandpasses. Due to the excellent agreement between the predicted and the observed values for pure power-law sources such as the Crab, it is unlikely that the difference is due to calibration systematics.

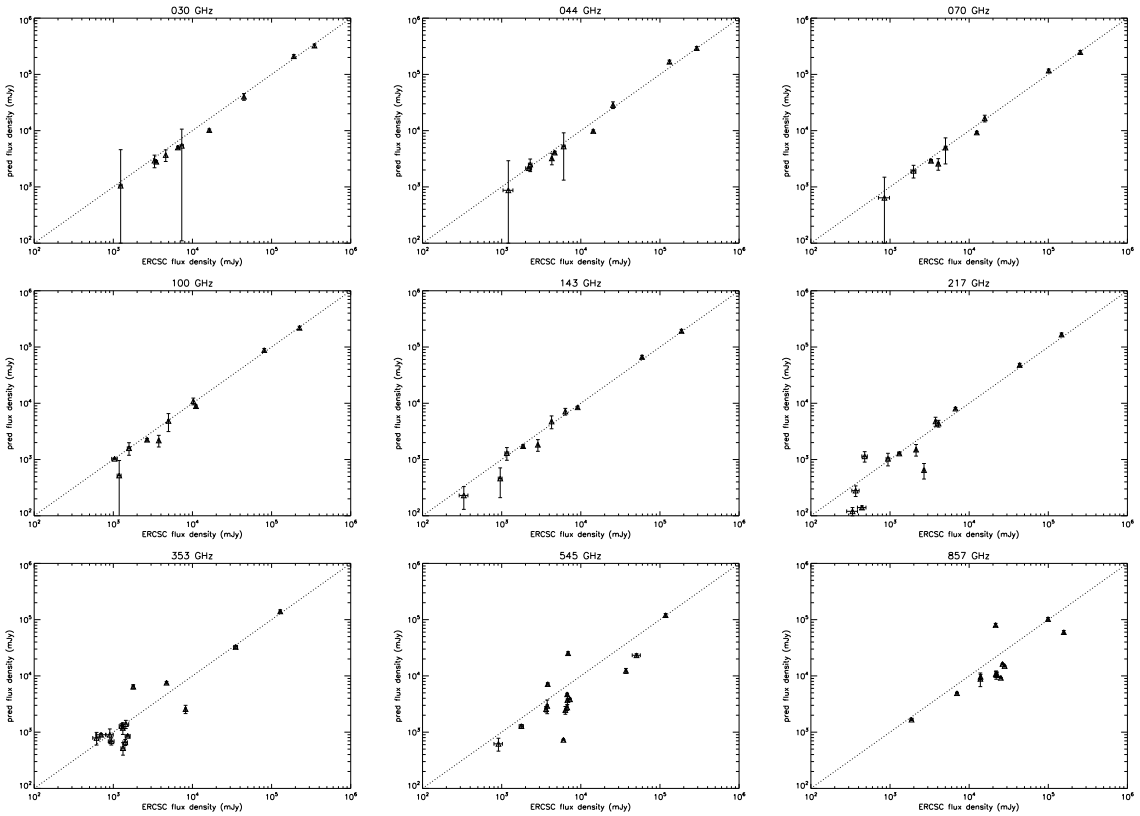

Fig. 17.— Comparison of the predicted and ERCSC flux densities for all predictive catalog sources.

Table 10: Summary of the 22 predictive flux catalog sources.

Name	Type	Angular Size (arcmin)	Useful freq. range	Notes
0637-752	Radio QSO	Pt source	All	Likely more reliable at lower freqs
1921-293	Radio source	Pt source	All	Flat-spectrum. Variable.
3C123	Radio galaxy	< 1	< 353	Well fit by a power-law. Radio lobes <1' apart.
3C461	Cas-A SNR	~ 5	All	Well defined power-law spectrum
Arp220	Starburst	~ 1.5	> 353	Reasonable fit
Cygnus-A	Radio galaxy	Pt source	< 545	Simple power-law better fit than modified BB.
ESO075-G041	Radio galaxy	~ 1.6	< 353	
M1	Crab SNR	$\sim 6 \times 4$	All	Very bright and power-law good model
M61	Sy 2 galaxy	6.5×5.8	> 353	Dominated by dust emission
M82	Starburst	11.2×4.3	> 217	Possibly detectable at lower frequencies
M88	Sy 2 galaxy	6.9×3.7	> 353	Not a good fit, but 1000 GHz data ok
M99	LINER gal	5.4×4.7	> 353	Model not a good fit near 200-400 GHz data
NGC157	Sp galaxy	4.2×2.7	> 353	60 μm not a good fit. 1000 GHz data ok
NGC520	Gal pair	~ 4.5	> 400	
NGC660	LINER gal	8.3×3.2	> 217	Power-law better fit than modified BB.
NGC1808	Sy 2 galaxy	6.5×3.9	> 353	
NGC3079	LINER gal	7.9×1.4	> 250	240GHz data point a little higher than model
NGC4490	SB sp gal	$\sim 6 \times 3$	> 200	Current data at $\sim$ 200-300GHz is well fit by model.
NGC7027	PNe	Pt source	All	Based on Hafez et al. (2008). Decreasing at $< 1\%$/yr
Pictor-A	Sy 1 gal	Pt source	< 500	Power-law good fit. Likely more reliable at lower freqs
UGC02855	SABc galaxy	4.4×2.0	> 545	
UGC08058	Sy 1 gal	1.3×1.0	> 800	

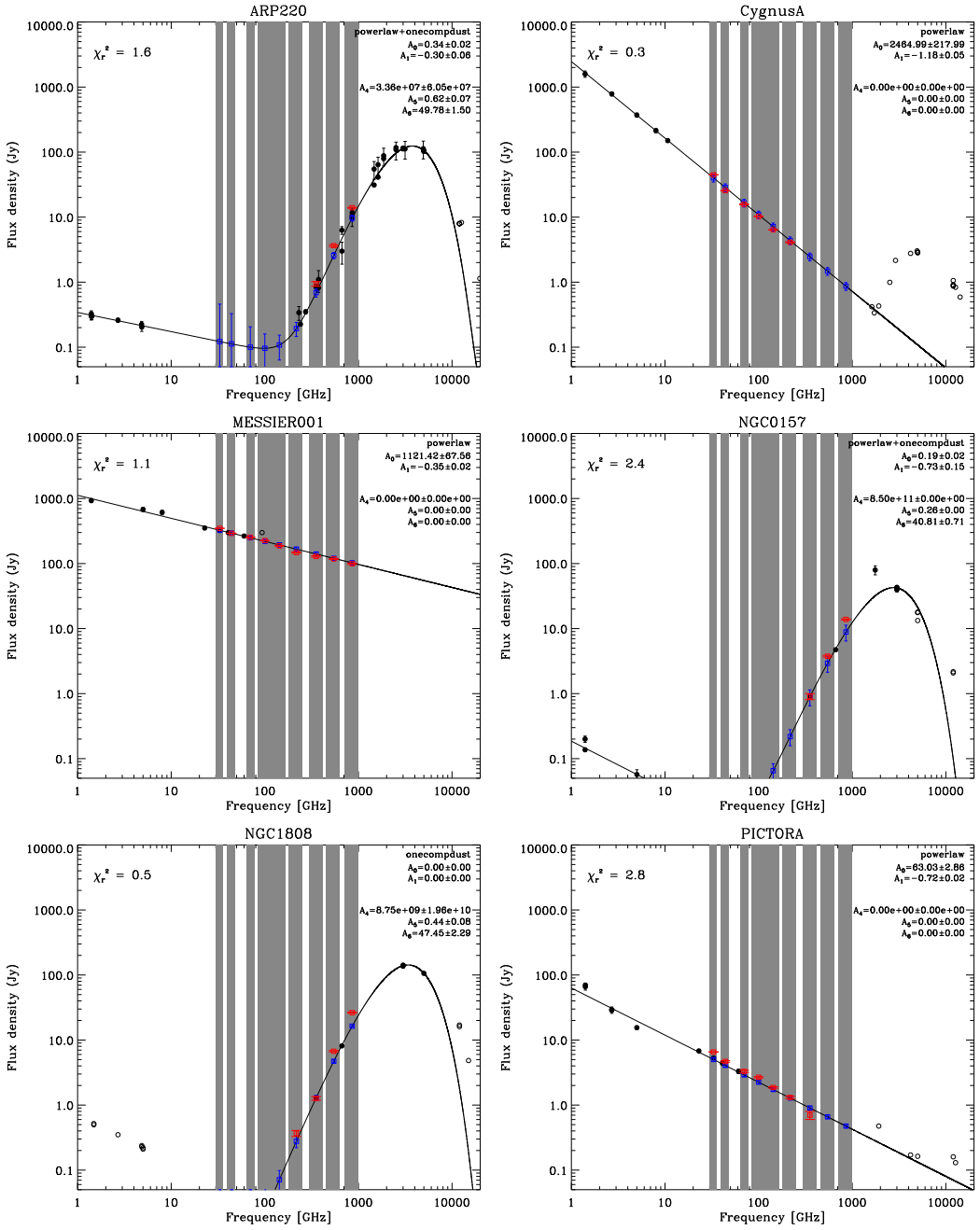

Fig. 18.— The SEDs of a subset of the predictive flux catalog sources. Blue marks the prediction and red is the recovered ERCSC flux density. Solid circles show flux densities which were used in the predictive fits while empty circles shown flux density estimates that were ignored. The χ^2 of the fit is also shown in the top left corner.

10. Contents of ERCSC

The primary product in the *Planck* Early Release Compact Source Catalog consists of source lists at each of the nine *Planck* frequencies. The ERCSC catalog lists the positions and flux densities of both Galactic and extragalactic sources with the radio galaxy population the dominant extragalactic contributor at lower frequencies and infrared luminous galaxies being the dominant contributor at higher frequencies.

Emphasis has been placed on making ERCSC reliable; completeness is not a requirement partly due to the significant variation in limiting sensitivity as a function of sky position. The ERCSC list is not to be used for statistical purposes (such as source counts versus flux density or color) without appropriate corrections, due to the large variation in sensitivity with position on the sky. The 857 GHz source list has been enhanced by including flux density measurements, at the position of each 857-GHz detected source, at 545, 353, and 217 GHz. Here, we describe the properties of the ERCSC lists.

10.1. ERCSC FITS Header

Each ERCSC source list is published as a FITS binary table file. The FITS header information for each file is documented in Table 11.

Table 11. ERCSC FITS Header Contents

FITS Keyword	Description
INSTRUME	LFI or HFI
BANDFREQ	Band frequency (GHz)
VERSION	Version of catalogs
DATE	Date file created: yyyy-mm-dd
ORIGIN	Name of organization responsible for the data (U.S Planck Data Center)
TELESCOP	PLANCK
DATE-OBS	Start-up time of the survey: *yyyy-mm-dd*
DATE-END	Ending time of the survey: *yyyy-mm-dd*

10.2. ERCSC Table Format

The ERCSC source list in each band is structured as a FITS binary table having one row for each detected source. The table format described here lists the columns supplied for each source in the catalog. Several of the parameters given here are derived from the lower-level source extraction algorithms, specifically, aperture photometry, moment analysis, beam PSF fitting, and general 2-D Gaussian fitting. Table 12 lists the source columns for the ERCSC release.

Table 12. ERCSC FITS Binary Table Contents

Column Name	Description
	Identification
NAME	Source name[1]
FLUX	Flux density (mJy)[2]
FLUX_ERR	Flux density error (mJy)[2]
CMBSUBTRACT	Flag indicating detection of source in CMB subtracted maps[3]
EXTENDED	Flag indicated that source is extended[4]
DATESOBS	UTC dates at which this source was observed[5]
NUMOBS	Number of days this source observed
CIRRUS	Cirrus flag based on 857 GHz source counts
	Source Position
GLON	Galactic longitude based on extraction algorithm
GLAT	Galactic latitude based on extraction algorithm
POS_ERR	Standard deviation of positional offsets for sources with this SNR
RA	Right Ascension (J2000) transformed from (GLON,GLAT)
DEC	Declination (J2000) transformed from (GLON,GLAT)
	Effective beam
BEAM_FWHMMAJ	Elliptical Gaussian beam FWHM along major axis (arcmin)
BEAM_FWHMMIN	Elliptical Gaussian beam FWHM along minor axis (arcmin)
BEAM_THETA	Orientation of Elliptical Gaussian major axis (measured East of Galactic North)
	Morphology
ELONGATION	Ratio of major to minor axis lengths
	Source Extraction Results
FLUXDET	Flux density of source as determined by detection method (mJy)
FLUXDET_ERR	Uncertainty (1 sigma) of FLUXDET (mJy)
MX1	First moment in X (arcmin)[6]
MY1	First moment in Y (arcmin)[6]
MX2	Second moment in X ($arcmin^2$)[6]
MXY	Cross moment in X and Y ($arcmin^2$)[6]
MY2	Second moment in Y ($arcmin^2$) [6]
PSFFLUX	Flux density of source as determined from PSF fitting (mJy)
PSFFLUX_ERR	Uncertainty (1 sigma) of PSFFLUX (mJy)
GAUFLUX	Flux density of source as determined from 2-D Gaussian fitting (mJy)
GAUFLUX_ERR	Uncertainty (1 sigma) of GAUFLUX (mJy)
GAU_FWHMMAJ	Gaussian fit FWHM along major axis
GAU_FWHMMIN	Gaussian fit FWHM along minor axis
GAU_THETA	Orientation of Gaussian fit major axis (measured East of Galactic North)

Table 12—Continued

Column Name	Description
	Quality Assurance
RELIABILITY	Fraction of MC sources that are matched and have photometric errors < 30%
RELIABILITY_ERR	Uncertainty (1 sigma) in reliabiliy based on Poisson statistics
MCQA_FLUX_ERR	Standard deviation of photometric error for sources with this SNR
MCQA_FLUX_BIAS	Median photometric error for sources with this SNR
BACKGROUND_RMS	Background point source RMS obtained from threshold maps (mJy)
	Bandfilling (857 GHz catalog only)
BANDFILL217	217 GHz Aperture Photometry Flux Density at 857 GHz Source Position (mJy)
BANDFILL217_ERR	Uncertainty in BANDFILL217
BANDFILL353	353 GHz Aperture Photometry Flux Density at 857 GHz Source Position (mJy)
BANDFILL353_ERR	Uncertainty in BANDFILL353
BANDFILL545	545 GHz Aperture Photometry Flux Density at 857 GHz Source Position (mJy)
BANDFILL54_5ERR	Uncertainty in BANDFILL545

[1]Source name designations consist of a prefix and a positional qualifier, which is in Galactic coordinates and specified as "Glll.ll-bb.bb" where the (l,b) values are truncated. The prefix used in the single-band portion of the ERCSC is PLCKERCddd - ERCSC catalog at ddd GHz. For example, a source detected at (l,b) = (120.237, -4.231) in the 545 GHz Planck map would be labeled PLCKERC545 G120.23-04.23.

[2]The measured parameter assigned to the FLUX column is the flux density computed by aperture photometry centered on the detected source position.

[3]The CMBSUBTRACT flag has the value of 0, 1, or 2.

[4]The EXTENDED flag has the value of 0 if the source is compact and the value of 1 is it extended.

[5]The UTC observation dates are presented as a string having the format "YYYYMMDD,YYYYMMDD,...".

[6]The X and Y axes used in moment analysis are defined within local gnomonic projections around each source. At the center of the projection the X and Y axes are parallel to those of constant Galactic latitude and longitude, respectively. The convention of the moments is provided in Section 5.2.2.

10.3. Postage Stamps and Skymaps

10.3.1. Postage Stamps

As an aid to source characterization, we provide postage stamps of the individual sources contained within the ERCSC and ECC catalogs. No postage stamps are provided for the ESZ catalog. This is primarily because the individual frequency postage stamps are not a useful tool for validation of ESZ candidates due to the confusion from ISM structure and CMB emission. In addition, the ESZ candidates have been validated through follow-up observations and cross-matches with ancillary catalogs. The attributes of the ERCSC postage stamps are:

1. Derived from the CMB-subtracted HEALPix maps described in Section 7.3
2. Image size 4×FWHM on a side, aligned with galactic North up
3. Color scale chosen independently for each image

These are delivered in two separate formats:

1. Separate JPEG files for each image, for use in online archives.
2. PDF files with many images per page in order of increasing Galactic longitude, labeled with location (galactic coordinates) and flux density of source in mJy.

10.3.2. Skymaps

Maps showing the distribution of detected sources on the sky are provided as part of ERCSC. The maps are displayed in Galactic coordinates, longitude (GLON) −180 deg to 180 deg, latitude (GLAT) −90 deg to 90 deg, using a simple rectangular (*plate carrée*) projection.

There are 9 ERCSC maps, one for each frequency. Each source is displayed as a dot, color-coded by flux density (FLUX) using a logarithmic scale. A color-bar scale is included, labelled in Janskys. In addition, the ESZ and ECC skymaps are provided which are described in Sections 11 and 12.

Filenames:
ERCSC_f030_skymap.pdf
...

ERCSC_f857_skymap.pdf
ECC_skymap.pdf
ESZ_skymap.pdf

10.4. Notes on Individual Sources

Planck detects sources in a frequency regime which is essentially unexplored. To make the most usage of the ERCSC catalogs, we have looked into external catalogs from large area surveys and tried to associate the ERCSC detections with known sources.

For the 30 to 143 channels, we have cross-correlated the ERCSC catalogs with the WMAP7 catalog at 23 to 94 GHz (Gold et al. 2010), the AT20G catalog at 20 GHz (Murphy et al. 2010), and the GB6 (Gregory et al. 1996), PMN (Griffith et al. 1994, 1995; Wright et al. 1994, 1996) and S5 (Kuehr et al. 1981) catalogs at 5 GHz. To avoid false association of very faint low frequency sources with the ERCSC sources, we have applied a flux density cut of 150 mJy for both the 5 GHz catalogs (except for the S5 catalog which has a flux limit of 250 mJy) and the 20 GHz (only quality = 'g' sources are selected) catalog. No flux cut has been applied to the WMAP7 sources. Using a matching radius of half of the FWHM at each frequency, 94.5%, 91.8%, 88.1%, 64.7%, 55.8% of the ERCSC sources (at $|b| > 5°$) have been associated with one or multiple low frequency IDs in the 30, 44, 70, 100 and 143 GHz channels. Table 13 gives an example of the matching results. Using the Quick Detection System (Aatrokoski et al. 2009), variability information is also provided for 30, 44 and 70 GHz extragalactic sources (at $|b| > 10°$) that display a significant ($> 40\%$) change in their flux densities between multiple observations of the source by *Planck*. These multiple observations might either be a result of the 1.6 sky coverages or due to a source being observed at different times by the different *Planck* horns.

At higher frequencies, associations are practically impossible due to the difference in wavelength coverage between *Planck* and *IRAS* or *Akari*. For this reason, the notes files at 217, 353 and 545 GHz are empty. At 857 GHz, associations between ERCSC sources and the Imperial-IRAS Faint Source Catalog (Wang & Rowan-Robinson 2010) as well as bright galaxies in the NASA Extragalactic Database are presented. The notes are a continuously evolving document and have thus far been on a best effort basis. Cross-identifications are not guaranteed but have been incorporated to help the user. They will be updated as further analysis work is done and additional information is made available.

10.5. Color Corrections

The LFI maps are calibrated such that extracted sources have the correct flux density if they have a spectrum identical to that of the CMB. The HFI maps on the other hand are calibrated to have the correct flux density values for the spectral convention νI_ν =constant. Table 14 provides the multiplicative color corrections that should be applied to the ERCSC flux densities for sources of other spectral indices, to get the true flux density. That is, the true source flux density is equal to the ERCSC flux density multiplied by the color correction from Table 14. The spectral index α is defined such that the flux density $S_\nu \propto \nu^\alpha$. Naturally, the multiplicative color correction factor in the table is exactly unity if the spectral index is the same as the calibrator spectrum at that frequency i.e. 2 for the LFI bands and -1 for the HFI bands. The derivation of the color corrections is described in Zacchei et al. (2011); Planck HFI Core Team (2011b).

Table 13. Example of Notes for ERCSC 30 GHz Sources

Source Name	Notes
PLCKERC030 G000.70-42.83	Associated with WMAP J2109-4111 and AT20G J210933-411020.
PLCKERC030 G001.39+45.98	Associated with WMAP J1516+0014 and GB6 J1516+0015.
PLCKERC030 G001.55-28.97	Associated with WMAP J1958-3845 and AT20G J195759-384506.
PLCKERC030 G002.17+65.96	Associated with WMAP J1415+1324 and GB6 J1415+1320.
PLCKERC030 G003.62+80.50	Associated with WMAP J1327+2210 and GB6 J1327+2210.
PLCKERC030 G004.48-62.06	Associated with WMAP J2247-3700 and AT20G J224703-365746.
PLCKERC030 G004.51+06.86	Associated with PMN J1729-2235.
PLCKERC030 G005.33-40.24	Associated with AT20G J205741-373402.
PLCKERC030 G006.87+43.23	Associated with WMAP J1534+0127 and GB6 J1534+0131.
PLCKERC030 G008.85+73.07	Associated with WMAP J1356+1919 and GB6 J1357+1919.
PLCKERC030 G009.31-19.57	Associated with WMAP J1924-2914 and AT20G J192451-291430.
PLCKERC030 G009.66-32.92	Associated with AT20G J202435-325335.
PLCKERC030 G010.83+40.87	Associated with WMAP J1549+0236 and GB6 J1549+0237.
PLCKERC030 G011.37+54.57	Associated with WMAP J1504+1030 and GB6 J1504+1029.
PLCKERC030 G012.05+10.84	Associated with PMN J1733-1304.

Table 14. Color Corrections

Frequency	Spectral Index							
[GHz]	-2.0	-1.0	0.0	1.0	2.0	3.0	4.0	5.0
30	0.927	0.953	0.975	0.990	1.000	1.003	1.000	...
44	0.962	0.977	0.988	0.996	1.000	1.001	0.998	...
70	0.935	0.961	0.979	0.993	0.999	0.999	0.993	...
100	0.994	1.000	0.997	0.985	0.963	0.932	0.892	0.842
143	0.978	1.000	1.013	1.016	1.009	0.991	0.962	0.922
217	1.005	1.000	0.986	0.964	0.934	0.896	0.851	0.801
353	1.012	1.000	0.981	0.956	0.924	0.887	0.845	0.799
545	1.001	1.000	0.989	0.968	0.939	0.903	0.861	0.814
857	0.985	1.000	1.005	1.000	0.986	0.965	0.936	0.901

11. The *Planck* Early Cold Cores Catalog

11.1. Introduction

The *Planck* Early Cold Cores Catalog (ECC) provides a list of Galactic cold cores, i.e., compact cloud cores with color temperatures below 14 K. These can be either pre-stellar objects before or at the very initial stages of the protostellar collapse, or possibly more evolved sources that still contain significant amount of cold dust. Pre-stellar cloud cores represent the transition from turbulence-dominated large scales to the gravitation-dominated protostellar scales and are therefore a crucial step in the process of star formation. Imprinted in their structure and statistics is information on the properties of the parental clouds and the core formation processes where interstellar turbulence, magnetic field, self-gravity, and external triggering all play a role. The initial conditions in these cold molecular cloud cores directly affect the most fundamental aspects of star formation such as the stellar mass function, the star-formation efficiencies and time scales.

The shortest wavelength channels of *Planck* are at 350, 550, and 850 μm. These cover the wavelengths around and longward of the intensity maximum of the cold dust emission: $\nu^2 B_\nu(T = 10\mathrm{K})$ peaks close to 300 μm while, with a temperature of $T \sim 6$ K, the coldest dust inside the cores has its maximum close to 500 μm. Therefore, *Planck* data, when combined with far-infrared data from the IRAS survey, enable accurate determination of both the dust temperatures and its spectral index.

11.2. Source Detection

In order to detect the cold cores, we apply the Warm Background Subtraction Method, part of the CoCoCoDet algorithm described in Montier et al. (2010) and *Planck* Collaboration (2011s), on the maps at IRIS 100 microns, *Planck* 857 GHz, 545 GHz and 353 GHz. The spectrum of the background due to the diffuse ISM is computed over a disk with a $15'$ outer radius. This is assumed to be a warm background, uncontaminated by other cold cores. The initial catalog contains sources detected at SNR ≥ 4 by applying the background removal technique to the three highest frequency *Planck* bands using the IRIS 100 μm map as the "warm" component. The band-merging process positionally matches objects in the 353 GHz detection list, which contains the least number of entries, against both the 545 and 857 GHz catalogs using a $5'$ matching radius. Sources detected in only one or two bands are discarded. The SNR and position of the detection with the greatest SNR are assigned to the band-merged entry. As a final step, planetary masks defined in the *Planck* 353, 545, and 857 GHz bands are applied to the catalog to remove sources that are artifacts caused

by these very bright sources.

Aperture photometry is performed on the IRIS 100 micron and *Planck* 353, 545, and 857 GHz maps using an aperture radius of 5′ and a background annulus with radii spanning from 5 to 10′. An aperture correction of 1.0909 is applied, assuming that the effective beam FWHM is 5′ in all four bands. The flux densities and flux density errors generated by the four-band aperture photometry are used in an unconstrained three-parameter (T, β, and S_{857GHz}) greybody fit. The fitted temperatures are used in the source selection process described below.

11.3. ECC Monte Carlo Quality Assessment

The ECC Monte Carlo QA system addresses the ability of the ECC detection method to detect cold grey objects, characterized by the flux density at 857 GHz, temperature, and emissivity index (β). A total of 3500 Sources are injected into the IRIS 100 micron and the *Planck* 353, 545, and 857 GHz maps in each of four Monte Carlo realizations with the following parameters:

1. 8 K < T < 20 K [uniform distribution]
2. The emissivity index is computed following the T-β relation deduced from Archeops-detected cold sources: $\beta = 11.5T^{-0.66}$ (Desert et al. 2008)
3. 1 Jy < S_{857GHz} < 100 Jy [uniform distribution in log_{10}S]
4. uniform distribution across the entire sky

We assess the ability of the detection method to accurately recover the flux densities of the injected sources based on both the SNR and the estimated temperature. The reliability of a source detection is assessed using a combination of astrometric and photometric criteria, specifically, that the detected source be within 5 arcmin of an injected false source and that the flux densities at 353, 545, and 857 GHz are recovered to within 30%. The 30% requirement for the flux density accuracy is motivated by a similar analysis performed for the ERCSC which is described in Section 7.1.

Figure 19 shows the photometric accuracy, defined as the relative difference of the detected flux density to the injected flux density, against the detection SNR. On these plots the ±30% photometric error limits used in defining reliability are marked along with the ECC SNR ≥ 15 threshold. Figure 20 presents the photometric accuracy plotted against the

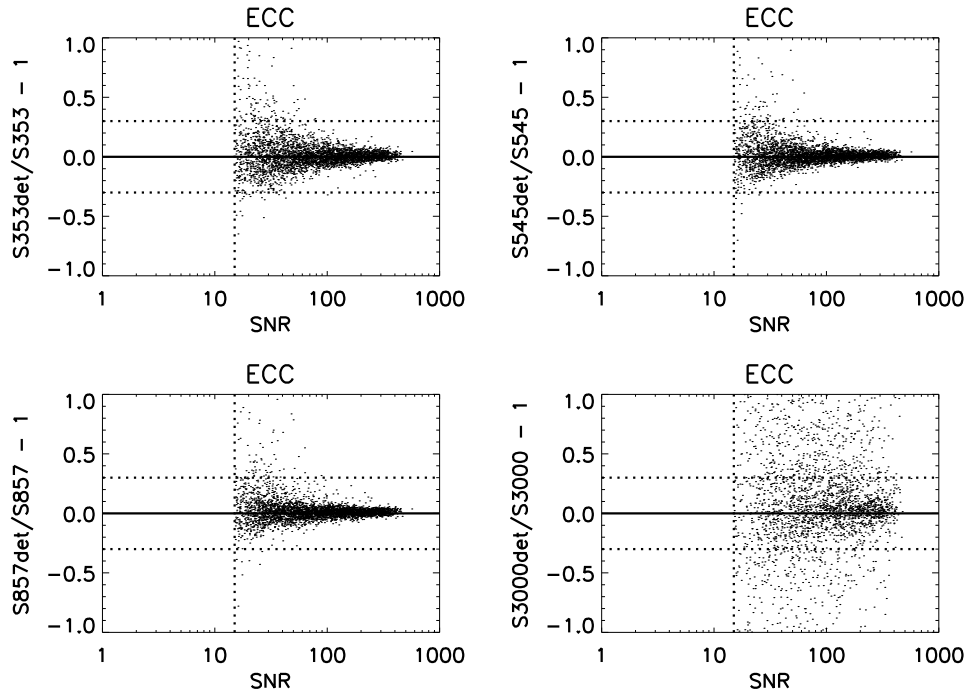

Fig. 19.— The photometric accuracy for Monte Carlo injected false sources are shown here against the reported SNR of detection for the *Planck* 353, 545, and 857 GHz bands and in the IRIS 100 micron (3000 GHz) maps. The vertical line marks the SNR=15 threshold used in creation of the ECC. The dotted horizontal lines trace the ±30% photometric accuracy limits used in assessment of reliability.

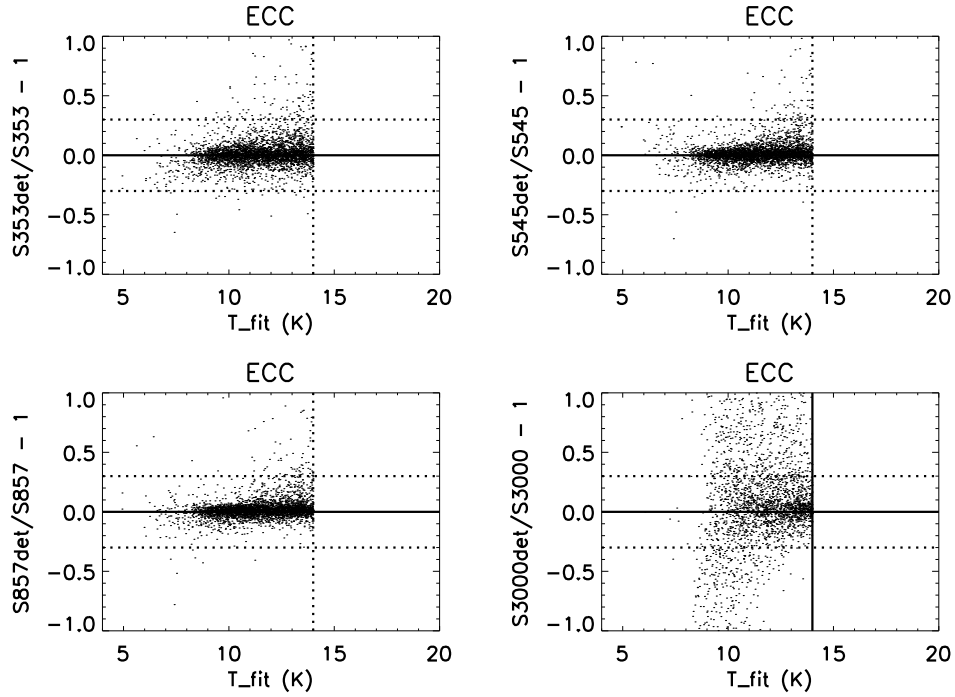

Fig. 20.— The photometric accuracy for Monte Carlo injected false sources are shown here against the fitted greybody temperature. The vertical line marks the T = 14 K threshold used in creation of the ECC.

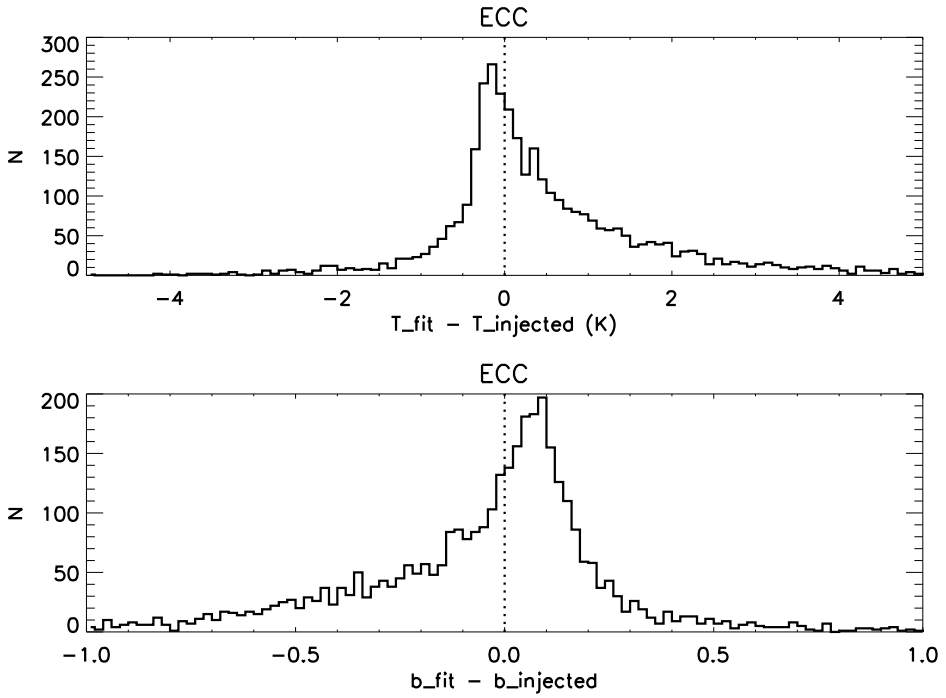

Fig. 21.— These plots show the recovery of the greybody (T,β) parameters for Monte Carlo injected false sources as difference histograms.

fitted greybody temperature, where the vertical line marks the ECC T $\leq$ 14 K limit. We also check how well the greybody fits recovered the temperature and emissivity indices of the injected sources - this information is shown in Figure 21.

The ECC reliability as a function of SNR and fitted temperature is summarized in Figure 22. The detection algorithm is sensitive to both the SNR and temperature, especially for sources whose temperatures are closer to the warm diffuse emission and hence are difficult to separate from the background.

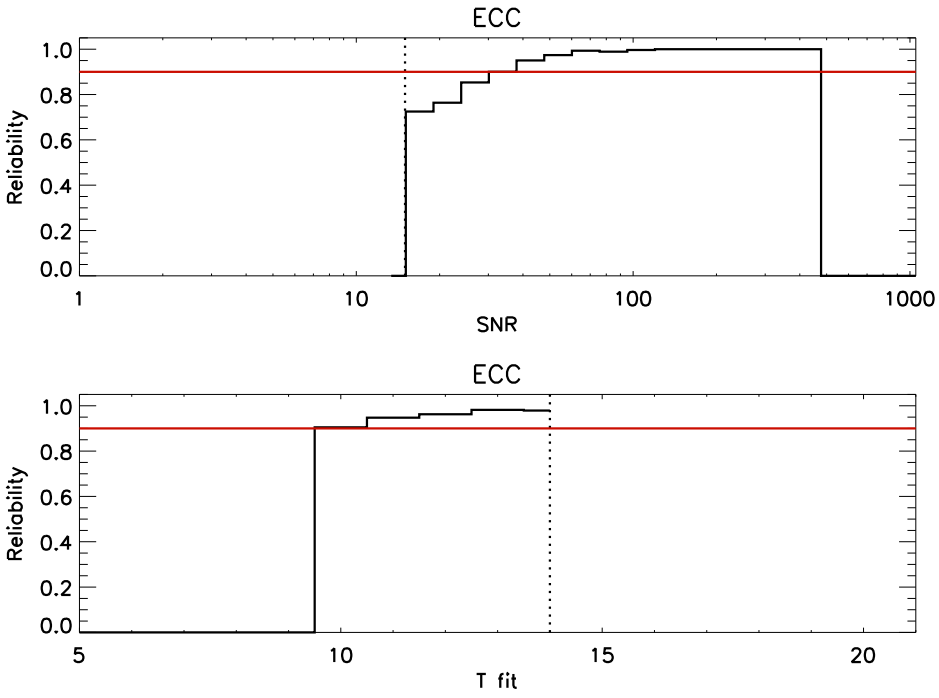

Fig. 22.— Here we present the Monte Carlo QA based reliability after application of the SNR $\geq$ 15 and T $\leq$ 14 K selection criteria employed in the delivered ECC. The reliability is computed for bins in SNR (*top*) and in the temperature inferred from the greybody fit (*bottom*). In both plots the vertical lines indicate the SNR and temperature thresholds and the horizontal line marks the 90% reliability level for reference.

11.4. Delivered ECC

11.4.1. Catalog Contents

The delivered catalog consists of the 915 objects meeting the ECC selection criteria of SNR $\geq$ 15 and T $\leq$ 14 K, after removal of sources with obviously discrepant SEDs or are positionally matched to bright AGNs, e.g. 3C 273.

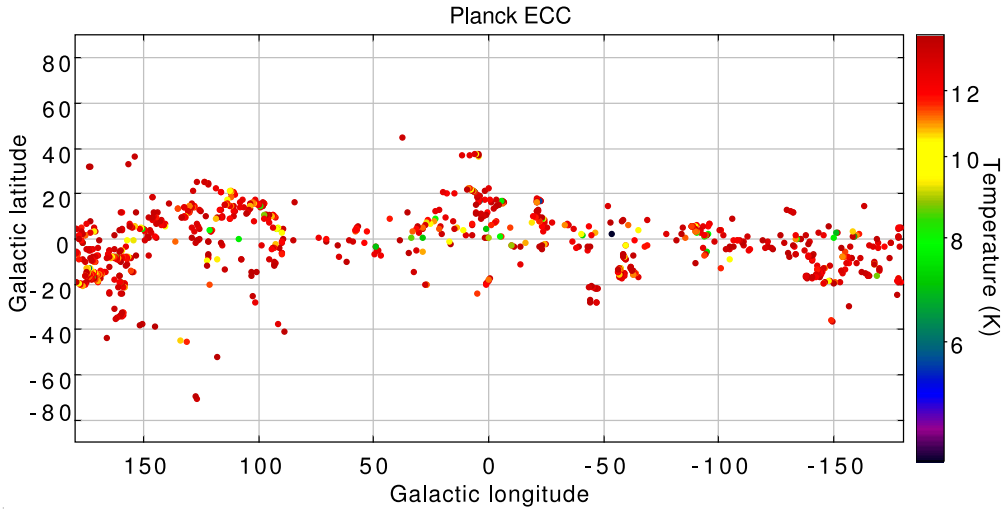

Fig. 23.— ECC detections having SNR $\geq$ 15 and T $\leq$ 14 K presented on a rectangular all-sky map. The symbols are color-coded by temperature using the scale shown on the right.

11.4.2. Catalog Format

The *Planck* ECC is delivered as a FITS binary table. The primary header and extension contents are described in Tables 15 and 16. The data columns contained within the extension cover identification, source position, source detection, and source characterization.

Table 15. ECC FITS Binary Table Primary Header

FITS Keyword	Description
INSTRUM	HFI
VERSION	Version of the ECC
DATE	Date file created: yyyy-mm-dd
ORIGIN	Organizations responsible for the data (*Planck* Working Group 7 and U.S. *Planck* Data Center)
TELESCOPE	PLANCK
CREATOR	P4.2 Pipeline
DATE-OBS	Start-up time of the survey: yyyy-mm-dd
DATE-END	Ending time of the survey: yyyy-mm-dd

Table 16. ECC FITS Binary Table Extension Contents

Column Name	Description
	Identification
NAME	Source name[1]
SNR	Signal to Noise ratio of detection
	Source Position
GLON	Galactic longitude based on bandmerge algorithm
GLAT	Galactic latitude based on bandmerge algorithm
RA	Right ascension (J2000)
DEC	Declination (J2000)
	Source Detection
APFLUX353	Aperture flux density at 353 GHz (mJy)
APFLUX545	Aperture flux density at 545 GHz (mJy)
APFLUX857	Aperture flux density at 857 GHz (mJy)
APFLUX3000	Aperture flux density at 3000 GHz (mJy)
APFLUX353_ERR	Uncertainty (1 sigma) in APFLUX353 (mJy)
APFLUX545_ERR	Uncertainty (1 sigma) in APFLUX545 (mJy)
APFLUX857_ERR	Uncertainty (1 sigma) in APFLUX857 (mJy)
APFLUX3000_ERR	Uncertainty (1 sigma) in APFLUX3000 (mJy)
	Source Characterization
TEMPERATURE	Temperature from greybody fit (K)
BETA	Emissivity index from greybody fit
S857	Flux density at 857 GHz from greybody fit (mJy)
TEMPERATURE_ERR	Uncertainty (1 sigma) in TEMPERATURE (K)
BETA_ERR	Uncertainty (1 sigma) in BETA
S857_ERR	Uncertainty (1 sigma) in S857
BESTNORM	Summed squared residuals for best fit (mJy^2)
	Detailed Source Characterization
TEMPERATURE_CORE	Core T from greybody fit on cold residual (K)
BETA_CORE	Emissivity index from greybody fit on cold residual
MAJ_AXIS_FWHM_CORE	Ellipse major axis of cold residual extent (arcmin)
MIN_AXIS_FWHM_CORE	Ellipse minor axis of cold residual extent (arcmin)
TEMPERATURE_CORE_ERR	Uncertainty (1 sigma) TEMPERATURE_CORE (K)
BETA_CORE_ERR	Uncertainty (1 sigma) BETA_CORE
MAJ_AXIS_FWHM_CORE_ERR	Uncertainty (1 sigma) MAJ_AXIS_FWHM_CORE (arcmin)
MIN_AXIS_FWHM_CORE_ERR	Uncertainty (1 sigma) MIN_AXIS_FWHM_CORE (arcmin)

[1]Source name designations consist of a prefix and a positional qualifier, which is in Galactic coordinates and specified as "Glll.ll+bb.bb" where the (l,b) values are truncated. The prefix used in the ECC portion of the ERCSC is PLCKECC - Planck ECC catalog.

11.5. Postage Stamps and Skymaps

11.5.1. Postage Stamps

The postage stamps created for the ECC display the same source at three frequencies: 353, 545, and 857 GHz, and are from the CMB-subtracted intensity maps.

The attributes of these postage stamps are:

1. Image size 4*FWHM square, aligned with galactic North up
2. Color scale chosen independently for each image
3. Sources listed in ascending order of Galactic longitudes

These are delivered in two separate formats:

1. Separate JPEG files for each image, for use in online archives.
2. PDF files with many images per page, labeled with location (galactic coordinates) and flux density of source in mJy.

11.5.2. Skymaps

The spatial distribution of the sources included in the ECC is shown in Figure 23. The cold core candidate positions are indicated by dots, color-coded by estimated temperature (TEMPERATURE). The ECC sources are mainly distributed in the Galactic plane, having a median value of $|b|$ of 9.7°. Only 38 sources (4.2%) are at high Galactic latitude ($|b| \geq 30°$).

11.6. Notes on the Catalog

11.6.1. Sources with Negative 100 μm Flux Densities

A small fraction (23/915) of sources have negative flux densities measured from the IRIS 100 μm maps. This is an expected consequence of performing aperture photometry on very cold sources having negligible emission relative to the warmer ambient dust at short wavelengths. In Figure 24 it is evident that these form part of the general trend for sources having fitted temperatures less than 10 K to also have very low ratios of 3000 GHz to 857 GHz flux densities.

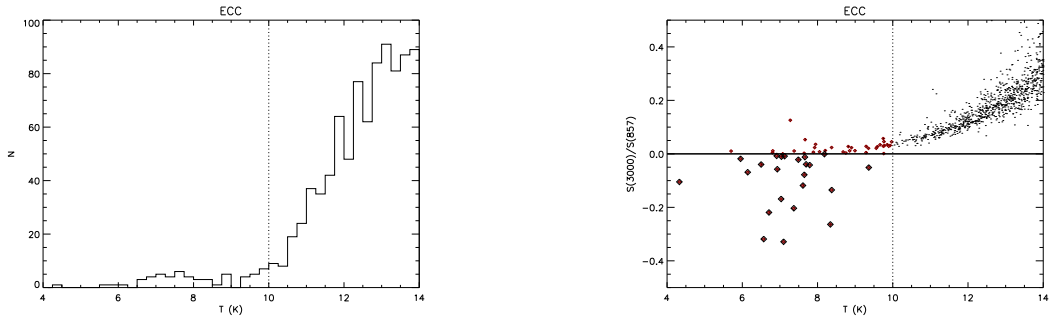

Fig. 24.— ECC detections having T $\leq$ 10 K are highlighted in the histogram of fitted temperatures (*left*) and on a plot of the 3000 GHz to 857 GHz flux density ratio against temperature (*right*). In the latter, sources with negative 3000 GHz aperture fluxes are marked by black diamonds.

11.6.2. Contents of the ECC Notes File

Comments concerning the individual ECC sources are supplied in electronically available notes, formatted as a two-column comma separated value file. The issues addressed with these annotations are:

- Inclusion in the ERCSC 353, 545, or 857 GHz single-band detection based catalogs,
- Astrometric cross-matches with far-IR sources (IRAS Point Source Catalog),
- Astrometric cross-matches with known infrared dark clouds (IRDCs),
- Astrometric cross-matches with extragalactic objects listed in the SIMBAD and NED catalogs,
- Lack of astrometric cross-match with any entry in SIMBAD,
- The quoted TEMPERATURE_CORE value being a probable upper limit,
- Failure of the Gaussian fit procedure responsible for production of the "CORE" columns

In all cases the matching radius used is 5 arcminutes.

A portion of the ECC notes files is reproduced here, as guidance for form and content.

```
PLCKECC G001.38+20.94, Detected at 857, 545 and 353 GHz in the ERCSC.
PLCKECC G001.64-00.07, Associated with IRDC G001.62-00.08.
```

```
                     Quoted core temperature is an upper limit.
                     Gaussian fit failed, circular aperture forced.
PLCKECC G001.84+16.58, Detected at 857, 545 and 353 GHz in the ERCSC.
PLCKECC G001.95+09.78, Detected at 857, 545 and 353 GHz in the ERCSC.
                     Gaussian fit failed, circular aperture forced.
PLCKECC G003.07+09.95, Detected at 857, 545 and 353 GHz in the ERCSC.
PLCKECC G003.14+08.19, Detected at 857, 545 and 353 GHz in the ERCSC.
PLCKECC G003.27+10.42, Associated with IRAS 17119-2027.
                     Detected at 857, 545 and 353 GHz in the ERCSC.
                     Possible extragalactic object.
```

12. The *Planck* Early Sunyaev-Zel'dovich Detected Cluster Candidates

12.1. Introduction

The *Planck* Early Sunyaev-Zel'dovich (ESZ) cluster sample is a list of SZ cluster candidates which are detected by their multi-frequency signature through the *Planck* bands. The thermal SZ effect is the result of CMB photons inverse Compton scattering off energetic electrons in the hot intra-cluster medium. The net result is a distortion in the shape of the CMB spectrum which results in a deficit of flux density below ∼220 GHz and an increment in flux density at higher frequencies (Sunyaev & Zel'dovich 1972; Carlstrom et al. 2002). By utilizing a matched multi-frequency filter, the spectral signature of this distortion can be detected and measured in the *Planck* all sky maps, which enables cluster candidates to be detected.

The ESZ sample generated as part of the *Planck* early data release is the result of a blind multi-frequency search in the all sky maps, i.e., no prior positional information on clusters detected in any existing catalogues was fed as input to the detection algorithm. In practice, the ESZ sample is produced using one of the four matched multi-frequency filter (MMF) algorithms available within the *Planck* Collaboration (hereafter MMF3; see Melin et al. (2010) for details of the comparison of the cluster extraction algorithms). MMF3 is an all-sky extension of the algorithm described in Melin et al. (2006) and is run blindly over the six HFI frequency maps. The technique first divides the all-sky maps into a set of overlapping square patches. The matched multi-frequency filter then combines optimally the six frequencies of each patch assuming the SZ frequency spectrum and using the Arnaud et al. (2010) pressure profile as the cluster profile. Auto- and cross- power spectra used by the MMF are directly estimated from the data. They are thus adapted to the local instrumental noise and astrophysical contamination. For each patch, the scale radius of the cluster profile is varied to maximize the signal-to-noise ratio of each detection. The algorithm thus assigns to each detected source an estimated size and an integrated flux. The detected sources extracted from individual patches are finally merged into an all-sky cluster list. Non-SZ sources captured by the MMF algorithm can contaminate the list and an additional step of validation of the detection is needed (see next section).

Unlike the individual frequency source lists or the ECC list which are validated through a Monte-Carlo technique, the reliability of the ESZ list has been estimated through a validation process based on internal checks and on cross-checks with ancillary optical/near-infrared and X-ray cluster catalogs or data.

12.2. The Generation of the ESZ List

This section describes the steps associated with generation of the ESZ list.

Although the spectral distortion of the CMB due to the intra-cluster medium can in principle be detected down to the lowest frequencies at which *Planck* operates, the beam at the lowest frequencies is large compared to typical cluster sizes. Since clusters at moderate redshifts typically span angular scales of $\sim 5'$, the large beam of *Planck* at the LFI bands results in beam dilution of the SZ signal. The inclusion of the lowest *Planck* frequencies using the current algorithm therefore results in a lower signal to noise for the detected sources than if only the HFI bands are used. This reduces the efficiency of SZ cluster detection which can potentially be improved in the future with refinements to the algorithm. As a consequence, for the generation of the ESZ list, only the *Planck* all sky maps at frequencies of 100 GHz and above were considered.

For the spatial filtering, the beam values estimated from observations of planets were adopted (Table 1). It is noted that these are not the effective beams in the maps which vary as a function of spatial location on the sky. This variation has been estimated to lead to $\sim 10 - 20\%$ differences in the flux density estimates of the high signal to noise SZ clusters presented here.

A first pass of the algorithm on the *Planck* maps at $|b| > 14^\circ$ resulted in a total of 945 SZ candidates being detected in a blind search, with signal-to-noise ratio SNR≥ 4. As discussed above, the MMF algorithm uses prior information on the SZ spectrum and on the cluster shape. However, in the case of beamsizes of the order of a few arcminutes, the resulting list of SZ candidates contains false detections due mainly to dust emission at high frequencies from the interstellar medium (ISM) or infrared sources, and to a lesser extent from CMB fluctuations at low frequencies. The latitude cut used above is chosen to minimize contamination from the ISM. We do not explicitly check for associations with extragalactic sources emitting at HFI frequencies. As a result, some residual contamination of the SZ Compton-Y parameter by point sources may still be present and is noted for individual sources in the notes.

The validation process on this sample was then initiated. A full description of the validation process can be found in *Planck* Collaboration (2011d). First the candidates showing rising spectral energy distribution in the highest HFI frequency bands were rejected. They represent $\sim$14% of the initial number of blind SZ candidates. Second, the remaining sample was further cleaned by rejecting all objects associated with either Galactic sources, or cold cores within a $7'$ radius of the SZ candidates. This step further reduces the SZ candidate sample by about 17%.

After this two-step process, the initial blind SZ candidate sample is reduced by about 27% and we are left with around 770 SZ candidates with SNR$\geq$ 4. To ensure high reliability of the ESZ we then apply a signal-to-noise cut of SNR $\geq$ 6 which retains 201 SZ candidates. Finally, only the SZ candidates detected blindly by the MMF3 algorithm and at least one other cluster detection algorithm, be it MMF1 or PowellSnakes (see *Planck* Collaboration 2011d for details) are classified as "robust". This results in 190 SZ cluster candidates which constitute the baseline ESZ sample. A final internal check was performed which consisted of searching for associations of the 190 SZ candidates with possible artefacts such as low-frequency noise stripes, ringing from neighbouring bright sources, hot pixels, non-observed pixels or poorly sampled pixels in the vicinity of solar system objects. None of the 190 ESZ candidates was associated with such artefacts.

A detailed inspection of the 190 cluster candidates was undertaken through a combination of cross-matching with known cluster catalogs, searches of data archives and follow-up with other observational facilities.

- *Associations in X-ray cluster catalogues:* The ESZ candidates were matched to the Meta-Catalogue of X-ray detected Clusters of galaxies (Piffaretti et al. 2010; MCXC hereafter), and an extented version of the MCXC detailed in *Planck* Collaboration (2011e). The MCXC consists of $\sim$1800 clusters from publicly available ROSAT All Sky Survey-based (NORAS, REFLEX, BCS, SGP, NEP, MACS, and CIZA) and serendipitous (160SD, 400SD, SHARC, WARPS, EMSS, etc) cluster catalogues. For each known X-ray cluster, several entries are available among which the identifiers, redshift, coordinates, total mass M_{500}, and radius R_{500} were used during the external validation process. R_{500} is the radius that encompasses a mean matter density which is 500 times the critical density at the corresponding redshift. R_{500} is less than the virial radius of the cluster. M_{500} is the mass within R_{500}.

- *Associations in optically-selected cluster catalogues:* The ESZ candidates were matched to the Abell cluster catalogue (5250 clusters of which 1026 have a redshift) and the Zwicky cluster catalogue (9134 objects). The association criterion here required a positional match within a search radius for both catalogues set to $10'$. Furthermore, the ESZ sample was cross-checked against MaxBCG and the Sloan cluster search (Wen et al. 2009) with a search radius of $5'$.

- *Associations with known SZ clusters:* The ESZ sample was matched to clusters identified through the SZ effect at millimeter wavelengths such as the newly discovered ACT and SPT clusters (Menanteau et al. 2010; Vanderlinde et al. 2010) as well as the sample of Douspis et al. (in preparation). Again the association was based on positional matching with a search radius of $5'$.

- *Other Searches:* Further searches in the Virtual Observatory, SIMBAD, NED and in logs of various observatories were performed. These are important since they indicate which clusters might already have ancillary observations available. The search in X-ray observatories (ROSAT, Suzaku, XMM-Newton and Chandra) was performed using the HEASARC tool[3]. For XMM-Newton and Chandra both master catalogues and accepted GO (Guest Observer) targets were used in the search. For Suzaku, only the master catalogue was used. In the case of optical and NIR observatories, the search was performed in the public logs of several optical/infrared observatories. In some case, this search was completed using some of the VO (Virtual Observatory) tools[4]. The checked resources were: ING Archive, UKIRT Archive, ESO Archive, HST Archive (at ESO), CFHT Archive, AAT Archive, NOAO Science Archive, Multimission Archive at STScI (MAST), Gemini Science Archive and SMOKA (Subaru Mitaka Okayama Kiso Archive). In addition, a search in the footprint of the covered area for known surveys was performed. The searched areas considered were those of SDSS, UKIDSS, HST (ACS-WFC) as they are described in the VO footprint service[5] , as well as those of SPT and ACT experiments.

A coherent follow-up programme targeted towards the verification/validation of the candidate clusters in the full SZ list was put in place. The main goals of this follow up programme are to confirm *Planck* candidates as new clusters, and as a consequence, to better handle both the SZ selection criteria in the *Planck* survey and the reliability of selected sources. An ensemble of SZ candidates spanning a range of SNR between 11 and 4 was selected for follow-up. The primary follow-up effort involved the use of XMM-*Newton* Director's Discretionary Time (*Planck* Collaboration 2011e). A total of 25 targets were observed for short snapshot exposures (i.e., 10 ks nominal exposure time) out of which 21 were confirmed as clusters or systems of multiple extended X-ray sources (i.e. double or triple). All the data are made public with the publication of the *Planck* early results. Of the 21 confirmed *Planck* SZ sources, 11 are found in the ESZ sample. The remaining 10 are discussed in *Planck* Collaboration (2011e). In addition, optical follow up with the European Northern Observatory facilities (ENO), cross correlation with overdensities of infrared galaxies in the WISE all sky survey (Wright et al. 2010) and observations with the Arcminute Microkelvin Imager (AMI) were undertaken.

169 of the 190 cluster candidates are associated with known X-ray or optical clusters

[3]http://heasarc.gsfc.nasa.gov/cgi-bin/W3Browse/w3browse.pl

[4]VO command line tools http://iraf-nvo.noao.edu/vo-cli/,

[5]http://www.voservices.net/footprint

and the *Planck* data provide the first measure of the SZ signature of the majority of them. 21 are candidate new clusters of which 12 have been confirmed (11 by XMM-*Newton* and 1 by AMI and WISE). There are 9 remaining candidate new clusters to be confirmed. One of them turned out to be a spurious detection and was rejected from the final ESZ list. One (*PLCKESZ G189.84−37.24*) was further inspected and found to have a high level of contamination and low reliability. It is still present in the ESZ list with caveats in the notes (Section 12.4). The final ESZ list thus includes 189 clusters and cluster candidates.

A full description of the validation effort is in the *Planck* early paper I (*Planck* Collaboration 2011d). Notes on individual sources are provided later in Section 12.4. Figure 25 shows the all sky distribution of the clusters and cluster candidates with the color coding by SNR.

12.3. Usage of the ESZ List

The full list of columns for the ESZ list is provided in Table 17. All clusters have a *Planck* name which is given in the column `NAME`. This name has a format PLCKESZ GXXX.XX±YY.YY, which is constructed from `GLON` and `GLAT`, the best estimated Galactic coordinates of the SZ signal. The *Planck* SZ cluster candidate positions are also given in equatorial coordinates in `RA` and `DEC`, while `SNR` gives the detection's signal-to-noise ratio as defined by the matched multi-filter method MMF3.

When a *Planck* SZ cluster candidate is identified as an X-ray cluster in the MCXC the coordinates of the X-ray counterpart (i.e., the X-ray centroid) is given in columns (`GLON_X`, `GLAT_X`) and (`RA_X`, `DEC_X`). The same positional information is given for the *Planck* cluster candidates confirmed by XMM-Newton observation (apart from one candidate identified with a double cluster, see notes below). For those clusters with an X-ray counterpart, the Compton-Y parameter, which is the integral of the Compton-y over the cluster area, is re-extracted from the *Planck* maps using the X-ray centroid coordinates and X-ray size `THETA_X` as priors, yielding the value `Y_PSX` and its error `Y_PSX_ERR`. The Compton-Y parameter measured using the X-ray position and size priors is known to be more robust than the blind value estimated without priors (*Planck* Collaboration 2011d).

For cluster candidates without available estimates of X-ray position or size, the derived SZ parameters `THETA`, `Y`, and the associated errors `THETA_ERR` and `Y_ERR` are the values returned directly by the matched filter. These are likely to be more uncertain than cases where the cluster has been confirmed in the X-ray data. `THETA` and `THETA_X` are the estimated angular size of the cluster at 5 times R_{500}.

For clusters identified at other wavelengths the most common name is given in the `ID` column.

If available, redshifts are provided in column `REDSHIFT` (see Figure 26). The redshifts are taken from the MCXC cluster compilation unless otherwise stated in the notes. Photometric redshifts are given to two decimal place, while spectroscopic redshifts are given to three decimal places, apart from those from the MCXC. Redshifts estimated for 9 of the 11 *Planck* cluster candidates confirmed by XMM-Newton observation are also included in the catalog. Details of those can be found in *Planck* Collaboration (2011e).

Figure 27 shows postage stamp cutouts of a representative sample of 12 clusters at the HFI frequencies. Cutouts of the cluster candidates in both the intensity maps as well as the component separated maps are shown. Clusters distinguish themselves by the presence of a CMB decrement (blue regions) at the center of the 100 and 143 GHz cutouts. The presence of a decrement in the raw intensity maps is hard to discern due to the contribution from Galactic foregrounds. The multifrequency capabilities of *Planck* enables a more precise subtraction of the foregrounds. Figure 28 shows the reconstructed Compton-y map for these 12 clusters from a spatially smoothed, weighted combination of the maps from the individual frequencies.

12.4. Notes on Individual Clusters

The `ID` column, implying an identification, is filled if the SZ source is associated with a known cluster. The `ID` could be one of the following:

- 'AXXXX': cluster from the Abell catalogue (Abell et al. 1989);
- 'RXC' or 'RX': cluster from the ROSAT X-ray survey;
- 'CIZA': cluster from the "Cluster in the Zone of avoidance" sample ;
- 'ACO': cluster from the Abell, Corwin and Olowin catalogue;
- 'RBS': cluster from the ROSAT Bright Source (RBS) catalogue ;
- 'MACS': cluster from the "MAssive Cluster Survey" (Ebeling et al. 2010)
- 'ZwCl': cluster fom the Zwicky catalogue (Zwicky et al. 1961).

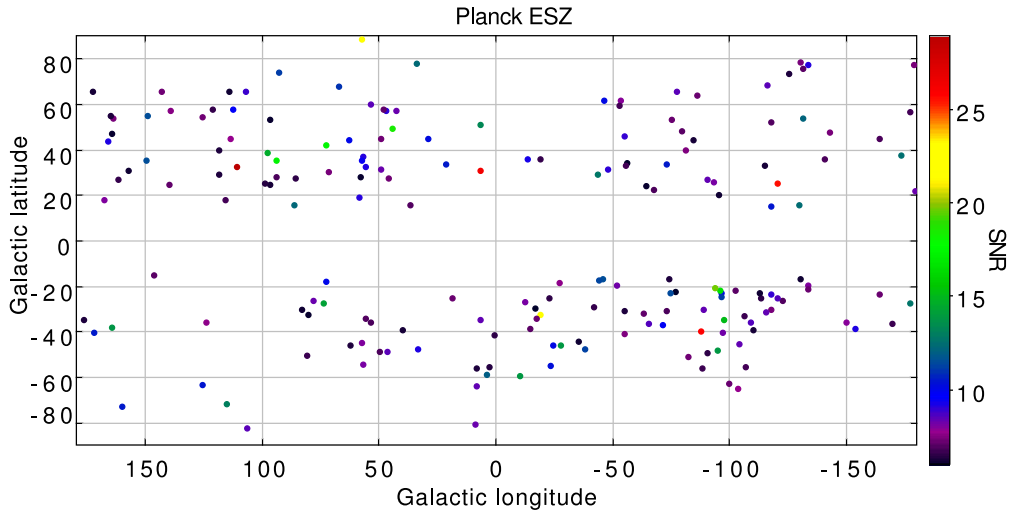

Fig. 25.— Plot showing the sky distribution of the ESZ cluster candidates. Sources close to the Galactic Plane have been excluded since the spurious fraction is high.

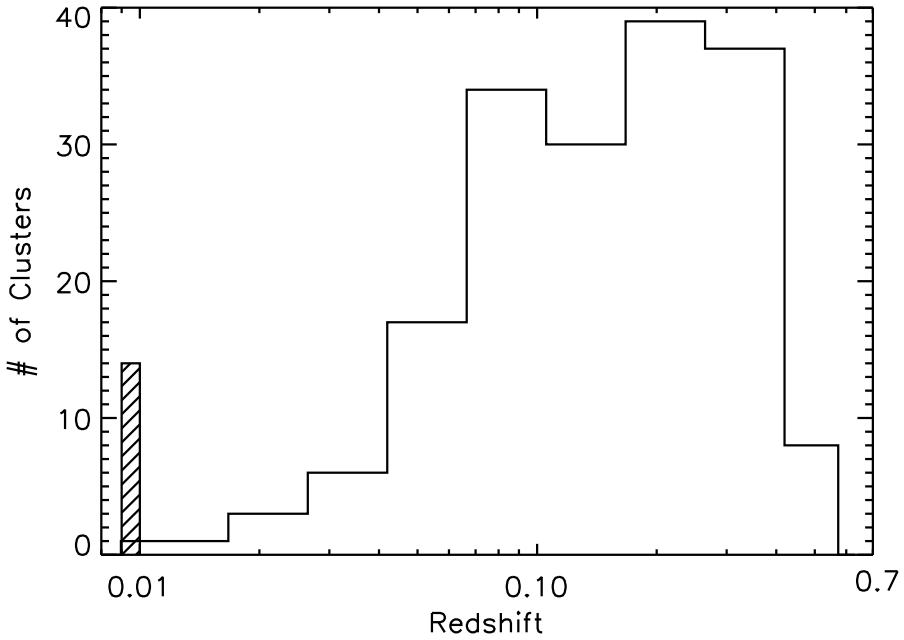

Fig. 26.— Redshift distribution of ESZ cluster candidates. ESZ clusters which do not have a redshift estimate are shown at an arbitrary redshift as the hatched region.

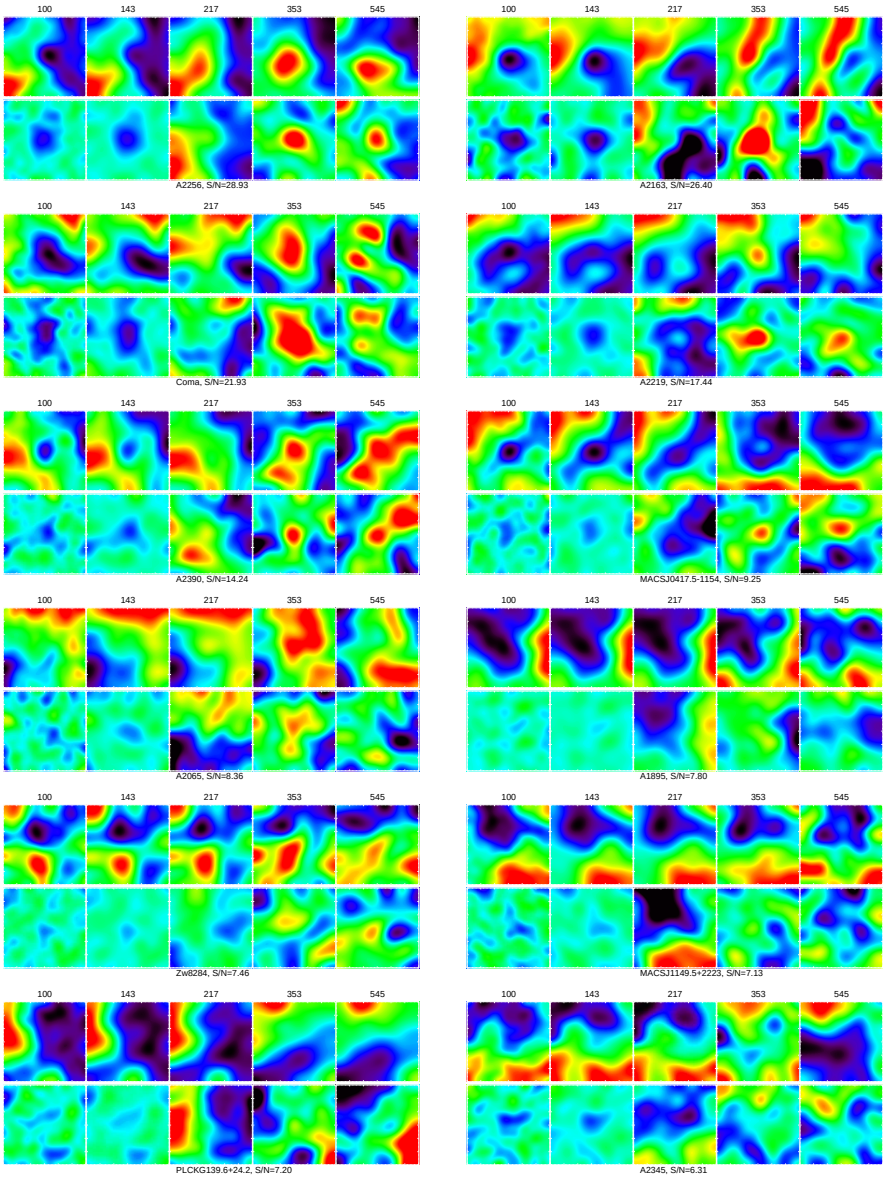

Fig. 27.— Multifrequency postage stamp of representative clusters from the ESZ sample. For each cluster, the upper panels show the raw (1 square degree) maps at 100, 143, 217, 353, and 545GHz. The lower panels show the corresponding "cleaned" maps (see *Planck* Collaboration 2011d). These clusters span SNR values from 29 to 6, from the upper left to the lower right The color scale in each cutout ranges from blue for low intensity to red for high intensities.

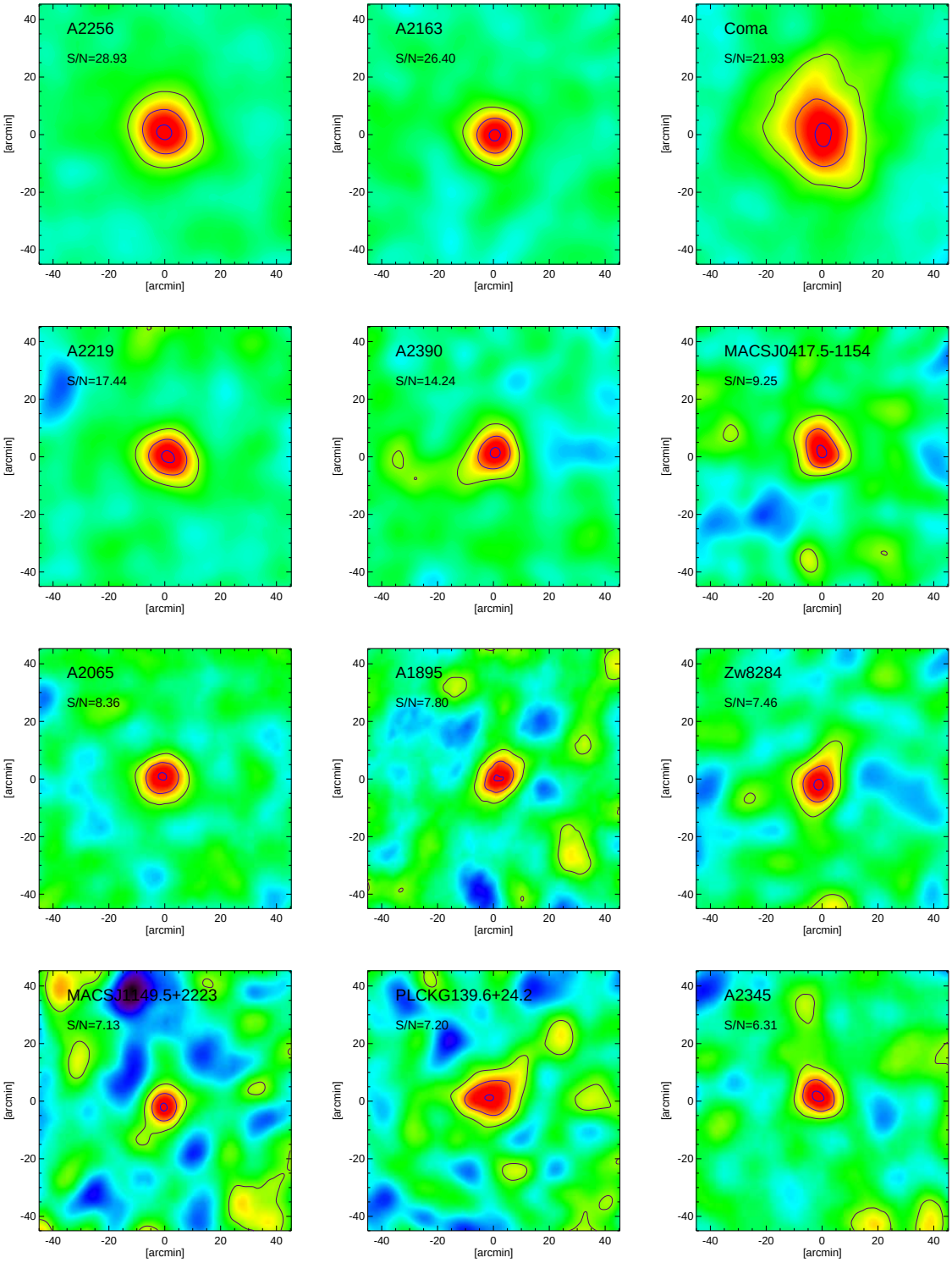

Fig. 28.— Illustrations of reconstructed Compton-y maps (1.5 deg $\times$1.5 deg, smoothed to 13′) for 12 clusters spanning SNR values from 29 to 6, from the upper left to the lower right.

Notes on individual clusters follow. An electronic version of these notes is integrated into the *Planck* archive. Unlike for the ECC and the ERCSC where the notes are far more numerous, the full listing of ESZ notes is provided here.

PLCKESZ G008.30−64.75 : X−ray source in the field. Redshift ($z = 0.3148$) quoted in Abell et al. (1989) and in Martini et al. (2007).

PLCKESZ G049.20+30.86 : In ERCSC at 545 and 857 GHz. Possible contamination could affect Y estimate.

PLCKESZ G053.44−36.26 : In ERCSC at 545 GHz. Possible contamination by source emission could affect Y estimate. Redshift ($z = 0.325$) quoted in Smail et al. (2007).

PLCKESZ G055.97−34.88 : Possible contamination by dust emission could affect Y estimate.

PLCKESZ G062.42−46.41 : Possible contamination by dust emission could affect Y estimate.

PLCKESZ G072.80−18.72 : X−ray source in the field. Redshift ($z = 0.143$) quoted in Allen et al. (1992).

PLCKESZ G085.99+26.71 : Possible contamination by dust emission could affect Y estimate. Redshift ($z = 0.179$) quoted in David et al. (1999).

PLCKESZ G086.45+15.29 : In ERCSC at 353 GHz.

PLCKESZ G094.01+27.42 : Redshift ($z = 0.299$) quoted in Schneider et al. (1992).

PLCKESZ G096.87+24.21 : X−ray source in the field. Possible contamination by source emission could affect Y estimate. No redshift quoted.

PLCKESZ G097.73+38.11 : In ERCSC at 353 GHz.

PLCKESZ G115.71+17.52 : Candidate new cluster. BSC−RASS source in the field. Possible contamination by dust emission could affect Y estimate.

PLCKESZ G121.11+57.01 : Candidate new cluster. FSC/BSC−RASS source in the field. Possible association with WHL J125933.4+600409 with redshift ($z = 0.33$) from Wen et al. (2009).

PLCKESZ G125.58−64.14 : In ERCSC at 30 GHz.

PLCKESZ G139.59+24.18 : Candidate new cluster confirmed by AMI observations and possibly confirmed by WISE. Details can be found in Planck Collaboration (2011e).

PLCKESZ G157.43+30.33 : Identification from SIMBAD. Cluster quoted in Appenzeller et al. (1998).

PLCKESZ G164.61+46.38 : X−ray source in the field. Possible contamination by source emission could affect Y estimate. No redshift quoted.

PLCKESZ G171.94−40.65 : Candidate new cluster confirmed by XMM−Newton observations. Details, including redshift estimate, can be found in Planck Collaboration (2011e).

PLCKESZ G189.84−37.24 : Candidate new cluster but with low reliability. No X−ray source in the field. High level of contamination by Galactic emission.

PLCKESZ G225.92−19.99 : Candidate new cluster. BSC−RASS and FSC−RASS sources in the field. In XMM-Newton and HST observation logs.

PLCKESZ G228.49+53.12 : Possible contamination by source emission could affect Y estimate. NVSS source in the field with 0.133 Jy emitting up to 100 GHz.

PLCKESZ G239.28−25.99 : Redshift ($z = 0.407$) quoted in Cavagnolo et al. (2008).

PLCKESZ G241.85+51.53 : Possible contamination by source emission could affect Y estimate. NVSS source with 0.159 Jy flux density in the field emitting up to 143 GHz.

PLCKESZ G246.52−26.05 : In ERCSC at 30 GHz.

PLCKESZ G250.90−36.25 : Possible contamination by dust emission could affect Y estimate.

PLCKESZ G255.62−46.16 : Candidate new cluster. FSC−RASS source in the field. In ESO and Suzaku observation logs.

PLCKESZ G262.25−35.36 : In ERCSC at 353 GHz.

PLCKESZ G262.71−40.91 : Candidate new cluster confirmed by XMM−Newton observations. Details, including redshift estimate, can be found in Planck Collaboration (2011e). Also ACT cluster with redshift ($z = 0.54$) quoted in Menanteau et al. (2010).

PLCKESZ G264.41+19.48 : Candidate new cluster. BSC−RASS source in the field.

PLCKESZ G266.03−21.25 : In ERCSC at 353 GHz.

PLCKESZ G269.51+26.42 : Possible contamination by source emission could affect Y estimate.

PLCKESZ G271.19−30.96 : Candidate new cluster confirmed by XMM−Newton observations. Details, including redshift estimate, can be found in Planck Collaboration (2011e).

PLCKESZ G271.50−56.55 : Redshift ($z = 0.3$) quoted in Edge et al. (1994).

PLCKESZ G275.21+43.92 : Possible contamination by source emission could affect Y estimate. NVSS source with flux density of 1.32 Jy in the field emitting in all LFI and HFI channels.

PLCKESZ G277.75−51.73 : Candidate new cluster confirmed by XMM−Newton observations. Details, including redshift estimate, can be found in Planck Collaboration (2011e).

PLCKESZ G283.16−22.93 : Candidate new cluster. FSC−RASS source in the field.

PLCKESZ G284.99−23.70 : Candidate new cluster confirmed by XMM−Newton observations. Details, including redshift estimate, can be found in Planck Collaboration (2011e).

PLCKESZ G285.63−17.24 : Candidate new cluster confirmed by XMM−Newton observations. Details, including redshift estimate, can be found in Planck Collaboration (2011e).

PLCKESZ G286.58−31.25 : Candidate new cluster confirmed by XMM−Newton observations. Details, including redshift estimate, can be found in Planck Collaboration (2011e).

PLCKESZ G286.99+32.91 : Candidate new cluster confirmed by XMM−Newton observations. Details, including redshift estimate, can be found in Planck Collaboration (2011e).

PLCKESZ G292.51+21.98 : Candidate new cluster confirmed by XMM−Newton observations. Details, including redshift estimate, can be found in Planck Collaboration (2011e).

PLCKESZ G294.66−37.02 : Possible contamination by dust emission could affect Y estimate.

PLCKESZ G304.84−41.42 : Candidate new cluster. BSC−RASS source in the field. In ESO observation logs.

PLCKESZ G308.32−20.23 : Candidate new cluster confirmed by XMM−Newton observations. Details, including redshift estimate, can be found in Planck Collaboration (2011e).

PLCKESZ G337.09−25.97 : Candidate new cluster confirmed by XMM−Newton observations. Found to be a double cluster. Details, including redshift estimate, can be found in Planck Collaboration (2011e).

PLCKESZ G345.40−39.34 : Redshift ($z = 0.044831$) quoted in den Hartog & Katgert (1996).

Table 17. ESZ Catalog Columns

Keyword	Type	Units	Description
INDEX	Integer	UNITLESS	Index of clusters
NAME	String	UNITLESS	*Planck* Name of Cluster Candidate
GLON	Real*8	degrees	Galactic Longitude from Planck
GLAT	Real*8	degrees	Galactic Latitude from Planck
RA	Real*8	degrees	Right Ascension from Planck (J2000)
DEC	Real*8	degrees	Declination from Planck (J2000)
SNR	Real*4	UNITLESS	Signal to Noise Ratio Returned by the matched multi-filter (MMF3)
ID	String	UNITLESS	External Identifier of Cluster e.g. Coma, Abell etc.
REDSHIFT	Real*4	UNITLESS	Redshift of Cluster from the MCXC X-ray cluster compilation (Piffaretti et al. 2010) unless stated otherwise in the notes
GLON_X	Real*8	degrees	Galactic Longitude of the associated X-ray cluster
GLAT_X	Real*8	degrees	Galactic Latitude of the associated X-ray cluster
RA_X	Real*8	degrees	Right Ascension of the associated X-ray cluster (J2000)
DEC_X	Real*8	degrees	Declination of the associated X-ray cluster (J2000)
THETA_X	Real*4	arcminute	Angular size at 5R500 from X-ray data.
Y_PSX	Real*4	arcminute^2	Integrated Compton-Y at X-ray position and within 5R500 (THETA_X)
Y_PSX_ERR	Real*4	arcminute^2	Uncertainty in Integrated Compton-Y at X-ray position and within 5R500 (THETA_X)
THETA	Real*4	arcminute	Estimated angular size from matched multi-filter (MMF3)
THETA_ERR	Real*4	arcminute	Uncertainty in Estimated angular size from matched multi-filter (MMF3)
Y	Real*4	arcminute^2	Integrated Compton-Y at Planck position and within THETA from matched multi-filter (MMF3)
Y_ERR	Real*4	arcminute^2	Uncertainty in Integrated Compton-Y at Planck position and within THETA from matched multi-filter (MMF3)

[1]Source name designations consist of a prefix and a positional qualifier, the latter is in Galactic coordinates and specified as "Glll.ll+bb.bb" where the (l,b) values are truncated. The prefix used in the ESZ portion of the ERCSC is PLCKESZ - Planck ESZ catalog.

A. Glossary

List of Abbreviations

ACT	Atacama Cosmology Telescope
ADU	Analog to Digital Unit
AMI	Arcminute Microkelvin Imager
CMB	Cosmic Microwave Background
COBE	Cosmic Background Explorer
C3PO	Cold Core Catalogue of Planck Objects
DMR	Differential Microwave Radiometer
DPC	Data Processing Center
ECC	Early Cold Cores catalogue
ERCSC	Early Release Compact Source Catalogue
ESA	European Space Agency
ESO	European Southern Observatory
ESZ	Early Sunyaev Zeldovich catalogue
FEBeCoP	Fast Effective Beam Convolution in Pixel space
FITS	Flexible Image Transport System
FIRAS	Far Infrared Absolute Spectrophotometer
FWHM	Full Width at Half Maximum
HFI	High Frequency Instrument
IFCAMex	Mexican hat source detection algorithm designed at IFCA, Santander, Spain
IPAC	Infrared Processing and Analysis Center (Caltech, Pasadena, USA)
IRAS	Infrared Astronomical Satellite
ISM	Interstellar Medium
K_{RJ}	Kelvin Rayleigh-Jeans, a unit of brightness temperature
LFI	Low Frequency Instrument
MaxBCG	An algorithm which identifies clusters using the red-sequence of galaxies
MC	Monte-Carlo
MCXC	Meta-Catalogue of X-ray detected Clusters of galaxies
MMF	Multi-frequency Matched Filter
NASA	National Aeronautics and Space Administration
OD	Operational Day
PMF	Paris Matched Filter source detection algorithm
PSF	Point Spread Function

List of Abbreviations (continued)

PwS	Powell Snakes source detection algorithm
QA	Quality Assessment
QSO	Quasi-stellar object or quasar
ROSAT	Roentgen Satellite
SDSS	Sloan Digital Sky Survey
SED	Spectral Energy Distribution
SExtractor	Source Extractor source detection algorithm
SNR	Signal to Noise Ratio
SPT	South Pole Telescope
SRCEXT	ERCSC module which extracts parameters of sources
TOI	Time Ordered Information
USPDC	United States Planck Data Center
UTC	Universal Time Control
VLA	Very Large Array
VO	Virtual Observatory
WISE	Wide-field Infrared Survey Explorer
WMAP	Wilkinson Microwave Anisotropy Probe
XMM	X-ray Multimirror telescope

REFERENCES

Aatrokoski, J., Lähteenmäki, A., Tornikoski, M., Valtaoja, E., Maino, D., Galeotta, S., Zacchei, A., & Pasian, F. 2010, MNRAS, 401, 597

Abell, G. O., Corwin, H. G., Jr., & Olowin, R. P. 1989, ApJS, 70, 1

Allen, S. W., et al. 1992, MNRAS, 259, 67

Appenzeller, I., et al. 1998, ApJS, 117, 319

Arnaud, M., Pratt, G. W., Piffaretti, R., Böhringer, H., Croston, J. H., & Pointecouteau, E. 2010, A&A, 517, A92

Ashdown, M. A. J., et al. 2007, A&A, 471, 361

Beichman, C. A., Neugebauer, G., Habing, H. J., Clegg, P. E., & Chester, T. J. 1988, Infrared astronomical satellite (IRAS) catalogs and atlases. Volume 1: Explanatory supplement, 1,

Bertin, E., & Arnouts, S. 1996, A&AS, 117, 393

Carlstrom, J., et al., 2002, ARA&A, 40, 643

Carvalho, P., Rocha, G., & Hobson, M. P. 2009, MNRAS, 393, 681

Cavagnolo, K. W., Donahue, M., Voit, G. M., & Sun, M. 2008, ApJ, 682, 821

Chary, R., et al., 2004, ApJ, 154, 80

Condon, J. J., Cotton, W. D., Greisen, E. W., Yin, Q. F., Perley, R. A., Taylor, G. B., & Broderick, J. J. 1998, AJ, 115, 1693

David, L. P., Forman, W., & Jones, C. 1999, ApJ, 519, 533

den Hartog, R., & Katgert, P. 1996, MNRAS, 279, 349

Ebeling, H., Edge, A. C., Mantz, A., Barrett, E., Henry, J. P., Ma, C. J., & van Speybroeck, L. 2010, MNRAS, 407, 83

Edge, A. C., et al. 1994, A&A, 289, L34

Finkbeiner, D. P., Davis, M., & Schlegel, D. J. 1999, ApJ, 524, 867

Gregory, P. C., Scott, W. K., Douglas, K., & Condon, J. J. 1996, ApJS, 103, 427

González-Nuevo, J., Argüeso, F., López-Caniego, M., Toffolatti, L., Sanz, J. L., Vielva, P., & Herranz, D. 2006, MNRAS, 369, 1603

Górski, K. M., Hivon, E., Banday, A. J., Wandelt, B. D., Hansen, F. K., Reinecke, M., & Bartelmann, M. 2005, ApJ, 622, 759

Griffith, M. R., Wright, A. E., Burke, B. F., & Ekers, R. D. 1995, ApJS, 97, 347

Healey, S. E., Romani, R. W., Taylor, G. B., Sadler, E. M., Ricci, R., Murphy, T., Ulvestad, J. S., & Winn, J. N. 2007, ApJS, 171, 61

Hinshaw, G., et al. 2003, ApJS, 148, 135

Hobson, M. P., & McLachlan, C. 2003, MNRAS, 338, 765

Keihänen, E., Keskitalo, R., Kurki-Suonio, H., Poutanen, T., & Sirviö, A.-S. 2010, A&A, 510, A57

López-Caniego, M., Herranz, D., González-Nuevo, J., Sanz, J. L., Barreiro, R. B., Vielva, P., Argüeso, F., & Toffolatti, L. 2006, MNRAS, 370, 2047

López-Caniego, M., González-Nuevo, J., Herranz, D., Massardi, M., Sanz, J. L., De Zotti, G., Toffolatti, L., & Argüeso, F. 007, ApJS, 170, 108

Martini, P., Mulchaey, J. S., & Kelson, D. D. 2007, ApJ, 664, 761

Meinhold, P., et al. 2009, Journal of Instrumentation, 4, 2009

Melin, J.-B., Bartlett, J. G., & Delabrouille, J. 2006, A&A, 459, 341

Menanteau, F., et al. 2010, arXiv:1006.5126.

Melin, J.-B., et al. 2010, A&A, submitted

Mitra, S., Rocha, G., Górski, K. M., Huffenberger, K. M., Eriksen, H. K., Ashdown, M. A. J., & Lawrence, C. R. 2010, arXiv:1005.1929

Murphy, T., et al. 2010, MNRAS, 402, 2403

Murtagh, F., Starck, J.-L., & Bijaoui, A 1995, A&AS, 112, 179

Piffaretti, R., Arnaud, M., Pratt, G. W., Pointecouteau, E., & Melin, J. -. 2010, arXiv:1007.1916

Planck: The Scientific Programme, 2005, ESA-SCI(2005)1, http://www.rssd.esa.int/SA/PLANCK/docs/Bluebook-ESA-SCI(2005)1.pdf

Planck Collaboration. 2011a, Planck early results. I. The Planck mission, A&A, 536, A1

Planck Collaboration. 2011b, Planck early results. II. The thermal performance of Planck, A&A, 536, A2

Planck Collaboration. 2011c, Planck early results. VII. The Early Release Compact Source Catalogue, A&A, 536, A7

Planck Collaboration. 2011d, Planck early results. VIII. The all-sky early Sunyaev-Zeldovich cluster sample, A&A, 536, A8

Planck Collaboration. 2011e, Planck early results. IX. XMM-Newton follow-up for validation of Planck cluster candidates, A&A, 536, A9

Planck Collaboration. 2011f, Planck early results. X. Statistical analysis of Sunyaev-Zeldovich scaling relations for X-ray galaxy clusters, A&A, 536, A10

Planck Collaboration. 2011g, Planck early results. XI. Calibration of the local galaxy cluster Sunyaev-Zeldovich scaling relations , A&A, 536, A11

Planck Collaboration. 2011h, Planck early results. XII. Cluster Sunyaev-Zeldovich optical scaling relations, A&A, 536, A12

Planck Collaboration. 2011i, Planck early results. XIII. Statistical properties of extragalactic radio sources in the Planck Early Release Compact Source Catalogue, A&A, 536, A13

Planck Collaboration. 2011j, Planck early results. XIV. Early Release Compact Source Catalogue validation and extreme radio sources, A&A, 536, A14

Planck Collaboration. 2011k, Planck early results. XV. Spectral energy distributions and radio continuum spectra of northern extragalactic radio sources, A&A, 536, A15

Planck Collaboration. 2011l, Planck early results. XVI. The Planck view of nearby galaxies, A&A, 536, A16

Planck Collaboration. 2011m, Planck early results. XVII. Origin of the submillimetre excess dust emission in the Magellanic Clouds, A&A, 536, A17

Planck Collaboration. 2011n, Planck early results. XVIII. The power spectrum of cosmic infrared background anisotropies, A&A, 536, A18

Planck Collaboration. 2011o, Planck early results. XIX. All-sky temperature and dust optical depth from Planck and IRAS — constraints on the "dark gas" in our Galaxy, A&A, 536, A19

Planck Collaboration. 2011p, Planck early results. XX. New light on anomalous microwave emission from spinning dust grains, A&A, 536, A20

Planck Collaboration. 2011q, Planck early results. XXI. Properties of the interstellar medium in the Galactic plane, A&A, 536, A21

Planck Collaboration. 2011r, Planck early results. XXII. The submillimetre properties of a sample of Galactic cold clumps, A&A, 536, A22

Planck Collaboration. 2011s, Planck early results. XXIII. The Galactic cold core population revealed by the first all-sky survey, A&A, 536, A23

Planck Collaboration. 2011t, Planck early results. XXIV. Dust in the diffuse interstellar medium and the Galactic halo, A&A, 536, A24

Planck Collaboration. 2011u, Planck early results. XXV. Thermal dust in nearby molecular clouds, A&A, 536, A25

Planck Collaboration. 2011v, The Explanatory Supplement to the Planck Early Release Compact Source Catalogue (ESA)

Planck HFI Core Team. 2011a, Planck early results. IV. First assessment of the High Frequency Instrument in-flight performance, A&A, 536, A4

Planck HFI Core Team. 2011b, Planck early results. VI. The High Frequency Instrument data processing, A&A, 536, A6

Savage, R. S., & Oliver, S. 2007, ApJ, 661, 1339

Schneider, Donald P., Bahcall, John N., Gunn, James E., Dressler, Alan, 1992, AJ, 103, 1047

Smail, I., et al. 2007, ApJ, 654, L33

Sunyaev, R. & Zeldovich, Ya. 1972, A&A, 20, 189

Vanderlinde, K., et al. 2010, ApJ, 722, 1180

Wang, L., & Rowan-Robinson, M. 2010, MNRAS, 401, 35

Wen, Z. L., Han, J. L., Liu, F. S., 2009, ApJS, 183, 197

Wright, E. L., et al. 2009, VizieR Online Data Catalog, 218, 283

Wright, E. L., et al. 2010, AJ, 140, 1868

Zwicky, F., Herzog, E., & Wild, P. 1961, Pasadena: California Institute of Technology (CIT), —c1961,

Zacchei et al. 2011, Planck early results. V. The Low Frequency Instrument data processing, A&A, 536, A5